Removing Order Limitations in Local Absorbing Boundary Conditions for Free-Surface Wave Simulations

Towards Accurate Motion Prediction of Semi-Submersible Crane Vessels at Inconvenient Draught

Casper Koopman

Technische Universiteit Delft

TU Delft

MARINE CONTRACTORS

Removing Order Limitations in Local Absorbing Boundary Conditions for Free-Surface Wave Simulations

Towards Accurate Motion Prediction of Semi-Submersible Crane Vessels at Inconvenient Draught

by

Casper Koopman

to obtain the degree of Master of Science

at the Delft University of Technology,

to be defended publicly on February 26th, 2026 at 14:30.

Student number:	4901460	
Report number:	MT.25/26.019.M	
Project duration:	April 1, 2025 – February 26, 2026	
Thesis committee:	Dr. Ir. P.R. Wellens,	TU Delft, supervisor
	Dr. Ir. H.J. De Koning-Gans	TU Delft
	Dr. Ir. M.J.B.M. Pourquie	TU Delft
	Ir. P. Samudero	Heerema Marine Contractors
	Ir. F. Beothy	Heerema Engineering Solutions

An electronic version of this thesis is available at `http://repository.tudelft.nl/`.

During the preparation of this work, the author has made use of Large Language Models. These models served as progress accelerators for conceptualisation, derivation checking, derivation suggestions, code checking, code suggestions, textual refinement and as a sparring partner. The author bears full responsibility for the contents stated in this work.

TU Delft

Preface

Towards accurate and efficient non-linear motion prediction...

This thesis was written as a first step toward boundary treatment that is simultaneously efficient and accurate for non-linear free-surface wave interaction simulations. During the past ten months, I had the opportunity to combine my interests in numerical hydromechanics and programming while developing my own code. Along the way, I obtained knowledge required to tackle this challenging topic and realised that progress in research on non-linear wave problems is itself rarely linear. In particular, the combination of generalised curvilinear coordinates and absorbing boundary condition theory proved challenging at first.

Starting the thesis, the expectation was that a circular boundary with a circular wave was an equivalent situation to a planar boundary and a planar wave. For planar boundaries, a Sommerfeld boundary condition is exact for waves with normal incidence. This means that the wave is fully absorbed and no reflection returns. For circular boundaries, applied in this thesis, the normal incidence equivalent is a circular wave started in the centre of the domain. It therefore seemed natural to expect zero reflection as well, and any deviation was initially attributed to errors in my curvilinear implementation.

Using this configuration as a validation test, many iterations passed in which I repeatedly returned to theory concerning curvilinear coordinates. Eventually I had an implementation yielding a constant reflection coefficient and I was convinced this had to be correct. However, a constant reflection returned, which was unexpected. Inspiration can come from weird places: a ChatGPT prompt directed me to literature explaining a Sommerfeld boundary condition is exact for planar boundaries, but not for curved ones. What I initially considered an implementation mistake turned out to be a fundamental limitation of the boundary condition itself. Although known in theory, arriving at this conclusion was a significant breakthrough. This marked the point where the thesis shifted from debugging to understanding fundamental mathematical limitations. After this, more accurate boundary conditions followed quickly. Yet, implementation is only half the story. Frustratingly, demonstrating their clearly improved performance in tangible results required the same amount of iteration as the implementation.

Nevertheless, I am proud of the final result, combining wave mechanics, numerical discretization, generalised curvilinear coordinates, high-order absorbing boundary condition theory and Bessel functions. What started as a search for implementation errors in the curvilinear coordinates part, eventually evolved into deeper understanding of absorbing boundary condition theory (and through numerous iterations also theory concerning curvilinear coordinates).

During the project, I received guidance and support for which I am grateful. First of all I would like to thank Peter for his guidance, time, and involvement since the start of the project. Meetings were genuinely fun and inspiring, and his flexibility helped me stay motivated during peak periods. I hope this project does not conclude our collaboration and we can continue future research in industrial context. I am also glad that I had the unique opportunity to perform a thesis in collaboration with two companies, Heerema Marine Contractors and Heerema Engineering Solutions. I thereby would also like to thank Pandu and Farkas for their guidance during the project. Furthermore I would like to thank Henk de Koning-Gans and Mathieu Pourquie for taking place in my thesis committee and anyone else who has helped or inspired me during my thesis.

Met deze thesis beëindig ik ook een studententijd waar ik met ontzettend veel plezier op terugkijk. Na 7.5 jaar vol ervaringen, kennis en vooral heel veel lol ben ik dankbaar voor iedereen waarmee ik dat heb mogen delen. Dat was niet mogelijk zonder mijn clubgenoten, de boze mannen van de Raamstraat, bestuursgenoten en studiegenoten. Daarnaast wil ik mijn familie; Papa, Mama en Sjoerd, bedanken voor de leuke en veilige thuishaven om altijd even naar terug te kunnen varen.

Casper Koopman
Delft, February 2026

Contents

Nomenclature

Tensor calculus

$\cdot\|^n$	$\cdot$ evaluated at time level n
$\cdot\|_{i,j}$	$\cdot$ evaluated at staggered location with indices i, j
δ_β^α	Kronecker delta
$\Gamma_{\beta\gamma}^\alpha$	Christoffel symbol of the second kind
$\Gamma_{\alpha\beta\gamma}$	Christoffel symbol of the first kind
$\mathcal{S}$	Boundary of control volume
Ω	Control volume
$\sqrt{g*}$	Cell area/volume
$\vec{\nabla}$	Gradient operator
$\vec{\tau}$	Tangential vector
$\vec{a}^{(\alpha)}$	Contravariant base vector
$\vec{a}_x^{(\alpha)}$	x component of contravariant base vector
$\vec{a}_y^{(\alpha)}$	y component of contravariant base vector
$\vec{a}_{(\alpha)}$	Covariant base vector
$\vec{n}$	Normal vector
ξ^α	Curvilinear coordinate direction α
$g*$	Determinant of covariant metric tensor
$g^{\alpha\beta}$	Contravariant metric tensor
$g_{\alpha\beta}$	Covariant metric tensor
U^α	Contravariant velocity component in coordinate direction α
U_α	Covariant velocity component in coordinate direction α
V^α	Scaled contravariant velocity component in coordinate direction α

Grid generation parameters

β	Mapping/curvature strength parameter
f_d	Rectangular-interior ratio controlling mapped layers
L_x	Domain length in x-direction
L_y	Domain length in y-direction
N_e	Number of rectangular interior cell layers in curvilinear grid
N_r	Number of radial cell layers in curvilinear grid
R_d	Domain radius
$R_{d,ref}$	Reference domain radius

Mathematical symbols

$\angle(\vec{x})$	Angle of vector x in polar coordinates
$\mathfrak{I}$	Imaginary value
$\|\|\vec{x}\|\|$	Magnitude of vector x or complex number x
$\mathfrak{R}$	Real value
$H_m^{(1)}$	Hankel function of first kind order m
$H_m^{(2)}$	Hankel function of second kind order m
J_m	Bessel function of first kind order m
Y_m	Bessel function of second kind order m

Other symbols

Δt	Time step size
μ	Long crested wave direction
ω	Angular frequency
Φ	Wave potential function
ϕ_j	Auxiliary variable j for Hagstrom-Waburton formulation
ρ	Fluid density
θ_{inc}	Incidence angle
θ_{refl}	Reflected angle
φ	Angular coordinate (polar coordinates)
$\vec{k}$	Wave vector
$\vec{u}$	Velocity vector
ζ	Free surface elevation
A	Amplitude
c	Wave phase speed
C_w	Bottom friction coefficient
G	Gravitational acceleration
h	Water depth (bathymetry)
k	Wave number
q	Auxiliary variable 2nd order GABC formulation
R	Reflection coefficient
r	Radial coordinate (polar coordinates)
RHS	Right hand side of GABC
T	Wave period
t	Time
u_x	x-component of velocity in physical space
u_y	y-component of velocity in physical space

List of Abbreviations

ABC Absorbing Boundary Condition

BC Boundary Condition

CEM Circular Engquist-Majda

CFD Computational Fluid Dynamics

CRBC Complete Radiation Boundary Condition

FV Finite Volume

GABC Generating Absorbing Boundary Condition

HMC Heerema Marine Contractors

IMEX Implicit Explicit

iVOF improved Volume of Fluid

LCW Long-Crested Wave

LS Level Set Method

LSQ Least Squares

NRBC Non Reflecting Boundary Condition

PEM Planar Engquist-Majda

PML Perfectly Matched Layer

RAO Response Amplitude Operator

RBC Radiation Boundary Condition

SFD Sommerfeld

SSCV Semi-Submersible Crane Vessel

VOF Volume of Fluid

Summary

Predicting the motions of Semi-Submersible Crane Vessels (SSCVs) at shallow draught, with a small column of water on top of the floaters, has proven to be a challenging hydrodynamic problem to solve with linear diffraction theory. This situation is often referred to as 'inconvenient draught'. In order to capture the physics occurring at inconvenient draught, more advanced numerical methods are promising. However, these methods require boundaries to truncate a domain corresponding to open sea for computational feasibility. In absence of special boundary measures, this truncation introduces an artificial boundary at which outgoing waves undesirably reflect back into the computational domain. So far, boundary treatment that is simultaneously computationally affordable and sufficiently accurate for inconvenient draught is limited. Consequently, wave reflections pose significant challenges in terms of both computational cost and accuracy. Obtaining efficient and accurate boundary conditions is therefore the subject of this work.

High-order local Absorbing Boundary Conditions (ABCs) hold large potential to serve as accurate and efficient boundary treatment. This is due to their similar or improved performance at far lower computational cost than absorbing zones. For simulations with complex free-surface interaction, present at inconvenient draught, methods with rectangular interiors have proven accuracy. Problems arise in the corners of rectangular domains when applying high-order ABCs. These ABCs require information along boundaries in tangential direction, inherently limited at corners.

To overcome this limitation, this work applies a circular boundary to rectangular domains by the use of generalised curvilinear coordinates. On the circular boundary, no limitation exists for acquiring information in tangential direction, enabling the consistent application of high-order ABCs. To this end, a grid with rectangular interior and circular boundary can be mapped to a plus-shaped computational grid. The approach employs a staggered curvilinear Finite Volume (FV) discretisation on the plus-shaped computational grid. For the mapping, the interior edges of the plus-shape need to be coupled to resemble a continuous domain. The governing equations are the linearised shallow water equations, which are used to study multidirectional wave propagation and absorption in a 2D horizontal plane. The coupling methodology is benchmarked to a Cartesian implementation and shows to preserve numerical accuracy, with introduced errors remaining comparable to inherent discretisation errors.

On the circular boundary, three types of Generating Absorbing Boundary Conditions (GABCs) are discretised. One based on a Sommerfeld (SFD) operator to benchmark results and two second-order formulations based on a Planar Engquist-Majda (PEM) operator and a Circular Engquist-Majda (CEM) operator. Three tests were performed to assess performance. A centred source test showed similar performance of SFD and PEM, with CEM clearly improving absorbing performance. An off-centre source test showed improved absorbing performance of PEM over SFD as tangential variation is incorporated in the formulation. The CEM formulation only improves results for sufficiently large source-boundary distance relative to wavelength, i.e. for large values of dimensionless parameter kr. However this distance is quickly reached, resulting in overall improved performance. Furthermore, decreasing kr leads to systematically higher reflection levels for all GABCs formulations. This indicates that while circular boundaries eliminate corners, they introduce an kr-dependent absorption limitation. A last test for Long-Crested Waves (LCWs) introduced over the boundary was performed. All formulations showed generating performance. However, numerical artefacts were present for the PEM and CEM formulation, requiring further refinement for accurate introduction. Quantitative reflection coefficients for this test could not be reported, but qualitative analysis showed PEM and CEM yielding better absorbing performance than SFD. A clear classification between CEM and PEM could not be obtained.

Future work should investigate the numerical introduction artefacts for the higher-order GABC formulations. Once robust wave introduction is achieved, a test yielding quantitative reflection coefficients for LCWs will give insight on whether the kr-dependence observed for radiating sources also governs absorption of LCWs on circular boundaries.

Motivation

Heerema Marine Contractors is an offshore contractor that operates Semi-Submersible Crane Vessels (SSCVs). When these vessels operate in shallow water, their draught should be limited to avoid seabed contact. Also, when performing crane suspended transport of platform structures, a SSCV's draught is limited to reduce vessel resistance. At this limited draught, the tops of the SSCV's floaters are in close proximity to the free surface. This situation has proven to be a challenging hydrodynamic problem to solve with linear diffraction theory, and is commonly referred to as 'inconvenient draught'.

Linear diffraction theory generally is a versatile and accurate tool that serves as a industry standard to calculate vessel motions. Due to linear assumptions and the existence of a Green's function, this allows to discretise a vessel in panels with corresponding sources. Each source's influence can be evaluated at another location through a Green's function that, by construction, satisfies the linearised free-surface boundary condition [33]. This allows to solve each source strength by imposing a no penetration boundary condition on the discretised hull and compute vessel motions without imposing exterior boundary conditions. However, a Green's function exploits linearity in its application. For non-linear wave interaction, no Green's function exists. Generally speaking, for slightly non-linear situations, linear diffraction theory can be adapted slightly to still produce valuable results in engineering.

As a SSCV moves in waves with the floater tops in close proximity to the free surface, several effects occur that pose serious challenges for linear diffraction theory. The challenges posed are threefold. First of all, panels in close vicinity to the free surface produce unrealistically high free-surface levels, resulting in unreliable motion prediction. A common approach is to apply damping lids to dampen the free-surface elevation. However, these damping lids are designed for a different situation and have to be tuned per case specifically. This tuning necessitates calibration data for different cases. Second, non-linear free-surface effects such as shoaling and wave breaking cause interaction of wave frequency components, which is not captured under linear assumptions. Third of all, a floater can emerge from the free surface, which imposes a heavy geometric non-linearity of an abruptly changing water plane area. All together, these challenges call for a method that can accurately handle these effects to predict the non-linear motion behaviour of SSCVs at inconvenient draught.

Methods capable of handling these effects can unfortunately no longer rely on the convenience of a Green's function. This automatically has the consequence that these methods require exterior boundary conditions. As the desired simulated situation corresponds to open sea, the physical domain is way too large to simulate and requires truncation for computational feasibility. This truncation should ideally not change the simulated situation by letting waves leave and enter the domain without limitations. This however has been an area of exhaustive research due to the apparent simplicity of the requirement compared to the actual complexity. In absence of special boundary measures, this truncation introduces an artificial boundary at which outgoing waves undesirably reflect back into the computational domain. Special boundary measures aim to limit this reflection to acceptable limits. As will become apparent in both Appendix A and chapter 1, wave reflections pose significant issues for non-linear motion prediction in terms of computational demand and accuracy.

Concluding, in order to predict the non-linear hydrodynamic behaviour of SSCVs at inconvenient draught, an enabling puzzle piece is both accurate and computationally efficient boundary treatment. Therefore, the main body of this thesis concerns this topic. Applying this boundary treatment to numerical methods that explicitly resolve detailed non-linear free-surface interaction, is expected to enable quantification of the non-linear motion behaviour. This expectation is supported by literature demonstrating the capability of these methods to accurately capture non-linear wave interaction, as described in chapter 1 and Appendix A. However, the roadmap toward accurate and computationally efficient simulations at inconvenient draught, is longer than what can be attained during one or two MSc theses. Therefore it is important to set a clear roadmap toward this goal, which is described in Appendix I.

1

Introduction

To accurately simulate complex, non-linear free-surface interactions with offshore structures, Volume of Fluid (VOF) methods for Cartesian grids have been developed with proven accuracy [11], [27], [36]. However, achieving both accuracy and efficiency in long-duration simulations remains a challenge. The desired simulated situation corresponds to open sea, in which waves travel infinitely in horizontal directions. Since this physical domain is unbounded, the computational domain must be truncated for computational feasibility. In absence of special boundary measures, this truncation introduces an artificial boundary at which outgoing waves undesirably reflect back into the computational domain. Upon interaction with the object of interest, these reflections reduce the accuracy of these simulations. To enable accurate and efficient non-linear wave interaction simulations, these spurious reflections should therefore be tackled by effective and efficient boundary treatment. Furthermore, the boundary treatment should allow for the accurate introduction of waves to simulate truly open boundaries and produce physically realistic situations.

In general, there are two categories of the aforementioned boundary treatment. These are Absorbing Layers and Absorbing Boundary Conditions (ABCs). Also a combination of the two exist. These will be introduced and described in the following sections.

1.1. Absorbing Layers

Absorbing layers can be used to dampen out waves over space. This can be done in several ways, resulting in different types of absorbing layers. A general term to describe these methods are dissipation zones, in which waves lose (dissipate) energy over time to prevent reflections. In literature, several types of dissipation zones can be found which can rely on different mechanisms; mesh stretching, added viscosity, adding momentum source terms and solution relaxation. All of these methods rely on adding layers to the computational domain, which requires significant computational resources.

For Computational Fluid Dynamics (CFD) simulations for example, Choi et al. [4] compare several dissipation zones that rely on different principles for regular waves in 2D. They evaluate performance using an accumulated reflection coefficient based on the minimum and maximum of first-harmonic standing-wave amplitudes. What stands out is that large absorbing zones are added to the domain, which results in ratios of added layer with respect to desired domain of 3/7 or even 1/1. Accumulated reflection coefficients range between 1.9% and 6.7%, depending on the layer size and damping mechanism of the absorbing zone. What also stands out is that doubling the size of the absorbing layers only reduces this accumulated reflection by 1-2%, with initially better performing zones showing smaller improvements. Another example is given by Jacobsen, Fuhrman, and Fredsøe [23], which discuss the implementation of wave relaxation zones in the open-source CFD package OpenFOAM. The authors mention that for proper damping performance, the required length of the relaxation zone at one side of the domain should be larger or equal to the wavelength of interest.

The Perfectly Matched Layer (PML), first introduced by Berenger [2], is an optimised version of the absorbing layer. This was introduced for electromagnetic waves. Also this method adds to the compu-

tational costs, and no adaptation to CFD simulations has been found. The method has been combined with high-order ABCs by Hagstrom et al. [21] and with Complete Radiation Boundary Conditions (CRBCs) by Kim [26], which will be introduced in the next section.

Regardless of the effectiveness of the dissipation zone, the methodology significantly adds to the computational effort. Therefore, a more computationally efficient alternative is desired.

1.2. Absorbing Boundary Conditions

An absorbing boundary condition is prescribed in order to prevent or minimize reflection back into the domain. In literature, absorbing boundary conditions have several common names such as radiation boundary conditions (RBCs), non-reflecting boundary conditions (NRBCs), and complete radiation boundary conditions (CRBCs). In this work, the term ABC is used to refer to this class of boundary conditions. Terms like Generating-Absorbing, transparent or open boundary conditions also occur in literature. Mostly, but not always, these refer to boundary conditions that should also allow for introduction of waves into the domain. In this work, this subclass will be referred to as Generating Absorbing Boundary Condition (GABC). All implemented boundary conditions in this work are formulated as GABCs. As will become apparent, the generative part can be enabled or disabled easily which switches the type between GABC and ABC formally.

In the literature, ABCs are commonly classified by their order and by whether they are local or non-local. The order refers to the accuracy with which waves are absorbed, with higher orders generally performing better. Local ABCs depend only on neighbouring points in space and time, making them computationally efficient. In contrast, non-local methods require storing long histories or solving globally coupled boundaries, which is often impractical and expensive. Local methods are derived from a general non-local boundary operator, and thereby approximate this locally.

For the purpose of obtaining efficient boundary treatment, local methods are required. A comprehensive review of high-order local ABCs is given by Givoli [13]. A brief summary of the research leading to current high-order local ABCs is given below.

1.2.1. Low-Order Absorbing Boundary Conditions

Engquist and Majda [10] approximated the non-local boundary operator by a Padé series. This series is of arbitrary order of accuracy, but requires derivatives of increasing order as well, posing a challenge. Bayliss and Turkel [1] used a wave equation expansion in cylindrical coordinates to obtain a product of operators. This sequence of operators is also of arbitrarily high order, but again results in derivatives of increasing order. Higdon [22] also devised a product of operators, however in Cartesian coordinates, to obtain a high-order sequence. A Higdon sequence of order P applied to wave potential Φ is given in Equation 1.1, optimally absorbing multiple waves with phase speed c and incidence angles θ_j.

$$\left(\Pi_{j=1}^{P}\left(\frac{\partial}{\partial t}+\frac{c}{\cos\theta_j}\frac{\partial}{\partial x}\right)\right)\Phi=0 \tag{1.1}$$

In principle, the pioneering examples of the previous authors are high-order local ABCs that rely on different approaches to approximate the non-local boundary operator. However, their formulation introduces high-order derivatives, which makes their numerical implementation difficult. For instance, in Higdon ABCs the derivative normal to the boundary is difficult to discretise beyond a certain order, as no grid points are available outside the boundary. While one-sided stencils are possible, these often suffer from numerical instability [36]. For this reason, the aforementioned ABCs are considered as low-order ABCs in literature. Nevertheless, the underlying principles for deriving local ABCs remained influential and were later exploited in the literature to construct implementable high-order local ABCs.

1.2.2. High-Order Absorbing Boundary Conditions

An ABC formulation is generally only considered high-order if its implementation is also practically feasible. This distinction is often made in literature, separating low-order and high-order ABCs through a sense of practicality.

The first to implement an implementable high-order ABC were Collino and Joly [5], through introduction

through a system of auxiliary variables. This formulation allows solving a system of equations at the boundary while keeping derivatives low, thus attaining a high-order formulation while being practical. So-called functions of auxiliary variables are defined along the boundary and only derivatives tangential to the boundary are involved. This introduces the issue that in the corners of a Cartesian domain, tangential derivatives cannot be composed easily. Therefore special corner compatibility conditions have to be applied. These corner compatibility conditions are a recurring topic in literature due to the challenges associated with their formulation, implementation and accuracy.

Regardless, the auxiliary variable formulation has been the way forward since to realise well performing local ABCs. Grote and Keller [15] and Hagstrom and Hariharan [16] constructed auxiliary variable formulations for high-order ABCs using spherical or circular boundaries using polar coordinates, respectively using spherical harmonics and Bayliss-Turkel operators. For dispersive waves in a 2D Cartesian waveguide, Givoli and Neta [14] reformulated a Higdon sequence by the use of auxiliary variables with derivatives tangential to the boundary. Hagstrom and Warburton [19] improved the Givoli-Neta formulation for open domains and added corner conditions, however without dispersion. The Hagstrom-Waburton auxiliary variable formulation of order P is given below, in which ϕ_j are the auxiliary variables and a_j chosen coefficients.

$$\left(a_0\frac{\partial}{\partial t} + c\frac{\partial}{\partial n}\right)\Phi = \frac{\partial \phi_1}{\partial t} \tag{1.2}$$

$$\left(a_j\frac{\partial}{\partial t} + c\frac{\partial}{\partial n}\right)\phi_j = \left(a_j\frac{\partial}{\partial t} - c\frac{\partial}{\partial n}\right)\phi_{j+1} \text{ for j = 1, 2, ... , P} \tag{1.3}$$

$$\phi_{P+1} = 0 \tag{1.4}$$

These auxiliary variables can be seen as the residuals that were not absorbed by the previous operator. Subsequent Higdon operators, with derivatives in time t and normal direction n are applied to further absorb parts of the residual that were not absorbed by the previous operator. Therefore, Equation 1.3 still includes normal derivatives of auxiliary variables, but is rewritten by Hagstrom and Warburton to include only tangential derivatives.

The high-order formulations that are mentioned until now, do not take absorbing evanescent waves into account. Hagstrom and Warburton [20] did design such a formulation for a 2D wave equation in time domain and confirmed results comparing to a PML simulation. The authors reported no adverse effects from the corner closure conditions. This inclusion of evanescent waves into the ABC is often referred to as a CRBCs. The CRBC has been developed since, for example in the two consecutive papers of Hagstrom and Kim, formulating a CRBC for the Helmholtz equation in waveguides [17] and later deriving corner conditions for open domains as well [18]. Also Modave, Geuzaine, and Antoine [28] investigated the Helmholtz equation and the performance of corners, stating that right angle corners are best to limit reflections in frequency domain simulations.

1.2.3. Generating Absorbing Boundary Conditions

For simulating free-surface waves in CFD, dispersive and directional effects have to be taken into account in multidirectional-unbounded media. Designing boundary conditions based on auxiliary variables for rectangular domains necessitate corner compatibility conditions, whereas other local approaches struggle with creating the numerical equivalent of high-order boundary conditions. In the following literature, the auxiliary variable approach is mitigated whereas workarounds are found for the numerical equivalents of high-order derivatives. These approaches are described in this section.

Wellens [36] mitigates the issue of high-order derivatives normal to the boundary, by including dispersive effects through a vertical derivative. These dispersive effects are derived from linear wave theory. Based on this, Düz et al. [9] compares two ABCs based on Higdon operators, applied to free-surface waves. The first ABC includes dispersive effects in a first-order Higdon operator using a second-order vertical derivative. The second ABC uses a second-order Higdon operator and can thus tune for two directions with optimal absorption, and includes the dispersive effects in one of the Higdon operators using a second-order vertical derivative. The latter shows proper absorbing performance over a wide range of angles, as the absorbing performance is not limited to the chosen angles.

Wellens and Borsboom [37] created a GABC which allows waves to travel into the domain as well, which makes a truly open boundary condition possible. However including both dispersive and directional effects, as in the second-order Higdon ABC by Düz et al. [9], proved difficult to combine with incoming waves. Therefore Wellens and Borsboom [37] resorted to an approach using a first-order boundary condition, tuning for one angle with optimal absorbance.

The implementation of tackling dispersion using a vertical derivative became cumbersome at the free surface itself however. In the applied VOF method, no pressures and velocities are solved above the free surface. This makes it difficult to construct a second-order derivative. One sided vertical derivatives were attempted, but resulted in unstable simulations [37]. In [9] an ordinary first/second-order Higdon operator was applied at the free surface for the first and second-order ABC respectively. Therefore, Wellens and Borsboom make a compromise by applying a Sommerfeld (SFD) BC at the free surface, which is essentially a first-order Higdon operator for waves with a certain incidence angle. This compromise resulted in higher reflection, with 5% instead of the expected 2%. In [9], no reflection coefficients were given, only reflections in terms of error norms.

The latest work on the GABC by Chang and Wellens [3] was to extend the GABC for situations with a mean flow through the boundary, other than only waves propagating through the boundary. This extends the applicability of the GABC in offshore wave interaction simulations to more realistic simulations. Similar performance is reached with this boundary condition, with reflections under 5%.

1.3. Literature Gap and Research Questions

What stands out in literature is the complexity associated with the corner conditions that need to be devised when working in multi-directionally unbounded Cartesian domains. Authors either devise complex derivations for corner conditions for relatively simple equations, or prevent corner conditions by making the domain unbounded in only one direction. For free-surface CFD simulations in physically unbounded truncated Cartesian domains, high-order formulations and corner conditions are prevented. Other approaches are taken to improve the performance of ABCs for waves with dispersive and directional variety. However, this is limited to a certain order of accuracy. This results in the following gap in literature: no author has circumvented corner conditions for multi-directionally unbounded Cartesian domains to apply higher-order ABCs.

Corners can be circumvented by applying a circular boundary to a Cartesian domain. Curvilinear coordinates can be used to maintain a Cartesian orthogonal interior while applying a circular boundary. On this circular boundary, a higher-order absorbing boundary condition can be applied without corner conditions. This thesis will answer the following research question in order to investigate the addressed research gap:

Can higher-order local generating absorbing boundary conditions for multidirectional waves be applied for rectangular grids when circumventing corner compatibility conditions by mapping to a circular boundary?

To tackle this main research question, essential sub-questions are formulated that will lead to major advancements towards the answer of the main research question:

1. Can waves be simulated using generalised curvilinear coordinates when applying a circular boundary to a domain with a rectangular interior?
2. Is it possible to discretise a Sommerfeld ABC on a circular boundary in generalised curvilinear coordinates for normal/arbitrary incidence?
3. Is it possible to introduce waves on the circular boundary while absorbing these waves with the Sommerfeld ABC, forming a first-order GABC?
4. Is it possible to formulate a higher-order ABC on the circular boundary, absorbing waves with a range of incidence angles?
5. Is it possible to introduce waves on the circular boundary while absorbing these waves with a higher-order ABC, forming a higher-order GABC?

2

Methodology

To apply higher-order GABCs for grids with rectangular interiors, corners are prevented by using a curvilinear mapping. This mapping preserves a structured grid with a rectangular interior, while transforming the outer boundary to a circular shape. Higher-order GABCs can then be applied along this boundary. In this work, GABCs of limited order are presented that would require corner conditions for Cartesian grids. This way, the concept will be tested in a 2D horizontal plane governed by the linearised shallow water equations. These equations can model non-dispersive shallow water wave propagation and allow testing the absorbing performance under varying incidence angles.

2.1. Governing Equations

$$\frac{1}{\rho G}\frac{\partial p}{\partial t} + h(\vec{\nabla} \cdot \vec{u}) = 0 \tag{2.1}$$

$$\frac{\partial \vec{u}}{\partial t} + \frac{1}{\rho}(\vec{\nabla} p) = 0 \tag{2.2}$$

The linearised shallow water equations with constant bathymetry h are described above. The continuity equation is represented by 2.1 and the momentum equation by 2.2. The pressure head is defined by p and is analogous to the free-surface elevation ζ through $p = \rho G \zeta$. Unit density will be used in the equations. The velocity vector is defined as $\vec{u}$. G is used as gravitational constant, as lowercase g will be used for metric terms. This will become apparent in the discretisation of these equations.

2.2. Generalised Curvilinear Coordinates

The curvilinear implementation in this work follows conventions used in ISNAS ([24], [25], [32]). A brief summary will be given here to highlight the methodology, terminology and variables used. Equations from here onwards are expressed in Einstein notation, with sub- and superscripts $\alpha, \beta, \gamma, \delta$.

A generalised curvilinear coordinate system will be introduced. This is indicated by $\xi^\alpha = (\xi^1, \xi^2)$. The corresponding physical coordinates are $\vec{x} = (x, y)$. The transformation from physical coordinates to curvilinear coordinates is called T and can be characterised by base vectors.

$$(x, y) \xrightarrow{T} (\xi^1, \xi^2) \tag{2.3}$$

Two types of base vectors can be defined. Covariant base vectors are tangent to coordinate lines ξ^α and are defined as $\frac{\partial \vec{x}}{\partial \xi^\alpha}$. Contravariant base vectors are perpendicular to coordinate lines where ξ^α is constant, and are defined as $\vec{a}^{(\alpha)} = \frac{\partial \xi^\alpha}{\partial \vec{x}}$. The two sets of base vectors are defined such that $\vec{a}_{(\alpha)} \cdot \vec{a}^{(\beta)} = \delta^\beta_\alpha$. Here, δ^β_α is the Kronecker delta.

The dot products of the base vectors define the metric tensors:

$$g_{\alpha\beta} = \vec{a}_{(\alpha)} \cdot \vec{a}_{(\beta)} \;\&\; g^{\alpha\beta} = \vec{a}^{(\alpha)} \cdot \vec{a}^{(\beta)} = (g_{\alpha\beta})^{-1} \tag{2.4}$$

The determinant of covariant metric tensor $g_{\alpha\beta}$ is denoted by $g*$. If the computational grid (ξ^1, ξ^2) is defined with unit spacings, $\sqrt{g*}$ gives the cell area in 2D.

Vector and tensor quantities are invariant under coordinate transformations and can both be expressed using covariant and contravariant components. These correspond to a contravariant and covariant basis respectively. Christoffel symbols characterise the spatial variation of the basis when differentiating vectors or tensors in a curvilinear coordinate system. The different representations and occurrence of Christoffel symbols are demonstrated for velocity vector $\vec{u}$ in the following equations:

$$\vec{u} = U^\alpha \vec{a}_{(\alpha)} = U_\alpha \vec{a}^{(\alpha)} \tag{2.5}$$

$$\frac{\partial \vec{u}}{\partial \xi^\beta} = \frac{\partial U^\alpha \vec{a}_{(\alpha)}}{\partial \xi^\beta} = \frac{\partial U^\alpha}{\partial \xi^\beta}\vec{a}_{(\alpha)} + U^\alpha \frac{\partial \vec{a}_{(\alpha)}}{\partial \xi^\beta} = \left(\frac{\partial U^\alpha}{\partial \xi^\beta} + \vec{a}^{(\alpha)} \cdot \frac{\partial \vec{a}_{(\gamma)}}{\partial \xi^\beta} U^\gamma\right)\vec{a}_{(\alpha)} \tag{2.6}$$

The factorisation to express the derivative of the base vector in a covariant basis results in a Christoffel symbol of the second kind. These will be indicated as $\Gamma^\alpha_{\beta\gamma}$ and can be computed as follows:

$$\Gamma^\alpha_{\beta\gamma} = \vec{a}^{(\alpha)} \cdot \frac{\partial \vec{a}_{(\gamma)}}{\partial \xi^\beta} = \frac{1}{2} g^{\alpha\delta}\left(\frac{\partial g_{\delta\gamma}}{\partial \xi^\beta} + \frac{\partial g_{\delta\beta}}{\partial \xi^\gamma} - \frac{\partial g_{\gamma\beta}}{\partial \xi^\delta}\right) \tag{2.7}$$

Christoffel symbols of the first kind can then be found as follows:

$$\Gamma_{\alpha\beta\gamma} = g_{\alpha\delta}\Gamma^\delta_{\beta\gamma} = \frac{1}{2}\left(\frac{\partial g_{\alpha\gamma}}{\partial \xi^\beta} + \frac{\partial g_{\alpha\beta}}{\partial \xi^\gamma} - \frac{\partial g_{\beta\gamma}}{\partial \xi^\alpha}\right) \tag{2.8}$$

2.3. Numerical Implementation

2.3.1. Metric Terms

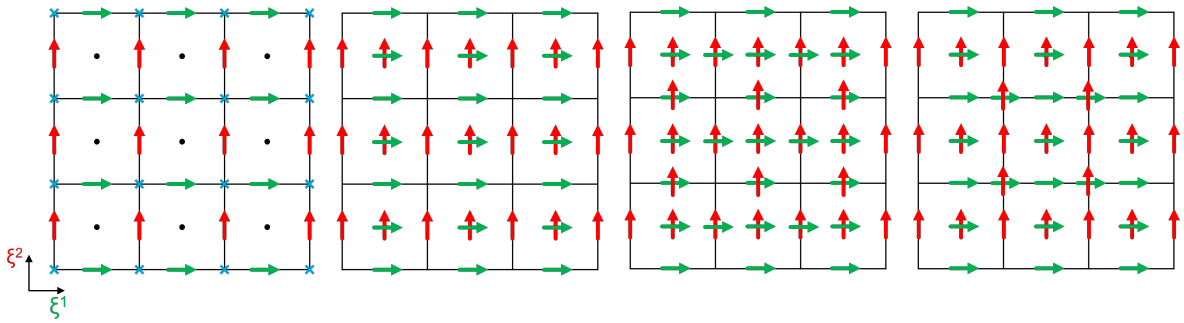

Figure 2.1: Determination of basevectors, FLTR: Finite differencing, Interpolation to cell centres, interpolation to cell faces, interpolation to vertices

The metric quantities introduced in the previous section are computed as follows in order to discretise Equation 2.1, Equation 2.2 and boundary conditions. The process is visualised in Figure 2.1. First, $\vec{a}_{(\alpha)}$ are computed in their corresponding tangent faces through finite differencing of the vertex locations. Through linear interpolation of these vectors to the cell centres, the full basis becomes available at the cell centres. A second interpolation of the missing base vector to the cell faces then provides a complete basis at the cell faces as well. With the full basis, $g_{\alpha\beta}$, $g^{\alpha\beta}$ and $\sqrt{g*}$, can be computed. At the boundaries of the computational domain, the interpolation cannot be fully performed, resulting in

missing base vectors at the outer cell faces. However, the use of ghost cells, a layer of one cell wide around the domain, prevents this from causing issues.

For the computation of Christoffel symbols, differencing of covariant metric tensor $g_{\alpha\beta}$ is required in two curvilinear coordinate directions. As will become apparent, the Christoffel symbols will be required in the cell faces to implement higher-order boundary conditions. To obtain Christoffel symbols in the cell faces, linear interpolation of base vectors from the cell faces to the cell vertices is performed, after which $g_{\alpha\beta}$ can be computed there. Finite differencing between cell centres and vertices then yields the necessary derivatives of $g_{\alpha\beta}$, from which the Christoffel symbols in the cell faces are computed.

2.3.2. Discretisation

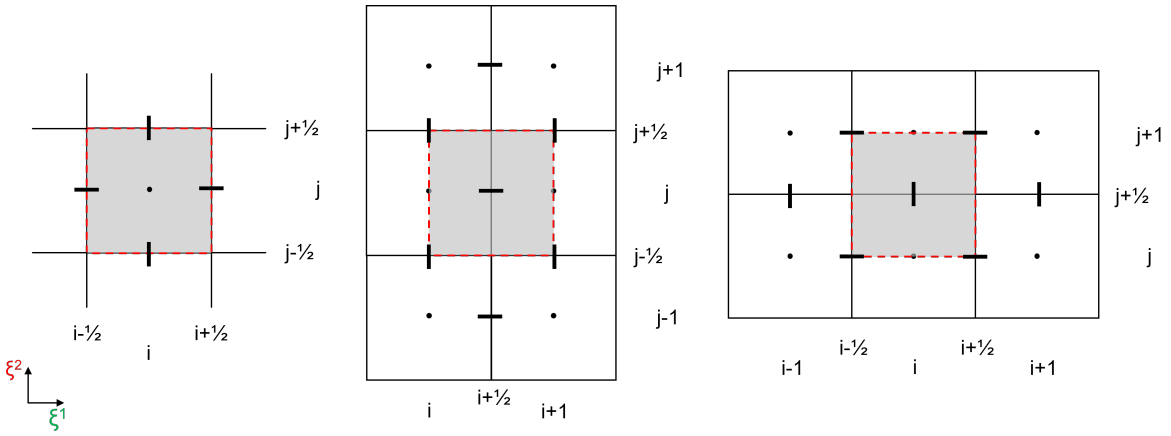

Figure 2.2: Staggered computational grid cells and indexing. FLTR; p cell, V^1 cell, V^2 cell

To discretise Equation 2.1 and 2.2, a Finite Volume (FV) discretisation is employed on a staggered grid. The pressure is stored at the cell centres, while the scaled contravariant velocity components $V^\alpha = U^\alpha\sqrt{g*}$ are stored at the corresponding cell faces. This follows the convention of Kassels and Segal [25] and allows for an accurate discretisation without Christoffel symbols required in the interior. Also, the choice of variables allows for exact recovery of a constant velocity field in the cell centres [24]. The staggered grid cell stencils are depicted in Figure 2.2. The semi-discrete system of equations is given in Equation 2.9-2.11. The notation $|_{i,j}$ is used to indicate the location of variables and their respective offset in the staggered grid.

$$\frac{\partial p}{\partial t}|_{i,j} = \frac{Gh}{\sqrt{g*}|_{i,j}}\left(V^1|_{i-\frac{1}{2},j} - V^1|_{i+\frac{1}{2},j} + V^2|_{i,j-\frac{1}{2}} - V^2|_{i,j+\frac{1}{2}}\right) \tag{2.9}$$

$$\frac{\partial V^1}{\partial t}|_{i+\frac{1}{2},j} = (p_{i,j} - p_{i+1,j})(g^{11}\sqrt{g*})|_{i+\frac{1}{2},j} + (p_{i+\frac{1}{2},j-\frac{1}{2}} - p_{i+\frac{1}{2},j+\frac{1}{2}})(g^{12}\sqrt{g*})|_{i+\frac{1}{2},j} \tag{2.10}$$

$$\frac{\partial V^2}{\partial t}|_{i,j+\frac{1}{2}} = (p_{i-\frac{1}{2},j+\frac{1}{2}} - p_{i+\frac{1}{2},j+\frac{1}{2}})(g^{21}\sqrt{g*})|_{i,j+\frac{1}{2}} + (p_{i,j} - p_{i,j+1})(g^{22}\sqrt{g*})|_{i,j+\frac{1}{2}} \tag{2.11}$$

In Equation 2.10 and 2.11, pressures values in the vertices are required. These are obtained through linear interpolation, as in Kassels and Segal [25].

For the discretisation in time, an Implicit Explicit (IMEX) scheme will be used. In the IMEX scheme, the pressure $p|^{n+1}$ is evaluated explicitly based on velocities from the previous time step $V^\alpha|^n$. This pressure $p|^{n+1}$ will be used to implicitly advance the velocity; $V^\alpha|^{n+1}$.

In Appendix B, the FV discretisation of the linearised shallow water equations is given. In Appendix C, computation of the metric values and the stencils are described.

2.4. Grid

To apply a higher-order GABC on a circular boundary while keeping a rectangular interior, a computational plus-shaped grid will be used. The curvilinear grid is mapped to the computational grid, these are depicted in Figure 2.3a and 2.3b respectively. The computational grid is equidistant with unit spacing. The curvilinear grid was generated using open-source mesh toolbox GibbonMesh's [29]. To create the grid, the radius R_d, the amount of rectangular interior cells along one direction N_e can be varied. The ratio of rectangular interior f_d determines the amount of cell layers to map to the circular boundary; N_r. One layer of ghost cells was added to the grid based on the local cell size normal to the boundary. The internal boundaries of the plus-shaped grid are marked blue in Figure 2.3. These will be referred to as slits. In the slits, the computational domain needs to be coupled to obtain a continuous domain.

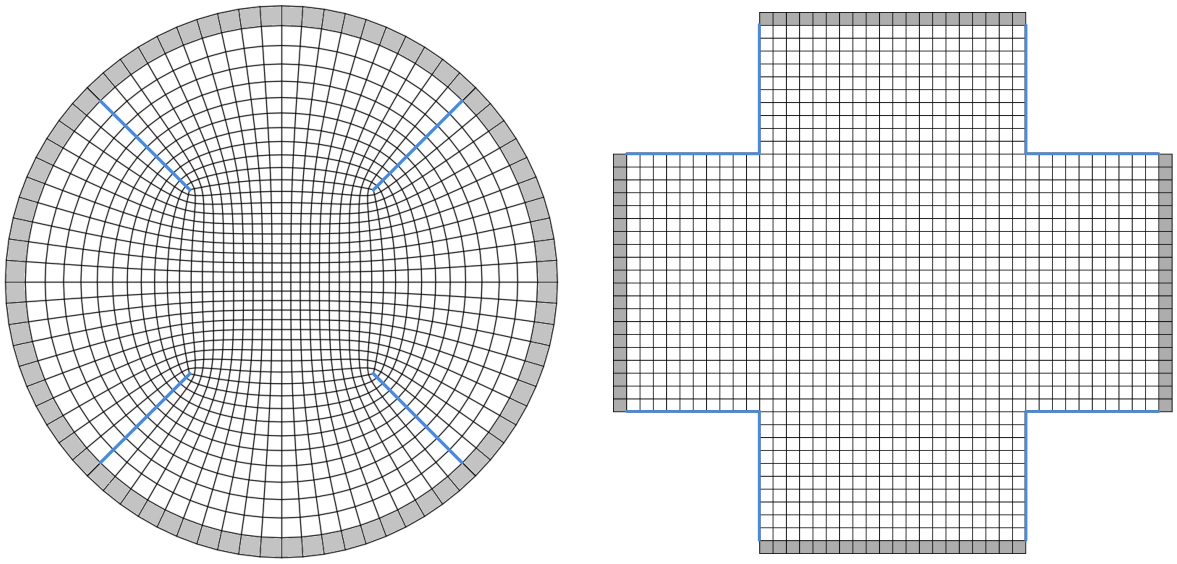

(a) Curvilinear grid

(b) Computational plus-shaped grid

Figure 2.3: Mapping between curvilinear grid and computational grid. Grey cells are pressure ghost cells. Blue lines indicate the slits.

The first challenge with the grid coupling is in determining the metric in the slit. With the ordinary interpolation routine, depicted in Figure 2.1, base vectors are missing for interpolation to the cell faces in the slit. This was solved by using the equivalent base vector at the other side of the slit. As two coordinate directions are coupled, the base vectors across the slit represent similar metric information. Depending on the slit location, a sign correction was applied. The vectors near the slit are visualised in Figure 2.4. Using the equivalent base vectors in interpolation to vertices and cell faces, there are no limitations in determining metric information near the slit.

The second challenge is the stencil of the pressures and velocities around the slit. To complete all pressure stencils near the slit, the V^α components that are defined on the slit faces are coupled with their cross slit counterpart, in a similar fashion as the base vector interpolation. To complete the velocity stencils, pressures from across the slit are taken that are adjacent to the V^α cell in the curvilinear grid. This is visualised in Figure 2.5.

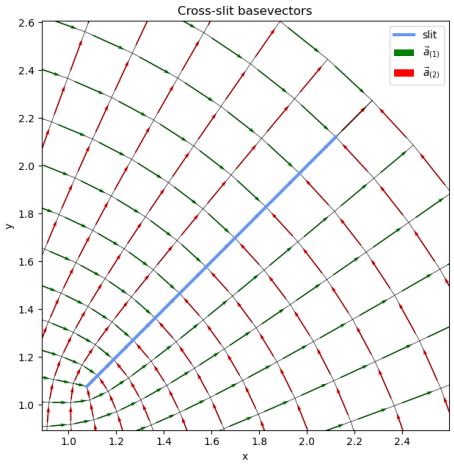

Figure 2.4: Base vectors near the slit. It can be seen that $\vec{a}_{(1)}$ represents similar metric information with opposite sign of $\vec{a}_{(2)}$.

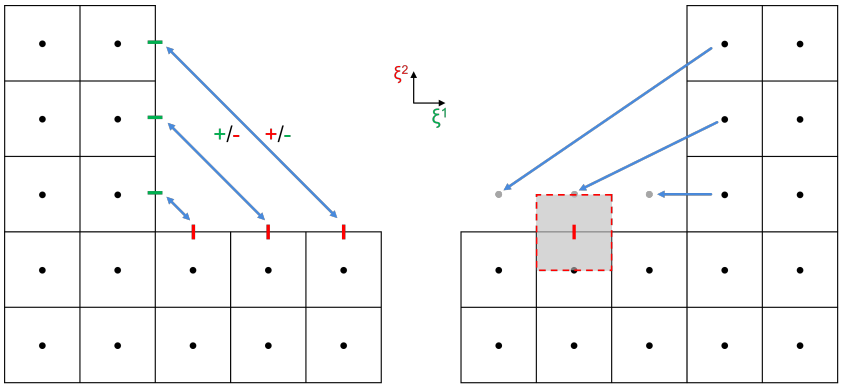

Figure 2.5: Velocity (left) and pressure (right) coupling in the slit.

The third challenge is the stencil of V^α cells which require a pressure value at the vertex where the slit starts. The ordinary stencil uses a four point interpolation to obtain a pressure at vertices. At the interior corner, a three point interpolation is used, as shown in Figure 2.6.

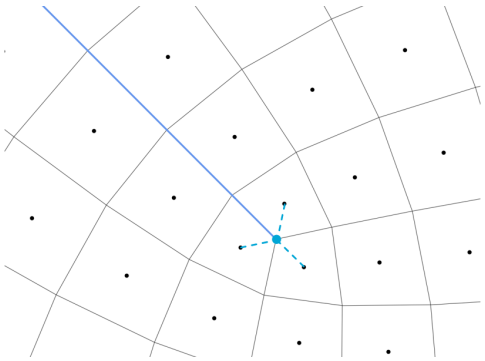

Figure 2.6: Pressure interpolation in interior slit corner.

A more detailed description of the slit coupling is given in Appendix C.

2.5. Interior Verification

To verify the internal discretisation, the implementation is benchmarked to a Cartesian FV discretisation on a staggered equidistant grid. The Cartesian grid spacing was chosen such that the interior of Figure 2.3a matches the Cartesian grid (Tables 2.2 and 2.3). A circular wave is introduced by initiating a pressure variation using the following equations:

$$Envelope\,(t) = S\left(\frac{t - t_{start}}{t_{intro}}\right)\left[1 - S\left(\frac{t - (t_{intro} + t_{plateau})}{t_{outro}}\right)\right] \tag{2.12}$$

$$S(t') = \begin{cases} 0 & t' \leq 0 \\ \dfrac{e^{-1/t'}}{e^{-1/t'} + e^{-1/(1-t')}} & 0 < t' < 1 \\ 1 & t' \geq 1 \end{cases} \tag{2.13}$$

$$p_{init}(t) = Envelope\,(t) \cdot A \cdot \sin(\omega t) \tag{2.14}$$

The wave is initiated by adding p_{init} (Equation 2.14) to the four centre cells at each time step. To limit introduction effects, the wave is gradually introduced using Equation 2.12. The comparison is performed before the wavefront reaches the boundary at $t = 0.70$. The results of the Cartesian simulation are resampled onto the curvilinear grid by bi-cubic spline interpolation for a point-to-point analysis. The parameters for the simulations are stated in Table 2.1.

Parameter	Symbol	Value	Unit
Gravitational constant	G	9.81	ms^{-2}
Water depth	h	2.0	m
Wave speed	$c = \sqrt{Gh}$	4.429	ms^{-1}
Amplitude	A	3.0	$kg\,ms^{-2}$
Envelope intro time	t_{intro}	0.339	s
Envelope outro time	t_{outro}	0.339	s
Envelope full amplitude time	$t_{plateau}$	0.677	s
Wave frequency	ω	9.277	$rad\,s^{-1}$
Simulated time	t_{tot}	0.7	s
Time step	Δt	0.0001	s

Table 2.1: General simulation parameters for interior verification test

Parameter	Symbol	Value	Unit
Domain Radius	R_d	3.0	m
Interior ratio	f_d	0.5	[-]
Centre Cell size x	Δx	0.00530	m
Centre Cell size y	Δy	0.00530	m
Interior cell layers	N_e	400	[-]
Radial layers	N_r	200	[-]

Table 2.2: Curvilinear grid settings for interior verification

Parameter	Symbol	Value	Unit
Domain length	L_x	6.01394	m
Domain width	L_y	6.01394	m
Cell size x	Δx	0.00530	m
Cell size y	Δy	0.00530	m
Cells in x dir	N_x	1134	[-]
Cells in y dir	N_y	1134	[-]

Table 2.3: Cartesian grid settings for interior verification

Results

The accuracy of the curvilinear implementation is evaluated using error norms, using the relative L^2 and absolute L^∞ pressure errors (Figure 2.7). The relative L^2 error remains below 0.014% throughout the simulation, demonstrating high consistency between the two methods.

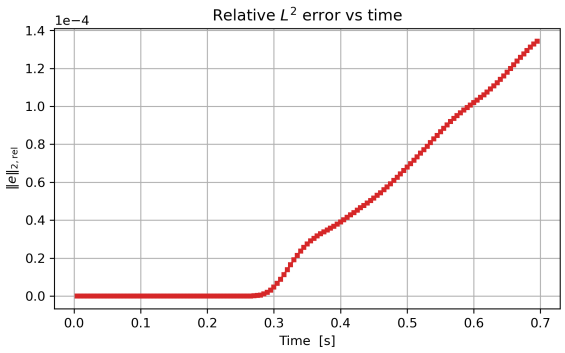

(a) Relative L^2 pressure error over time.

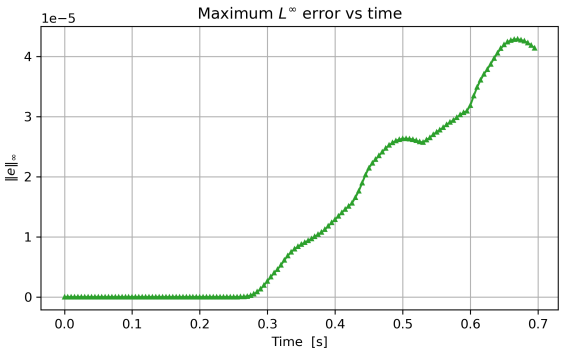

(b) Absolute L^∞ pressure error over time.

Figure 2.7: Error before $t = 0.70$. Error axes are scaled.

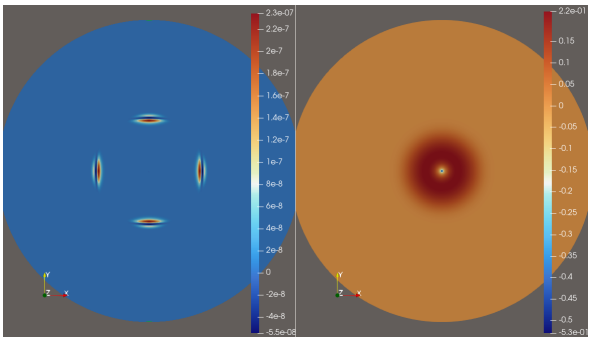

(a) Error caused by curvilinear grid stretching at t=0.275.

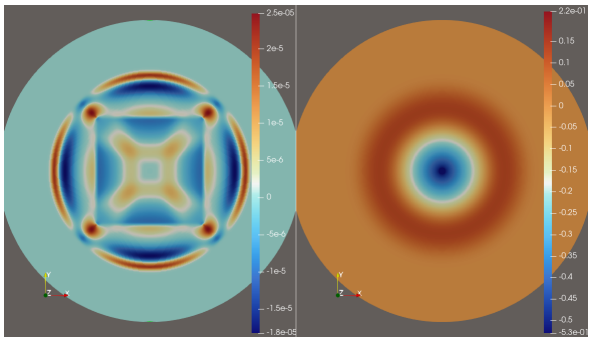

(b) Corner stencil error at t=0.475

Figure 2.8: Main error sources. Left part of (sub)image shows error in pressure at simulation instant described by the right part of the (sub)image

As the wavefront exits the uniform rectangular interior of the curvilinear grid, the L^2 error increases slightly due to numerical dispersion (Figure 2.8a). The L^∞ error exhibits peaks at $t \approx 0.475\,\mathrm{s}$ and $t \approx 0.660\,\mathrm{s}$, which coincides with the passage of the maximum pressure gradient over the interior slit corners. This is visualised in Figure 2.8b, in which the wavefront has a phase lag where it passed the corner with respect to the rest of the wave front. However, these local errors remain the same order of magnitude as the numerical dispersion errors.

The relative L^2 error remains low, and the maximum absolute error is of the same order of a known numerical artefact inherent to the discretisation. Therefore, the error levels verify that the curvilinear discretisation and the slit-coupling are implemented accurately. The methodology is therefore suitable for evaluating the performance of higher-order GABCs.

2.6. Generating Absorbing Boundary Conditions

Now that the interior coupling method has been verified, boundary conditions can be implemented with confidence. At the boundary, higher-order GABCs are implemented to circumvent corner conditions using generalised curvilinear coordinates. The boundary condition is applied exactly at the cell faces, which correspond to the locations of the contravariant velocity components. This is illustrated in Figure 2.9. The boundary condition is applied through updates of the pressure ghost cells, such that the linearly interpolated pressure at the boundary face satisfies the GABC. This pressure update is given by Equation 2.15. By updating the pressures, the velocity stencils near the boundary are complete and can be left unchanged. The pressure interpolation at the boundary face is used for all GABC formulations presented in this methodology. Therefore this interpolation is verified before introducing GABC theory and its numerical implementation.

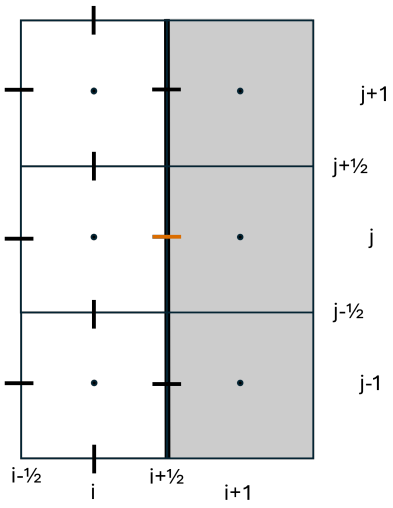

Figure 2.9: Computational grid and stencil at boundary. Grey cells are ghost cells.

$$p|^{n+1}_{i+\frac{1}{2},j} = \frac{1}{2}(p|^{n+1}_{i,j} + p|^{n+1}_{i+1,j}) \quad \Rightarrow \quad p|^{n+1}_{i+1,j} = 2\, p|^{n+1}_{i+\frac{1}{2},j} - p|^{n+1}_{i,j} \tag{2.15}$$

2.6.1. Verification of Pressure Interpolation

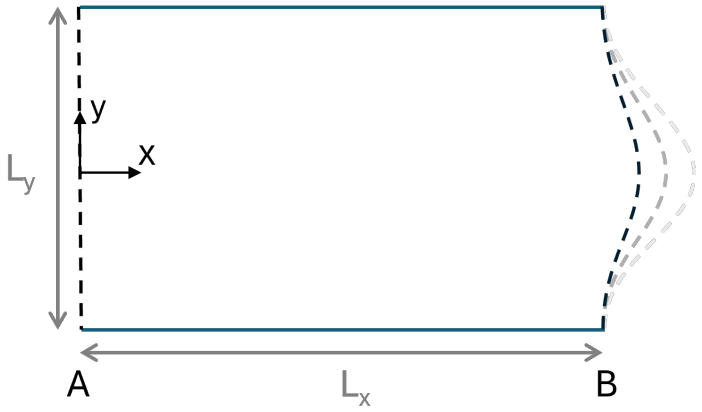

Figure 2.10: Domain with increasing amounts of curvature at boundary B

The pressure interpolation stated in Equation 2.15 is verified for curved boundaries by a convergence test. For this, the domain in Figure 2.10 was set up by transforming a rectangular computational grid with $\xi^\alpha \in \{0, ..., N_{\xi\alpha}\}$ to a curved grid based on Equation 2.16. To ensure orthogonality at the top and bottom boundary, the mapping is applied only on the interior computational domain. Ghost cell layers are transformed afterwards by extrapolation from neighbouring interior cells.

$$x(\xi^1, \xi^2) = L_x \frac{\xi^1}{N_{\xi^1}} + \beta \exp\left(-\frac{(\xi^2 - \frac{N_{\xi^2}}{2})^2}{2\,(0.2)^2}\right) W\left(\frac{\xi^2 - \frac{N_{\xi^2}}{2}}{N_{\xi^2}}\right)\left(\frac{\xi^1}{N_{\xi^1}}\right)^2 \tag{2.16}$$

$$y(\xi^1, \xi^2) = L_y \frac{\xi^2 - \frac{N_{\xi^2}}{2}}{N_{\xi^2}} \tag{2.17}$$

$$W(a) = \left(3a^2 - 2a^3\right)\left(1 - 3a^2 + 2a^3\right) \tag{2.18}$$

For a meaningful evaluation of pressure gradients, bottom friction C_w was added to Equation 2.2, resulting in Equation 2.20. A pressure gradient is prescribed through boundaries A and B using Equation 2.15. The prescribed value depends on x location of the boundary face and is given by Equation 2.19. The grid consists of orthogonal cells at the top and bottom boundary. Therefore, by copying the interior value to update the ghost cells, frictionless walls can be set up. This implies a zero pressure gradient normal to the boundary.

$$p_A + (p_B - p_A)\frac{x}{L_x} \tag{2.19}$$

The imposed pressure gradient induces a flow from A to B. Due to bottom friction, the velocity converges to a steady-state value. The velocity in x direction will converge to $0.555^{m/s}$ based on Equation 2.21 and the parameters in Table 2.4. The velocity in y direction will converge to zero. 50 seconds were simulated to reach a converged simulation.

$$\frac{\partial \vec{u}}{\partial t} + (\vec{\nabla} p) = -C_w \vec{u} \tag{2.20}$$

$$u_x = \frac{p_B - p_A}{L_x}\frac{1}{-C_w} \tag{2.21}$$

Parameter	Symbol	Value	Unit
Gravitational constant	G	9.81	$m\,s^{-2}$
Water depth	h	2.0	m
Wave speed	$c = \sqrt{Gh}$	4.429	$m\,s^{-1}$
Domain length	L_x	6.0	m
Domain width	L_y	5.0	m
Bottom friction coeff	C_w	9.0	s^{-1}
Overpressure	p_A	50.0	$kg\,m^{-1}s^{-2}$
Underpressure	p_B	20.0	$kg\,m^{-1}s^{-2}$
Simulated time	t_{tot}	50.0	s
Time step	Δt	0.0001	s

Table 2.4: Simulation parameters for pressure interpolation test

The simulation was performed for three curvature intensities in Equation 2.16 ($\beta = 1.0, 2.0, 3.0$) across three grid resolutions ($N_{\xi 1}, N_{\xi 2} = 120, 100$, $170, 140$ and $240, 200$). Other constant simulation parameters are stated in Table 2.4. The pressures at the two boundaries were introduced gradually using Equation 2.12. In all cases, the solution converged to a steady state within $t = 50\,\text{s}$.

The resulting maximum velocity deviations from the analytical solution are summarized in Table 2.5. While the absolute error increases with the boundary curvature β, it shows a consistent second-order convergence as the grid is refined, visualised in Figure 2.12. These results verify that the pressure interpolation scheme is robust for curved boundaries, forming a rigorous basis for applying higher-order GABCs. A more elaborate description of the performed test is given in Appendix D.

$N_{\xi 1}$	120		170		240	
β	u_x	u_y	u_x	u_y	u_x	u_y
1.0	3.070E-05	4.659E-06	1.558E-05	2.364E-06	7.559E-06	1.144E-06
2.0	1.377E-04	2.962E-05	6.979E-05	1.556E-05	3.394E-05	7.720E-06
3.0	3.424E-04	8.685E-05	1.741E-04	4.519E-05	8.501E-05	2.232E-05

Table 2.5: Maximum absolute errors based on analytical values for different grid resolutions $N_{\xi 1}$ and boundary curvatures β

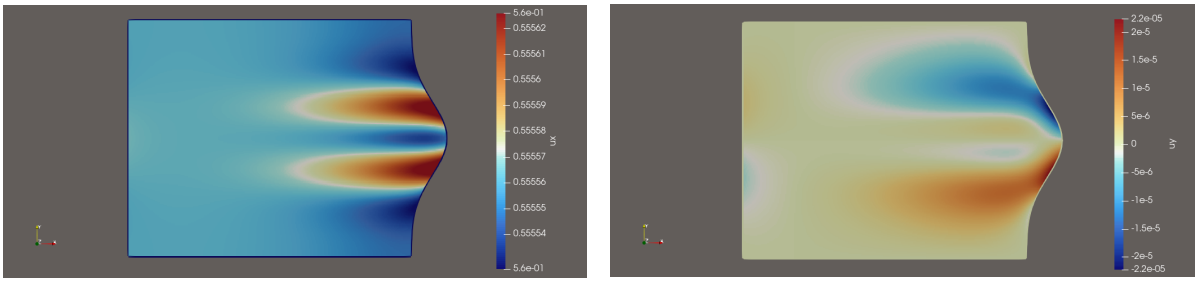

(a) Converged result of u_x

(b) Converged result of u_y

Figure 2.11: Converged simulation with curvature β = 3.0 and grid resolution $N_{\xi 1}$ = 240. Note that deviations are small.

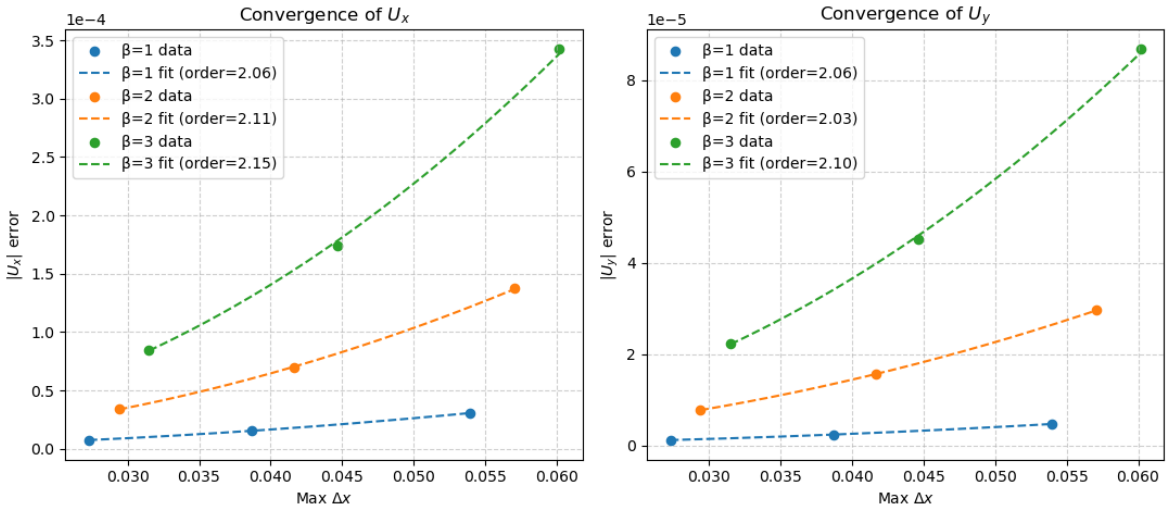

Figure 2.12: Absolute error convergence trend for different grids. Error axes are scaled.

2.6.2. First-Order Generating Absorbing Boundary Condition

Similar to Wellens and Borsboom [37], the first-order GABC will be derived from the wave equation in potential form normal to the boundary (2.22). Factoring gives the Sommerfeld condition (2.24), in which c_0 is a coefficient. c_0 represents the apparent velocity that can be tuned for the angle of incidence of the wave with the boundary:

$$\left(\frac{\partial^2}{\partial t^2} - c^2 \frac{\partial^2}{\partial n^2}\right)\Phi = 0 \tag{2.22}$$

$$\left(\frac{\partial}{\partial t} - c\frac{\partial}{\partial n}\right)\left[\left(\frac{\partial}{\partial t} + c\frac{\partial}{\partial n}\right)\Phi\right] = 0 \tag{2.23}$$

$$\left(\frac{\partial}{\partial t} + c_0\frac{\partial}{\partial n}\right)\Phi = 0 \tag{2.24}$$

In order to express Equation 2.24 in terms of solution variables, linear potential theory can be used. The derivative in time of Φ can be expressed as pressure. Using the linearised Bernoulli equation, with the dynamic boundary condition for free-surface flow applied, the pressure head p can be defined by Equation 2.25. The gradient, $\vec{\nabla}\Phi$, gives the velocity vector. Projection onto the outward normal gives the velocity in that direction, u_n (2.26).

$$p = G\zeta = -\frac{\partial \Phi}{\partial t} \tag{2.25}$$

$$u_n = \frac{\partial \Phi}{\partial n} = \vec{n} \cdot \vec{\nabla} \Phi \tag{2.26}$$

By applying a Sommerfeld BC, outgoing waves can be absorbed. Instead of prescribing a zero right hand side in 2.24, also a non-zero residual can be prescribed. If this residual is set to match a desired incoming wave, this wave will be introduced at the boundary. This is done through application of the same operator on an incoming wave, similar to how Wellens and Borsboom [37] define their GABC. The total potential is represented as Φ, and the incoming wave is represented by Φ_{in}.

$$\left(\frac{\partial}{\partial t} + c_0 \frac{\partial}{\partial n}\right) \Phi = \left(\frac{\partial}{\partial t} + c_0 \frac{\partial}{\partial n}\right) \Phi_{in} \tag{2.27}$$

$$\Phi_{in} = A e^{i(\vec{k} \cdot \vec{x} - \omega t + \epsilon)} = A e^{i(kx \cos \mu + ky \sin \mu - \omega t + \epsilon)} \tag{2.28}$$

The right hand side of Equation 2.27 is evaluated analytically at each boundary point. Because an analytical description of Φ_{in} is available, the right hand side derivatives can be computed in a straight forward fashion using the real part. One example of an introduced wave is given in Equation 2.28, in which A is the wave potential amplitude, k is the wave number, $\vec{k}$ is the wave vector, ω the angular wave frequency, μ the wave direction and ϵ is a desired phase of the wave. For every boundary cell, the dot product of the wave vector with the outward normal is evaluated. A negative value indicates an incoming wave, for which the right hand side will be computed analytically. Otherwise, the right-hand side (RHS) is set to zero and the GABC reduces to an ABC. The GABC in Equation 2.27 will be referred to as SFD.

Numerical Implementation

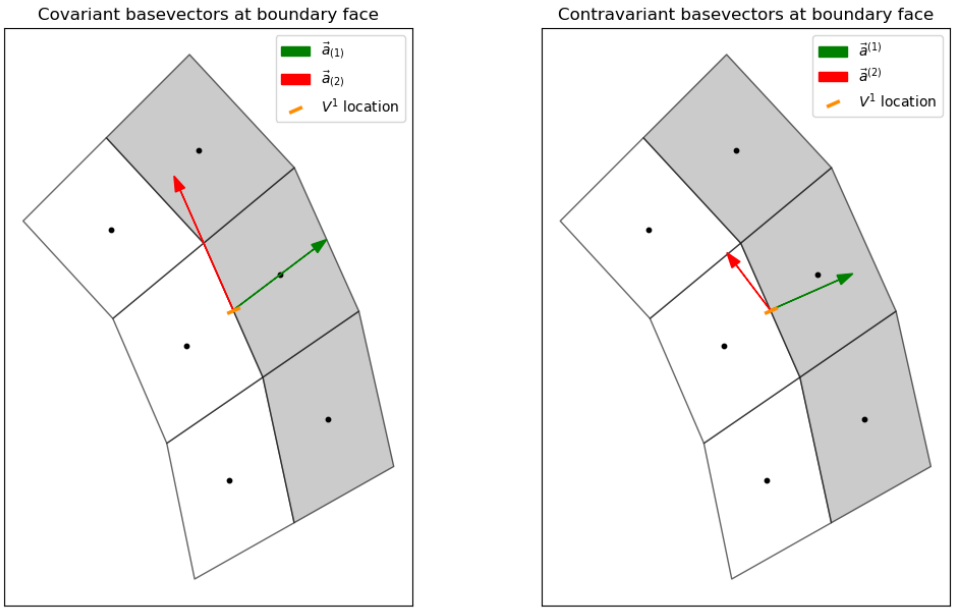

Figure 2.13: Base vectors at boundary face. Grey cells are ghost cells.

The implementation of Equation 2.27 is similar to that of Wellens and Borsboom [37] but in generalised curvilinear coordinates. It will be demonstrated for a ξ^1 = constant face, but is equivalent for other faces. First, Equation 2.26 will be written in curvilinear coordinates. It is used that the contravariant base vector aligns with the unit outward normal, as can be seen in Figure 2.13.

$$\frac{\partial \Phi}{\partial n} = \vec{n} \cdot \vec{\nabla}\Phi = n_1 \vec{a}^{(1)} \cdot (\vec{a}^{(\alpha)} \frac{\partial \Phi}{\partial \xi^\alpha}) = n_1 (g^{1\alpha} U_\alpha) = n_1 U^1 \tag{2.29}$$

$$||\vec{n}|| = 1 \quad \Rightarrow \quad n_1 = \frac{1}{\sqrt{\vec{a}^{(1)} \cdot \vec{a}^{(1)}}} = \frac{1}{\sqrt{g^{11}}} \tag{2.30}$$

Equation 2.25, 2.29 and the analytic RHS will be substituted in Equation 2.27. A formulation for the pressure ghost, with all elements defined at the same time level, is then given by:

$$p|^{n+1}_{i+1,j} = -p|^{n+1}_{i,j} + 2c_0 \; n_1 \; U^1|^{n+1}_{i+\frac{1}{2},j} - 2RHS \tag{2.31}$$

A relation needs to be found to substitute $U^1|^{n+1}_{i+\frac{1}{2},j}$. For this, the momentum equation normal to the boundary is evaluated explicitly:

$$\vec{n} \cdot \left(\frac{\partial \vec{u}}{\partial t} + (\vec{\nabla} p) \right) = n_1 \frac{\partial U^1}{\partial t} + \frac{\partial p}{\partial n} = n_1 \frac{\partial U^1}{\partial t} + n_1 \left(g^{\beta 1} \frac{\partial p}{\partial \xi^\beta} \right) \tag{2.32}$$

$$n_1 U^1|^{n+1}_{i+\frac{1}{2},j} = n_1 U^1|^{n}_{i+\frac{1}{2},j} - \Delta t \; n_1 \left(g^{11} \frac{\partial p}{\partial \xi^1}|^{n}_{i+\frac{1}{2},j} + g^{21} \frac{\partial p}{\partial \xi^2}|^{n}_{i+\frac{1}{2},j} \right) \tag{2.33}$$

Equation 2.33 is substituted in 2.31. As metric scaled contravariant velocity components are used as solution variables, substitution of $U^1 = \frac{V^1}{\sqrt{g*}}$ gives the update for the ghost pressure value corresponding to Equation 2.27. The pressure derivatives are found by finite differencing on the computational equidistant grid with unit spacing. $p|^{n}_{i+\frac{1}{2},j\pm\frac{1}{2}}$ can be found by four point interpolation of the surrounding values. For boundary faces near the slit, the procedure depicted in Figure 2.5 is used for a complete pressure stencil.

A more detailed derivation is given in Appendix E.

$$p|^{n+1}_{i+1,j} = -p|^{n+1}_{i,j} + 2c_0 \left[\; n_1 \frac{V^1}{\sqrt{g*}}|^{n}_{i+\frac{1}{2},j} - \Delta t \; n_1 \left(g^{11} \frac{\partial p}{\partial \xi^1}|^{n}_{i+\frac{1}{2},j} + g^{21} \frac{\partial p}{\partial \xi^2}|^{n}_{i+\frac{1}{2},j} \right) \right] - 2RHS \tag{2.34}$$

$$\frac{\partial p}{\partial \xi^1}|^{n}_{i+\frac{1}{2},j} = (p|^{n}_{i+1,j} - p|^{n}_{i,j}) \tag{2.35}$$

$$\frac{\partial p}{\partial \xi^2}|^{n}_{i+\frac{1}{2},j} = (p|^{n}_{i+\frac{1}{2},j+\frac{1}{2}} - p|^{n}_{i+\frac{1}{2},j-\frac{1}{2}}) \tag{2.36}$$

2.6.3. Higher-Order Generating Absorbing Boundary Conditions

Engquist and Majda [10] developed a family of ABCs based on Padé series expansion of the non-local boundary operator. Formulations were derived both for a constant coefficient wave equation, leading to Cartesian (planar) boundary operators, and for variable-coefficient wave equations, yielding operators suited for circular boundaries.

For Cartesian boundaries, the first-order approximation reduces to the SFD BC, while higher-order approximations improve absorption for a wider range of incidence angles. For circular boundaries, the first-order approximation is highly absorbing for cylindrical waves with the boundary placed far away from the centre. The second-order approximation improves absorption with angular dependence, when the wave is not fully cylindrical.

In this work, second-order formulations of the prior are adapted and implemented in generalised curvilinear coordinates on a circular boundary. In Appendix F, this is worked out in detail. The continuous

forms are stated below. The GABC based on planar boundaries will be referred to as Planar Engquist-Majda (PEM) (2.37) and the circular variant as Circular Engquist-Majda (CEM) (2.38).

$$\left(-\frac{\partial^2}{\partial t^2} - c\frac{\partial^2}{\partial t \partial n} + \frac{c^2}{2}\frac{\partial^2}{\partial \tau \partial \tau}\right)\Phi = \left(-\frac{\partial^2}{\partial t^2} - c\frac{\partial^2}{\partial t \partial n} + \frac{c^2}{2}\frac{\partial^2}{\partial \tau \partial \tau}\right)\Phi_{in} \tag{2.37}$$

$$\begin{aligned}\left(\frac{\partial^3}{\partial t^3} + c\frac{\partial^3}{\partial n \partial t^2} - \frac{c^2}{2}\frac{\partial^3}{\partial t \partial \tau \partial \tau} + \frac{c}{2R_d}\frac{\partial^2}{\partial t^2} + \frac{c^3}{2R_d}\frac{\partial^2}{\partial \tau \partial \tau}\right)\Phi = \\ \left(\frac{\partial^3}{\partial t^3} + c\frac{\partial^3}{\partial n \partial t^2} - \frac{c^2}{2}\frac{\partial^3}{\partial t \partial \tau \partial \tau} + \frac{c}{2R_d}\frac{\partial^2}{\partial t^2} + \frac{c^3}{2R_d}\frac{\partial^2}{\partial \tau \partial \tau}\right)\Phi_{in}\end{aligned} \tag{2.38}$$

Due to the staggered variable arrangement, interpolation of tangential velocity components is not available at the boundary. Both formulations are therefore rewritten entirely in terms of pressure. To enable this, auxiliary variable $q = \frac{\partial^2 \Phi}{\partial \tau \partial \tau}$ is introduced. Using Equation 2.25 and an analytical evaluation of the right-hand side, the boundary system corresponding to PEM can be written as:

$$\frac{\partial p}{\partial t} = -c\frac{\partial p}{\partial n} - \frac{c^2}{2}q + RHS \tag{2.39}$$

$$\frac{\partial q}{\partial t} = \frac{\partial^3 \Phi}{\partial t \partial \tau \partial \tau} = -\frac{\partial^2 p}{\partial \tau \partial \tau} \tag{2.40}$$

and the system corresponding to CEM:

$$\frac{\partial^2 p}{\partial t^2} = -c\frac{\partial^2 p}{\partial n \partial t} + \frac{c^2}{2}\frac{\partial^2 p}{(\partial \tau)^2} - \frac{c}{2R_d}\frac{\partial p}{\partial t} + \frac{c^3}{2R_d}q - RHS \tag{2.41}$$

$$\frac{\partial q}{\partial t} = -\frac{\partial^2 p}{\partial \tau \partial \tau} \tag{2.42}$$

Numerical Implementation
The implementation of PEM and CEM will be demonstrated for a ξ^1-constant face, as seen in Figure 2.9. Extensive derivations for this implementation are given in Appendix G. For the implementation, it is used that the normal vector aligns with $\vec{a}^{(1)}$, and the tangential vector at the boundary aligns with $\vec{a}_{(2)}$. This is visualised in Figure 2.13.

Explicit updates of the pressure ghost cell are desired, for which each system of equations is discretised explicitly in time. The auxiliary variable is updated first, after which it is used in the ghost cell update. Both systems are first discretised in time, after which the discretisation of the common spatial derivative building blocks are shown. Equation 2.15 is used to obtain the desired value for the ghost cell.

The explicit update for the ghost cell for PEM reads:

$$p|^{n+1}_{i+1,j} = -p|^{n+1}_{i,j} + 2p|^{n}_{i+\frac{1}{2},j} + 2\Delta t\left(-c\frac{\partial p}{\partial n}|^{n}_{i+\frac{1}{2},j} - \frac{c^2}{2}q|^{n+1}_{i+\frac{1}{2},j} + RHS\right) \tag{2.43}$$

$$q|^{n+1}_{i+\frac{1}{2},j} = q|^{n}_{i+\frac{1}{2},j} - \Delta t\frac{\partial^2 p}{\partial \tau \partial \tau}|^{n}_{i+\frac{1}{2},j} \tag{2.44}$$

The explicit update for the ghost cell for CEM is given below. To keep the equation insightful, the staggered location of the boundary face $|_{i+\frac{1}{2},j}$ is indicated as $|_b$ and the update is split up into a system of equations:

$$p|_{i+1,j}^{n+1} = 2p|_b^{n+1} - p|_{i-1,j}^{n+1} \tag{2.45}$$

$$p|_b^{n+1} = 2p|_b^n - p|_b^{n-1} + (\Delta t)^2 \left(-c\frac{\partial^2 p}{\partial t \partial n}|_b^n + \frac{c^2}{2}\frac{\partial^2 p}{\partial \tau \partial \tau}|_b^n - \frac{c}{2R_d}\frac{\partial p}{\partial t}|_b^n + \frac{c^3}{2R_d} q|_b^{n+1} - RHS \right) \tag{2.46}$$

$$\frac{\partial^2 p}{\partial t \partial n}|_b^n = \frac{\frac{\partial p}{\partial n}|_b^n - \frac{\partial p}{\partial n}|_b^{n-1}}{\Delta t} \tag{2.47}$$

$$\frac{\partial p}{\partial t}|_b^n = \frac{p|_b^n - p|_b^{n-1}}{\Delta t} \tag{2.48}$$

$$q|_b^{n+1} = q|_b^n - \Delta t \frac{\partial^2 p}{\partial \tau \partial \tau}|_b^n \tag{2.49}$$

The spatial derivative building blocks are implemented as follows. The pressure normal derivative is evaluated as in Equation 2.34. The second-order tangential derivative for scalars, for which an extensive derivation is given in Appendix G, can be defined as follows:

$$\frac{\partial^2 p}{\partial \tau \partial \tau} = \frac{1}{g_{22}} \left(\frac{\partial^2 p}{\partial \xi^2 \partial \xi^2} - \frac{\Gamma_{222}}{g_{22}} \frac{\partial p}{\partial \xi^2} \right) \tag{2.50}$$

The pressure derivatives are evaluated by finite differencing of interpolated pressure values. The computational grid with unit spacing is visualised in Figure 2.9. The pressure interpolation is verified in subsection 2.6.1. For boundary faces near the slit, the procedure depicted in Figure 2.5 is used for a complete pressure stencil.

$$\frac{\partial^2 p}{\partial \xi^2 \partial \xi^2}|_{i+\frac{1}{2},j} = p|_{i+\frac{1}{2},j+1} - 2\, p|_{i+\frac{1}{2},j} + p|_{i+\frac{1}{2},j-1} \tag{2.51}$$

$$\frac{\partial p}{\partial \xi^2}|_{i+\frac{1}{2},j} = \frac{p|_{i+\frac{1}{2},j+1} - p|_{i+\frac{1}{2},j-1}}{2} \tag{2.52}$$

$$p|_{i+\frac{1}{2},j} = \frac{p|_{i,j} + p|_{i+1,j}}{2} \tag{2.53}$$

$$p|_{i+\frac{1}{2},j\pm1} = \frac{p|_{i,j\pm1} + p|_{i+1,j\pm1}}{2} \tag{2.54}$$

For each GABC, the RHS is evaluated with constant $\vec{k}$. Together with the second-order tangential derivative for scalars, the RHS for introduction of Φ_{in} (Equation 2.28) is given by Equation 2.55 and Equation 2.56 respectively. In these equations, co- and contravariant vector components are clarified using brackets in the sub- and superscripts.

For PEM:

$$RHS = \Re \left[-\omega^2 \Phi_{in} + c\omega n_{(1)} k^{(1)} \Phi_{in} + \frac{c^2}{2}\frac{\partial^2 \Phi_{in}}{\partial \tau \partial \tau} \right] \tag{2.55}$$

And CEM:

$$RHS = \Re \left[i\omega^3 \Phi_{in} - ic\omega^2 n_{(1)} k^{(1)} \Phi_{in} + \frac{i\omega c^2}{2}\frac{\partial^2 \Phi_{in}}{\partial \tau \partial \tau} - \frac{\omega^2 c}{2R_d}\Phi_{in} + \frac{c^3}{2R_d}\frac{\partial^2 \Phi_{in}}{\partial \tau \partial \tau} \right] \tag{2.56}$$

For both:

$$\frac{\partial^2 \Phi_{in}}{\partial \tau \partial \tau} = \frac{1}{g_{22}} \left(-(k_{(2)})^2 \Phi_{in} + ik^{(1)} \Gamma_{122} \Phi_{in} + ik^{(2)} \Gamma_{222} \Phi_{in} - \frac{\Gamma_{222}}{g_{22}} ik_{(2)} \Phi_{in} \right) \tag{2.57}$$

2.7. Reflection Tests

The absorption properties of the GABCs are assessed using a set of numerical experiments based on radiating point sources on different locations. The source is imposed by forcing the four cells closest to the prescribed location, following the same procedure as described in section 2.5 and using Equation 2.14. The introduced energy depends on the local cell size, but the forcing formulation is identical for all simulations. All parameters common to the reflection tests are listed in Table 2.6, while case-specific settings are reported in the corresponding test tables. Where possible, the results are compared to analytical relations. The following configurations are considered: a centred point source, an off-centre source and a long crested wave introduced over the boundary through a non-zero RHS. These tests quantify both normal and angle-dependent reflection behaviour. This behaviour is determined by the reflection coefficient, which is defined as:

$$R = \frac{||A_{refl}||}{||A_{out}||} \tag{2.58}$$

Parameter	Symbol	Value	Unit
Gravitational constant	G	9.81	ms^{-2}
Water depth	h	2.0	m
Wave speed	$c = \sqrt{Gh}$	4.429	ms^{-1}
Forcing amplitude	A	3.0	$kg\ ms^{-2}$
Domain radius	R_d	3.0	m
Time step	Δt	0.0001	s

Table 2.6: Common parameters used in all reflection tests.

2.7.1. Centred Source

The centred configuration allows expressing the combined outgoing and reflected pressure signal as a combination of an outward-radiating $H_0^{(1)}(kr)$ and inward-radiating Hankel function $H_0^{(2)}(kr)$. The pressure signal is real valued, so a Least Squares (LSQ) fit will be performed to find A_{out} and A_{refl} according to Equation 2.59. This LSQ fit is performed in a temporal and spatial frame that has a fully developed outgoing and reflected signal. This results in the values indicated in Table 2.7. For each cell in the frame, the Hankel coefficients based on radius from the source and analytical wave number k are determined. Due to numerical dispersion effects, radial averaging could cause lower reflection results. Therefore, the LSQ fit is performed for 36 angular sectors, each yielding a reflection coefficient and an R-squared value of fit accuracy. These will be averaged to report a final reflection coefficient and fit accuracy. Five grid refinements are tested.

$$p(r,t) = \Re\left[A_{out}H_0^{(1)}(kr)e^{-i\omega t} + A_{refl}H_0^{(2)}(kr)e^{-i\omega t}\right] \tag{2.59}$$

An analytical reflection coefficient is derived by expressing the total pressure field as a superposition of $H_0^{(1)}(kr)$ and $H_0^{(2)}(kr)$ and imposing a Sommerfeld BC at finite radius. The resulting expression depends on the non-dimensional parameter kr, where k is the wave number and r the radius. This analytical reflection coefficient represents the reflection level predicted for a Sommerfeld BC in continuous space and time. This result, given in Equation 2.60, is used as a reference for the numerical measurements. The test will be performed for a kr ratio of 18.85, for which the analytical reflection coefficient is 0.0133. The full derivation is provided in Appendix H.

$$R = \frac{||A_{refl}||}{||A_{out}||} = \frac{\left|\left|-iH_0^{(1)}(kr) - H_1^{(1)}(kr)\right|\right|}{\left|\left|iH_0^{(2)}(kr) + H_1^{(2)}(kr)\right|\right|} \tag{2.60}$$

Parameter	Symbol	Value	Unit
Source location	(x_s, y_s)	$(0, 0)$	m
Wave frequency	ω	27.83	$rad\ s^{-1}$
Wave number	k	6.283	$rad\ m^{-1}$
Interior ratio	f_d	0.2	-
Interior cell layers	N_e	120, 170, 250, 400, 550	-
Simulated time	t_{tot}	1.5	s
Envelope intro time	t_{intro}	0.113	s
Envelope full amplitude time	$t_{plateau}$	1.387	s
LSQ fit radial range	r_{start}, r_{end}	2.0, 3.0	m
LSQ fit time range	t_{start}, t_{end}	1.129, 1.355	s

Table 2.7: Case-specific parameters for the centred source reflection test

2.7.2. Off-Centre Sources

The off-centre source configuration is used to assess reflection behaviour as a function of incidence angle. Moving the source closer to the boundary increases the maximum attainable incidence angle, while also varying source-boundary distance. Each boundary location corresponds to a different incidence angle, but has a different distance from the source. This results in a combined effect of incidence angle dependent reflection and kr related reflection (2.60).

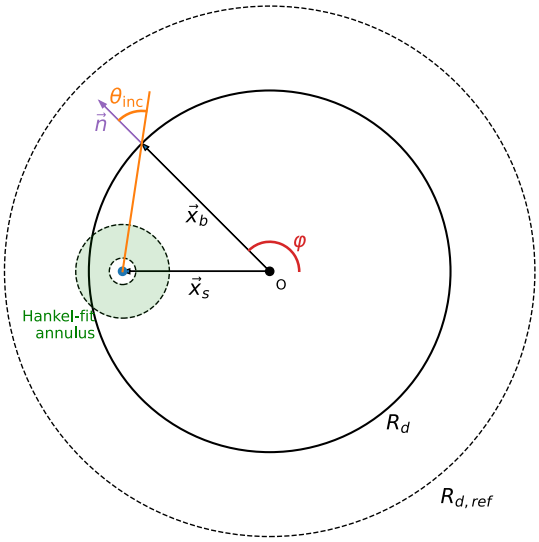

Figure 2.14: Visualisation of off-centre test setup

The configuration is visualised in Figure 2.14. At each boundary location $\vec{x}_b$ the incidence angle θ_{inc} depends on source location $\vec{x}_s$ and is defined by Equation 2.61.

$$\theta_{inc} = \arccos\left(\vec{n} \cdot \frac{(\vec{x}_b - \vec{x}_s)}{||\vec{x}_b - \vec{x}_s||}\right) \tag{2.61}$$

The test is performed for three different source locations and two wave numbers. For each case, a reference solution is set up on a computational grid obtained by extending the test domain grid, such that the interior remains identical. This ensures that solutions on the test domain can be compared without differences caused by numerical dispersion. Subtraction of the reference solution from the test solution then yields the reflected field. The reference domain is generated by adding cell layers based

on the average cell length normal to the boundary, with a stretch factor of 1.02 until a desired radius $R_{d,ref}$ is reached.

To assess the reflection at each boundary point and corresponding incidence angle, a reflected and local outgoing amplitude should be obtained. The outgoing amplitude is obtained by fitting a Hankel function ($H_0^{(1)}(k||\vec{x} - \vec{x}_s||)$) in the reference solution domain. Again, a LSQ fit is performed in clean temporal and spatial frame, such that the signal is free from both introduction effects and reflections. All numerical values in the interval (2.62-2.65) are taken into account in the LSQ fit. The spatial annulus is also visualised in Figure 2.14. The fit accuracy for A_{out} is evaluated using an R-squared value.

$$r_{start} = 0.05 R_{d,ref} \tag{2.62}$$

$$r_{end} = r_{start} + \frac{2\pi}{k} \tag{2.63}$$

$$t_{start} = t_{intro} + \frac{r_{end}}{c} \tag{2.64}$$

$$t_{end} = min\left[t_{intro} + t_{plateau},\ t_{start} + 2(R_{d,ref} - ||\vec{x}_s|| - r_{end})\right] \tag{2.65}$$

The maximum reflection amplitude is evaluated at each boundary location from the obtained reflected signal, sampled at a 50-time step interval within a safe analysis window (2.66, 2.67). The outgoing amplitude at each location is determined through $||A_{out} H_0^{(1)}(k||\vec{x}_b - \vec{x}_s||)||$. The simulation parameters for the tests are listed in Table 2.8 and 2.9.

$$t_{clean,start}(\vec{x}_b) = \frac{\|\vec{x}_b - \vec{x}_s\|}{c} + t_{intro} + \frac{T}{2} \tag{2.66}$$

$$t_{clean,end}(\vec{x}_b) = t_{clean,start} + 2T \tag{2.67}$$

Parameter	Symbol	Value Case I	Value Case II	Unit
Wave frequency	ω	50.0	18.5	$rad\ s^{-1}$
Wave number	k	11.28	4.18	$rad\ m^{-1}$
Interior ratio	f_d	0.5	0.5	-
Interior cell layers	N_e	500	500	-
Simulated time	t_{tot}	1.5	1.5	s
Envelope intro time	t_{intro}	0.0628	0.1698	s
Envelope outro time	t_{outro}	0.0628	0.1698	s
Envelope full amplitude time	$t_{plateau}$	0.377	1.019	s
Reference domain radius	$R_{d,ref}$	4.4	6.2	m

Table 2.8: Parameters for the off-centre source reflection tests for two cases

Parameter	Symbol	Subcase A	Subcase B	Subcase C	Unit
Source location	$\vec{x}_s$	(-2.441, 0)	(-2.581, 0)	(-2.720, 0)	m
Min. boundary distance	$\|\|\vec{x}_b - \vec{x}_s\|\|_{min}$	0.559	0.419	0.280	m
Max. incidence angle	$\theta_{inc,max}$	54.5	59.4	65.0	°

Table 2.9: Off-centre source configurations used for angle-dependent reflection subcases

Analytical expectation

For the Sommerfeld BC, an analytical result for the reflection coefficient can be obtained using a steady state solution. For this, the off-centre source is represented at each boundary point (R_d, φ) as an infinite modal sum of centred Hankel functions using Graf's addition theorem. The reflected signal is

represented as an infinite sum of Bessel functions of the first kind. More details for the representations are given in Appendix H.

$$\Phi_{out}(R_d, \varphi) = \frac{i}{4} \sum_{m=-\infty}^{\infty} J_m(k||\vec{x}_s||) H_m^{(1)}(kR_d) e^{im(\varphi - \angle(\vec{x}_s))} \tag{2.68}$$

$$\Phi_{refl}(R_d, \varphi) = \sum_{m=-\infty}^{\infty} b_m J_m(kR_d) e^{im(\varphi - \angle(\vec{x}_s))} \tag{2.69}$$

Enforcing the Sommerfeld BC gives coefficient b_m per reflected mode, which allows to compute the reflection coefficient analytically:

$$b_m = -\frac{i}{4} J_m(k||\vec{x}_s||) \frac{\frac{\partial H_m^{(1)}(kr)}{\partial(kr)} - iH_m^{(1)}(kr)}{\frac{\partial J_m(kr)}{\partial(kr)} - iJ_m(kr)} \tag{2.70}$$

The infinite sum is evaluated numerically at each boundary point, with a truncation at maximum mode m_{max} for which the sum converges. Convergence is verified by increasing the truncation limit until the relative change in both the incident and reflected field amplitudes falls below a prescribed tolerance of 1×10^{-10}. The average m_{max} over the boundary will be reported per case in the results.

2.7.3. Long-Crested Wave

A reflection test based on a Long-Crested Wave (LCW) introduced over the boundary is performed to verify the generating capability of the GABCs. LCWs can be used to assess reflection for waves that do not radially damp out like the point sources in the previous tests. Also, larger incidence angles are present at the boundary and effects from (near) grazing incidence can be evaluated.

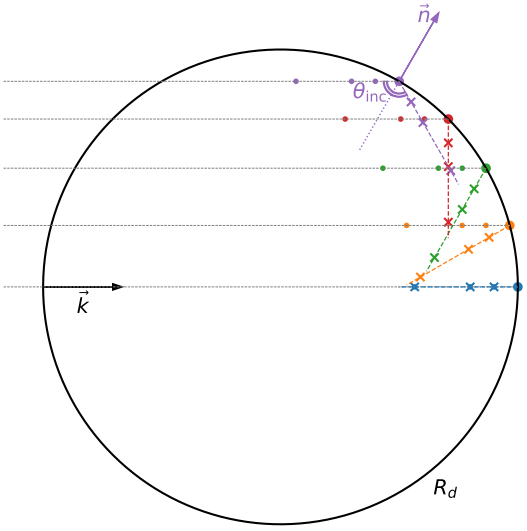

Figure 2.15: Visualisation of long-crested wave test setup, ·'s and ×'s represent wave probes for incoming and reflected wave components respectively.

The three GABC formulations will be tested with a similar setup. The wavelength is chosen such that the domain spans 4 wavelengths in diameter. The LCW is introduced by prescribing RHS for each GABC, computed analytically from a desired wave potential as in Equation 2.28. A spatial and temporal envelope will be applied to limit introduction effects. This envelope is applied after computing RHS, rather than applying the boundary operator to the product of the envelope and the desired potential.

This avoids cross terms from spatial and temporal derivatives in the boundary operator. The envelope is based on the envelope from Equation 2.12 and uses a delayed time coordinate χ for every boundary location $\vec{x}_b$:

$$\chi(\vec{x}_b, t) = t - \frac{\vec{x}_b \cdot \frac{\vec{k}}{||\vec{k}||} - R_d}{c} \tag{2.71}$$

$$Envelope(\vec{x}_b, t) = S\left(\frac{\chi(\vec{x}_b, t)}{t_{intro}}\right) \tag{2.72}$$

$$\vec{k} = k\begin{bmatrix}\cos\mu \\ \sin\mu\end{bmatrix} \tag{2.73}$$

$$\theta_{inc} = \theta_{refl} = \arccos\left(\vec{n} \cdot \frac{\vec{k}}{||\vec{k}||}\right) \tag{2.74}$$

Reflections are assessed using a LSQ fit, decomposing the signal into outgoing and reflected pressure components. For each incidence angle, three wave probes are positioned along the outgoing and reflected propagation line defined by Equation 2.74. The probes are placed at distances (s) $1/5\lambda$, $2/5\lambda$ and $13/15\,\lambda$ from the point of incidence at the boundary. The probes are spaced such that no full wavelength is spanned, and the probe spacings are no multiple of each other. The following equation describes the decomposition for which the LSQ fit is performed.

$$p(s,t) = A_{out}e^{i(\omega t + ks)} + A_{refl}e^{i(\omega t - ks)} \tag{2.75}$$

The setup is visualised in Figure 2.15. The signal at each probe is evaluated as soon as a fully developed reflected wave has reached the last probe (2.76). Incidence angles from 0 to 76 degrees are considered in the fit, as higher incidence angles will have probes outside of the domain. The simulation parameters are stated in Table 2.10.

$$t_{start}(\theta_{inc}) = t_{intro} + \frac{R_d + \vec{x}_b \cdot \frac{\vec{k}}{||\vec{k}||} + \frac{13}{15}\lambda}{c} \tag{2.76}$$

Parameter	Symbol	Value	Unit
Wave frequency	ω	18.5	$rad\ s^{-1}$
Wave number	k	4.177	$rad\ m^{-1}$
Wave length	λ	1.504	m
Wave direction	μ	0.0	^{o}
Wave potential amplitude	A	3.0	$m^2\ s^{-1}$
Interior ratio	f_d	0.5	-
Interior cell layers	N_e	500	-
Simulated time	t_{tot}	2.5	s
Envelope intro time	t_{intro}	0.3396	s

Table 2.10: Parameters for the Long-Crested Wave reflection test

3

Results

In the following sections, the results of the three reflection tests are given for the three different GABCs that were implemented. The performance of each can be explained by their assumptions and properties. The implemented GABCs are referred to as SFD, PEM and CEM. The results of the centred source test are given in section 3.1. The results of the off-centre source test are presented in section 3.2 and the LCW test will be presented in section 3.3.

3.1. Results Centred Source

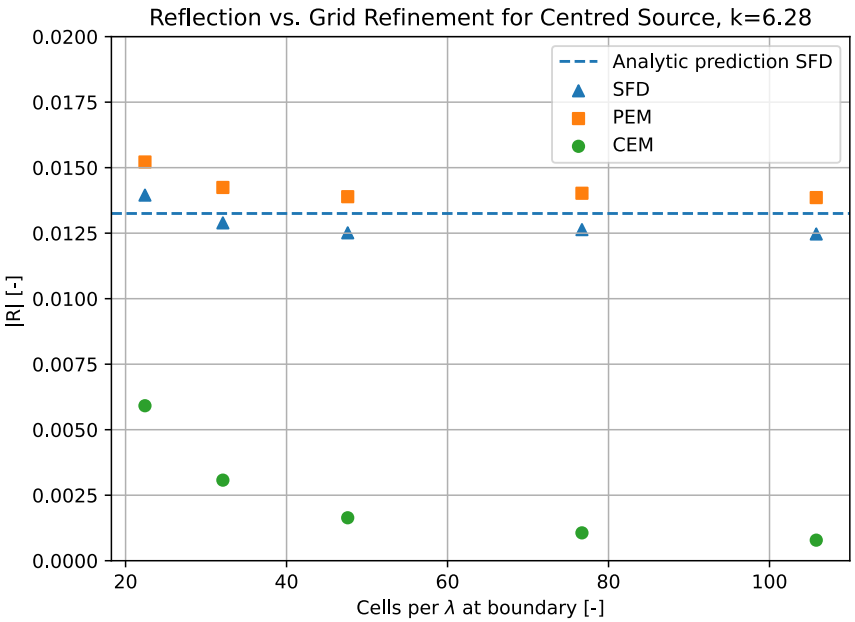

Figure 3.1: Reflection results for the two boundary conditions with different grid refinements

In Table 3.1, reflection coefficients and fit quality for various grid refinements for the centred test are reported. The performed LSQ fit produces an R-squared value indicating a high overall fit quality. The fit quality increases with grid refinement, as the numerical wave number k_{num} matches the analytical value more closely. Figure 3.1 visualises the reflection coefficients in Table 3.1 as a function of the grid refinement, quantified by the number of cell lengths per wavelength in the propagation direction. The reflection coefficients of both the SFD and the PEM BCs converge toward a level close to the analytic SFD prediction. The CEM converges to a lower value, as it takes part of the radial damping into account

Interior cell	SFD		PEM		CEM	
layers N_e	$\|\|R\|\|$	R-squared	$\|\|R\|\|$	R-squared	$\|\|R\|\|$	R-squared
120	0.01395	0.999875	0.01522	0.999875	0.00591	0.999874
170	0.01289	0.999911	0.01424	0.999911	0.00308	0.999911
250	0.01251	0.999919	0.01389	0.999919	0.00164	0.999918
400	0.01264	0.999935	0.01402	0.999935	0.00106	0.999935
550	0.01247	0.999947	0.01386	0.999947	0.00078	0.999947

Table 3.1: Mean reflection coefficients and mean fit accuracy over angular bins for the centred source test using three absorbing boundary conditions and five grid refinements.

that limits the performance of the SFD and PEM BCs in this centred situation. The PEM formulation has slightly higher reflection compared to the SFD case. The formulation is similar to a Sommerfeld BC because the tangential derivative in Equation 2.37 is equal to zero with normal incidence, however multiplied by a time derivative. The performance for this case is then slightly worse, because the SFD BC is solved for the same time step through substitution of the momentum equation. For the PEM BC, an explicit update is used. This causes a slight phase mismatch in the boundary condition that will increase reflection.

3.2. Results Off-Centre Sources

In Table 3.2, the fitted outgoing amplitudes are stated. The fitted outgoing amplitude increases as the source is placed closer to the boundary, due to cell size, and thus introduced energy, being larger near the boundary. The fit accuracy is almost indifferent over the cases, while slightly higher for case II with higher grid resolution compared to wavelength. The average maximum mode for convergence of the analytical modal sum is also stated in the table. This maximum mode increases as the source moves more off-centre and is higher for case I with shorter wavelength, consistent with expectation as these produce stronger angular variation.

Case : k		$\|\|\vec{x}_b - \vec{x}_s\|\|_{min}$	$\|\|A_{\text{out}}\|\|$	R-squared	$m_{max,avg}$
	A	0.559	4.7015	0.999907	107
I : 11.28	B	0.419	4.9225	0.999906	142
	C	0.280	5.1439	0.999908	200
	A	0.559	1.7395	0.999920	98
II : 4.18	B	0.419	1.8214	0.999925	131
	C	0.280	1.9033	0.999926	189

Table 3.2: Outgoing Hankel amplitude and fit accuracy determined from the reference solution for different off-centre (sub)cases and average maximum angular mode m for the analytical result.

The reflection coefficients for case I and II with respect to incidence angle are presented in Figure 3.2 and 3.3 respectively. In general, the closer a source is moved towards the boundary, and the longer the wave is with respect to this distance, the higher the reflection. This corresponds to high reflection for low kr values which has a higher analytical reflection prediction by Equation 2.60.

For the SFD BC, the numerical results follow the same trend as the analytical results. For lower incidence angles, a fairly constant reflection coefficient plateau is present. With reduced kr this reflection plateau becomes more dominant. As the incidence angle increases, kr increases. This results in a slight decrease of reflection before the incidence angle mismatch becomes dominant for higher incidence angles.

For the PEM BC, the kr plateau at lower incidence angles is not present. This is expected as the off-centre source location introduces tangential variation along the boundary, which the second-order tangential derivative in the operator can account for. As incidence angles increase, the tangential variation becomes stronger and reflections increase, however less quickly than for the SFD BC. This confirms theoretical expectation related to angular reflection dependence and higher-order ABC theory.

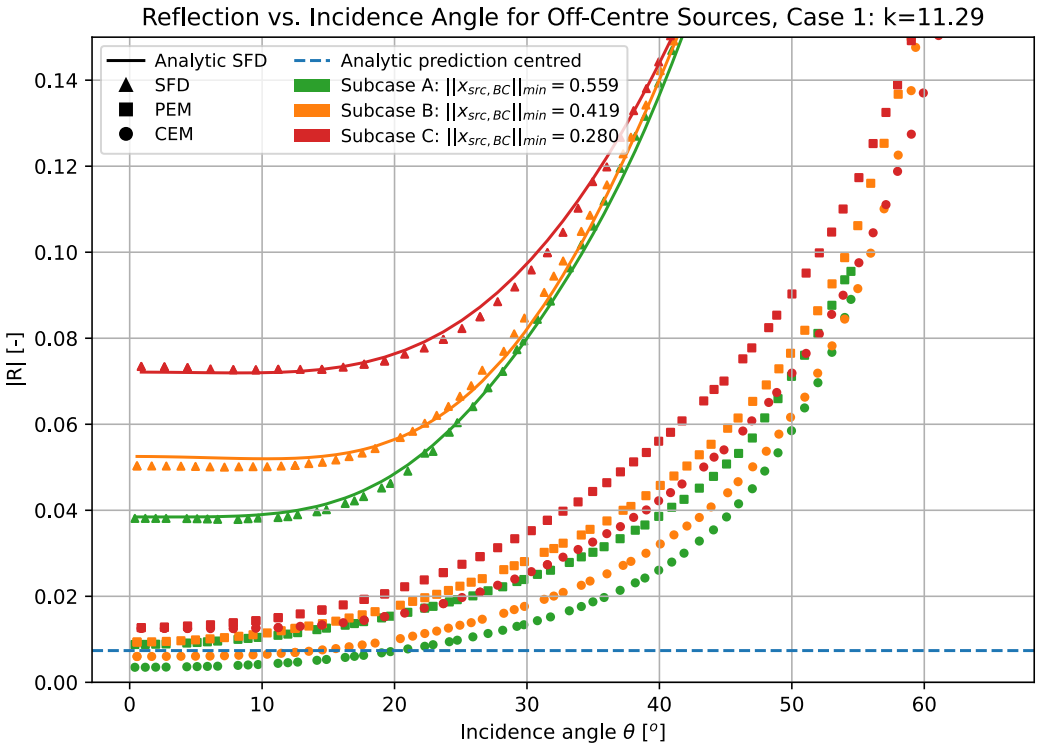

Figure 3.2: Case 1: Reflection coefficient per incidence angle for three different boundary conditions with sources placed off-centre with 3 different boundary offsets. Short wave with k=11.29

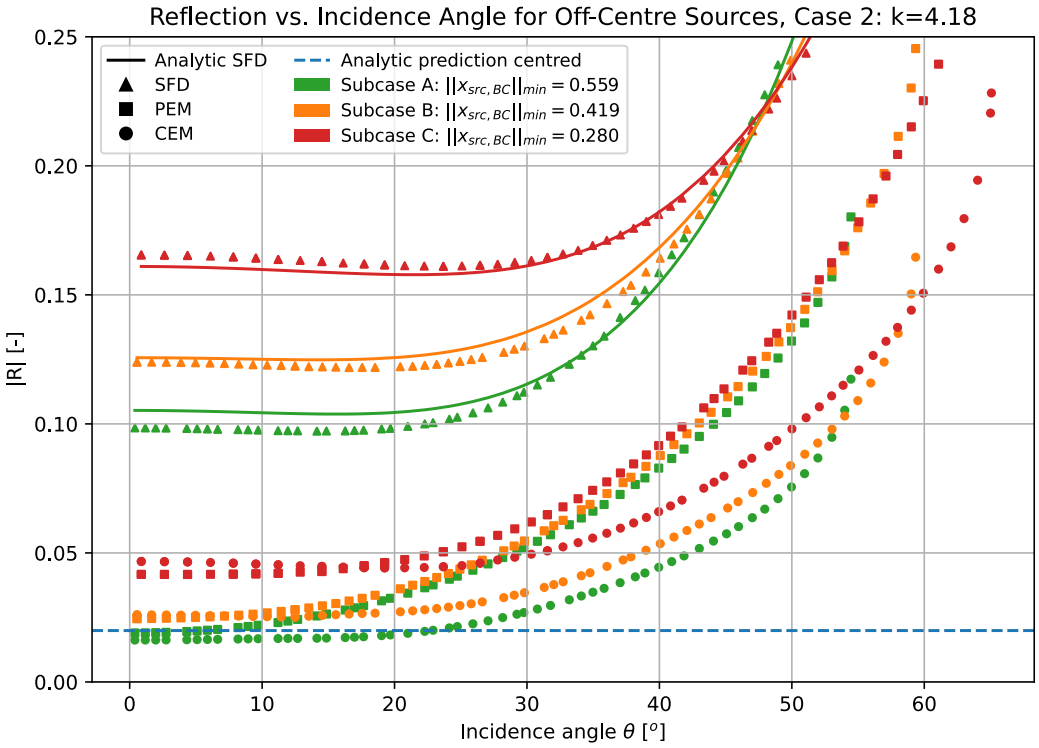

Figure 3.3: Case 2: Reflection coefficient per incidence angle for three different boundary conditions with sources placed off-centre with 3 different boundary offsets. Long wave with k=4.18

The CEM BC generally improves the performance further through inclusion of radial damping terms, related to kr. Figure 3.2 shows a lower reflection at normal incidence and a similar trend with increasing incidence angle compared to the PEM BC. Figure 3.3 shows a slightly inferior reflection at normal incidence for subcase B and C, corresponding to very low kr values. However, as the angle increases, and thereby also kr, the reflection increases less quickly compared to the PEM BC. A general trend can be seen over the (sub)cases that the CEM BC improves performance if kr is sufficiently high.

3.3. Results Long-Crested Wave

The foreseen LSQ decomposition of outgoing and reflected components described in subsection 2.7.3 did not yield consistent reflection coefficients. Reflection coefficients above 1 were obtained. The origin of this behaviour could not be identified within the scope of this work. Quantitive reflection curves can therefore not be reported. Instead, the results of the different GABC formulations will be interpreted qualitatively based on pressure field visualisations. In Figure 3.4 the generating capability of the different formulations is shown. The figure shows different mean pressure levels for the introduced wave. The SFD formulation yields zero mean, while the PEM and CEM formulations yield mean offsets.

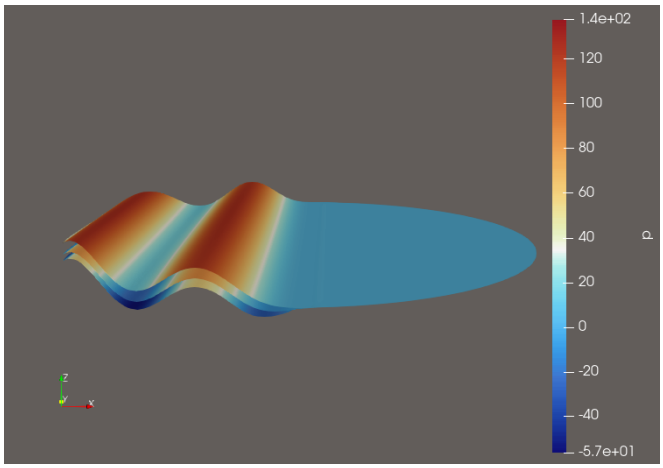

Figure 3.4: Results for three GABC formulations at t = 0.81 s. The top surface corresponds to CEM, the middle surface to PEM, the bottom surface to SFD.

The results for each GABC formulation are displayed at two time instants. The displayed images contain colour scales. The minimum and maximum of the scales are based on the minimum and maximum values of the introduced wave for the respective simulation at t=1.0, before reflection occurs.

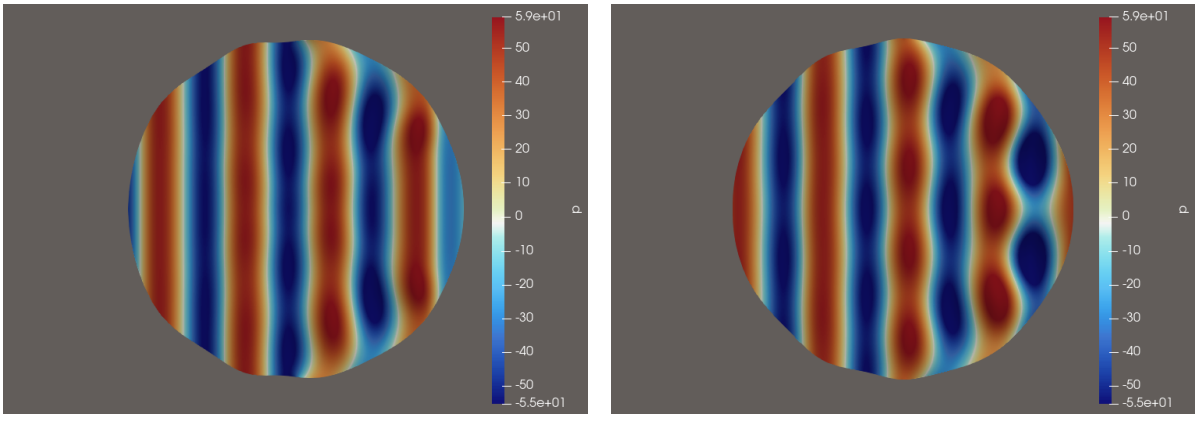

(a) SFD at t = 1.50 s

(b) SFD at t = 2.40 s

Figure 3.5: Results of the SFD formulation for two time instants

For the SFD formulation, the results are displayed in Figure 3.5. Figure 3.5a shows a combined incident

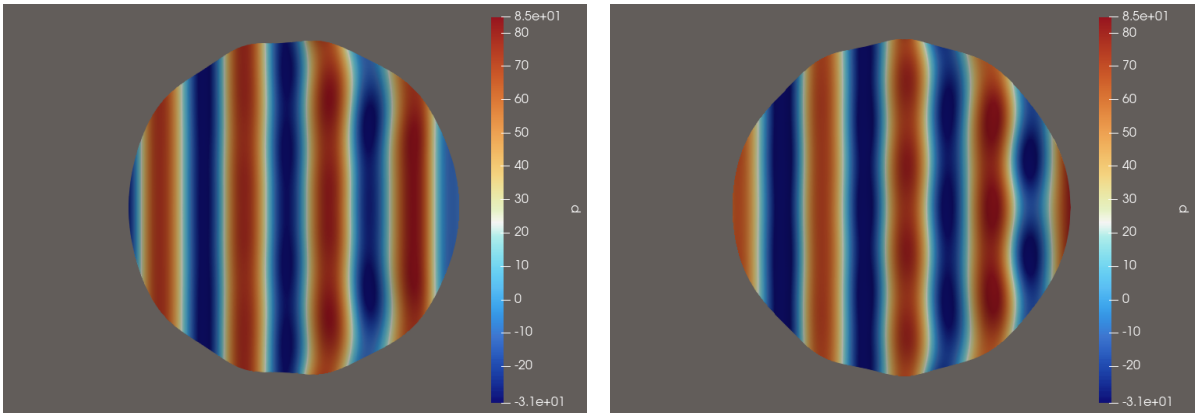

(a) PEM at t = 1.50 s

(b) PEM at t = 2.40 s

Figure 3.6: Results of the PEM formulation for two time instants

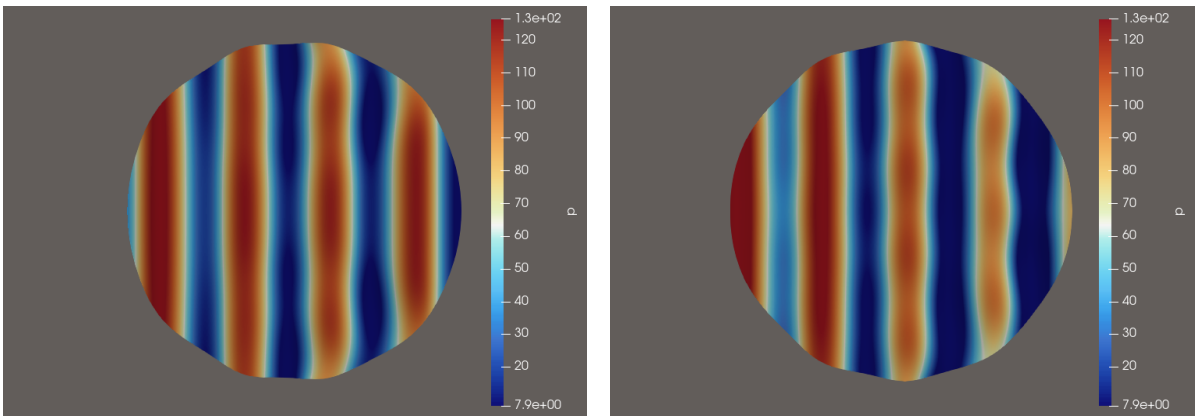

(a) CEM at t = 1.50 s

(b) CEM at t = 2.40 s

Figure 3.7: Results of the CEM formulation for two time instants

and reflected field with a clearly visible interference pattern. This interference is even more pronounced at a later time instant in Figure 3.5b. This indicates significant reflection for the SFD formulation.

The same interference pattern can be recognised in Figure 3.6, however visibly less pronounced. This indicates less reflection for the PEM compared to the SFD formulation. This is consistent with theoretical expectation. Secondly, a mean positive offset can be noticed in the colour scale. This indicates that the introduced wave does not oscillate around zero mean pressure.

Also in Figure 3.7 the interference pattern can be recognised. Also these results display a mean positive offset that is more pronounced than for the PEM formulation. Next to the mean offset, a spatial gradient in the mean pressure is present. In Figure 3.7b this is clearly visible, with higher pressure values at the left of the image compared to the right. This gradient complicates the visual assessment of the reflected pattern. Therefore, a clear qualitative ranking between the PEM and CEM formulation cannot be obtained. However, the absorbing properties of these two are clearly superior compared to the SFD formulation.

Two mechanisms might contribute to the mean offset and spatial gradient observed in the higher-order GABC formulations. First, the temporal discretisation for CEM and PEM is explicit whereas the SFD formulation is solved for the same time level. Second, the envelope with which the full amplitude wave is introduced is applied afterwards, instead of taking product rule contributions into account. A pattern is observed in which formulations involving increasing-order derivatives exhibit increasingly pronounced artefacts. Since both the explicit temporal treatment and the omission of product rule terms are directly related to the order of derivatives, this suggests a possible link between formulation order and the observed artefacts.

4

Conclusion

This work investigates the application and evaluation of higher-order local Generating Absorbing Boundary Conditions (GABCs) for domains with rectangular interiors while circumventing corner compatibility conditions through the use of curvilinear coordinates. To enable this, a well-structured numerical methodology was developed, implemented and verified for linearised shallow water equations. In this methodology, curvilinear coordinates are used to apply a circular boundary to a rectangular interior. The resulting curvilinear grid is mapped to a computational plus-shaped grid. The approach employs a staggered curvilinear Finite Volume (FV) discretisation on the plus-shaped grid, with coupling across the interior slits to form a continuous domain. A verification against a Cartesian reference solution shows high accuracy, through relative errors of 0.014% and maximum errors of the same order as discretisation-inherent numerical artefacts. Although this verification was limited to a single centred wave configuration, these results confirm that shallow water waves can be simulated reliably on a grid combining a circular boundary with a rectangular interior, thereby answering the first research subquestion and providing the foundation for application and evaluation of higher-order GABCs.

To enable pressure based boundary conditions using ghost cells, a pressure interpolation was tested on curved boundaries. For increasing curvature on the boundary, the pressure interpolation showed an increasing error. The error of the interpolation however also showed second-order convergence when the grid was refined. These results are consistent with theoretical expectation.

With the interior and boundary machinery verified, three types of GABCs were discretised in generalised curvilinear coordinates. A first-order GABC based on a Sommerfeld (SFD) operator, and two second-order GABCs based on Planar Engquist-Majda (PEM) and Circular Engquist-Majda (CEM) operators. Three tests were performed to assess their performance. A centred source test assessing normal incidence absorption, an off-centre source test for multidirectional incidence, and a test for generating Long-Crested Waves (LCWs) and subsequent absorbing performance.

In the centred source test configuration, results of SFD and PEM followed the analytic prediction of the reflection coefficient. The SFD results fell slightly below the analytical value, the PEM results slightly above, consistent with the applied time discretisation and theoretical expectation. CEM clearly improved results as it accounts for radial amplitude decay effects, which are dependent on source-boundary distance (kr). The test was performed for fixed time step and wave input parameters for several grid refinements. Spatial convergence was observed for coarser grids and a converged result was found for the finer grids. The time step was not varied during the convergence analysis. Performing the analysis for a constant Courant number would show overall convergence behaviour.

Off-centred source test configurations with two different wavelengths showed that reflection behaviour is governed by a combined dependence on incidence angle and source–boundary distance (kr). Moving the source closer to the boundary or increasing the wavelength both reduce kr, resulting in systematically higher reflection levels for all GABCs. Each GABC captures these dependencies differently, depending on whether kr dependent behaviour and angular dependence are incorporated in the formulation.

For the SFD formulation, an analytical result was computed that follows the same trend as the numerical results, providing confidence in the numerical implementation. The SFD formulation does not account for radial decay, leading to reflection plateaus near normal incidence at low kr. Inclusion of a second-order tangential derivative in PEM clearly improves absorption. Both tangential variation over the boundary due to radial amplitude decay effects at normal incidence, as tangential variation due to incidence angle, are captured more effectively by the PEM formulation. The CEM operator, designed to incorporate explicit kr dependence, provides superior absorption at sufficiently large kr, outperforming PEM as both kr and incidence angle increase. These results establish a clear hierarchy of absorbing performance consistent with higher-order Absorbing Boundary Condition (ABC) theory.

These results address two research sub-questions. They demonstrate that a Sommerfeld ABC can be discretised on a circular boundary in generalised curvilinear coordinates. Second, they confirm that higher-order ABCs can be formulated as well and improve absorption for a range of incidence angles. The analysis also reveals the influence of parameter kr on circular boundaries. For both the SFD and PEM formulation, this limits performance. The CEM formulation that was introduced generally improves this, especially for higher kr values.

For the LCW case, quantitative reflection coefficients could not be reliably extracted with the proposed method. Therefore, the analysis was limited to qualitative interpretation of pressure field visualisations. Both the PEM and CEM formulations exhibited a visually reduced interference pattern, confirming expected improved performance compared to the SFD formulation. The PEM introduced a mean pressure offset upon wave introduction. The CEM also introduced a mean offset and a spatial gradient upon introduction. This gradient complicates visual comparison with the PEM case, preventing a definitive qualitative ranking between these two formulations in this test case.

These results address the remaining research sub-questions. It is indeed possible to introduce waves on a circular boundary using a Sommerfeld ABC, yielding a first-order GABC. Furthermore, wave introduction using higher-order formulations is feasible. However, the higher-order operators exhibit numerical introduction artefacts that require further refinement before fully quantitative assessment of their generating-absorbing performance is possible.

The main research question of this work can be answered to substantial extent. The results of this work demonstrate that higher-order local Generating Absorbing Boundary Conditions can be applied to domains with rectangular interiors while circumventing corner compatibility conditions by mapping to a circular boundary using curvilinear coordinates. Results confirm that higher-order formulations consistently improve absorption compared to first-order formulations. Also generative capability was demonstrated, however with numerical artefacts present for higher-order formulations. At the same time, the results highlight that absorption of waves on circular boundaries is inherently limited for radiating sources. For LCWs, a quantitative result of planar wave absorption on circular boundaries has not yet been established. Furthermore, simultaneous generation and absorption performance has not yet been assessed in a dedicated quantitative test.

Overall, this work establishes the feasibility and consistent relative improvement of higher-order GABCs for domains with rectangular interiors and circular boundaries, while identifying the remaining steps required for full quantitative performance characterisation.

Future work should first investigate the origin of the numerical introduction artefacts observed in the higher-order formulations. Investigation should include, but not be limited to two effects: First, the role of the explicit temporal discretisation for the PEM and CEM should be assessed. Second, the effect of omitting product rule terms by applying an introduction envelope afterwards should be studied. Once robust wave introduction is ensured, tests capable of extracting reflection coefficients for LCWs should be performed for a quantitative comparison between formulations. This way, it can be assessed whether the kr-dependence observed for radiating sources also governs absorption for LCWs introduced on circular boundaries. This result is relevant to determine the required structure of a high-order ABC operator on a circular boundary, to accurately absorb the combination of waves encountered in wave simulations for offshore structures. Reflections attainable with this formulation can be benchmarked with simulations on Cartesian domains that do contain corner induced reflections. Finally, a dedicated test quantifying simultaneous generating and absorbing performance should provide conclusive answers on GABC performance.

A

Literature Review Inconvenient Draught

In this appendix, a review will be given concerning the relevant literature available on motion simulation of Semi-Submersible Crane Vessels (SSCVs) at Inconvenient Draught. First, an introduction to the name ”Inconvenient Draught” will be given in section A.1. Next, relevant physics for the problem will be highlighted. In section A.3, relevant literature on the problem with linear diffraction theory will be discussed. Non-linear potential flow methods will be discussed in section A.4, followed by CFD approaches in section A.5. In the end, a summary concerning requirements for a reasonable approach based on previous literature is given.

A.1. Inconvenient Draught

When SSCVs operate at shallow draught, with a small water column on top of its floaters, research and experience have shown that linear diffraction theory is unable to predict motions without being conservative [33] [34]. Linear diffraction theory is a simple, quick and powerful tool, often applicable beyond initial assumptions, in many situations. This makes linear diffraction theory a very convenient tool. Beyond linear diffraction theory, available approaches that are able to predict or model the motions, require extremely high computational resources. Therefore, the aforementioned draught is often referred to as ”Inconvenient Draught” in literature and industry. In the following sections, available methods will be analysed based on literature and their potential or discrepancies will be discussed.

A.2. Relevant Physics

During operation at inconvenient draught, the SSCV is subject to irregular waves. Due to these waves, the vessel experiences pressure fluctuations on its hull, which cause vessel motions. During the motions of the vessel, the vessel’s motions are damped by the waves it creates and radiates away from the vessel. These radiated waves are a form of inviscid damping.

Other than inviscid damping, the vessel also has some form of viscid damping. This is caused by skin friction and shedded vortices of the corners of the SSCV’s floater. However, this viscid damping is comparable for deeper draughts. As linear diffraction theory is able to correctly predict at deeper draughts [33], this phenomenon is less important for the motions of the vessel. Only for heavy roll or pitch motions, this generally becomes important.

Also, the vessel motions may cause the top of the floater approach or rise above the free surface. This can cause parts of the floater to have an infinitesimal amount or no water on top of it, a phenomenon commonly referred to as ”wetting and drying”. Moreover, close proximity to the free surface can cause incoming waves to steepen. This is commonly referred to as ”shoaling”, and can cause wave breaking. These phenomena characterise a violent free surface, which is non-linear.

One of the features of the inconvenient draught problem is thus a violent free surface, together with a varying waterplane area. This varying waterplane area is quite relevant for the motion of the vessel, and causes non-linear effects as well. The vertical position of the SSCV’s floater is quite relevant for

how incoming waves will interact with it. A difference in vertical position could make a difference in the portion of a wave rolling over the floater and the part being reflected off the side of the floater. One of the characteristics of a linear process is the concept of linear superposition, meaning that motions caused by each frequency component can be summed (superposed) to obtain the total vessel motion. However, if a certain frequency component causes upward vessel motion, this will influence how the other frequency components will interact with the vessel as well. This illustrates the non-linearity of the situation. In order to capture the vessel behaviour accurately, a sufficient time domain analysis is necessary in order to capture the full motion behaviour of the vessel. Depending on the simulation intensity, this can require significant computational resources.

A.3. Linear Diffraction Theory

Given that linear diffraction theory is usually versatile and convenient, it is not surprising that several attempts have been made to model the inconvenient draught problem with alterations of the method. Also, it has been investigated why the method is not able to capture the motion behaviour properly.

Based on experiments, Van der Kroft [33] has shown discrepancies of linear diffraction theory. In these tests, a 2D model is subjected to regular waves of different frequencies, and compared to predictions by linear diffraction theory. It is shown that especially in frequencies where linear diffraction theory predicts zero (inviscid) damping, discrepancies with the experiments occur. These discrepancies occur both in the wave load as well as the damping. However, radiated waves were clearly visible in the experiments at these frequencies, which indicate an inability of linear diffraction theory to model this damping. Also, the incoming wave loads were not predicted correctly in these cases. What Van der Kroft [33] noticed in these frequencies as well, is that the measured surface elevation on top of and besides the floater contained higher harmonics. This could be seen in increased peaks on top of the floater and different frequencies showing up in the oscillating signal on the sides of the floater. This exchange of energy between frequencies is clearly non-linear behaviour and requires a method that can handle non-linearities.

Because of the lack of damping predicted by linear diffraction theory at certain frequencies, adding artificial damping could possibly improve the results. This was attempted using damping lids by Van Winsen, Bokhorst, and Huijsmans [34]. This approach resulted in a better approximation at the frequencies with large discrepancy. However, huge values are necessary for the damping lids to properly approximate the RAO at these certain frequencies. This causes large discrepancies at frequencies that were predicted better without damping lids. This indicates that the problem can behave differently over different frequencies, reconfirming non-linearity. This means that a proper analysis over the full frequency spectrum is necessary to correctly predict motions at inconvenient draught.

A.4. Non-linear Potential Flow

One might think that non-linear potential flow methods are able to capture the non-linear physics of the problem. Generally speaking, this would pose a good solution to general problems in which viscous effects are not primarily relevant. Especially in non-linear wave interaction problems, this could be a good approach. However, for the Inconvenient Draught case, a modelling approach is necessary in which a violent free surface in close proximity to a structure can be modelled.

The violent free surface contains breaking waves, which mean an overturning free surface. Non-linear potential flow methods are unable to predict this in proximity to structures, as Fitzgerald [12] confirms. This limitation exists for non-linear potential flow methods, because wave overturning leads to coinciding or overlapping panels. This triggers numerical instabilities which causes methods in literature to reside to other methods. For example, in a study on modelling wave breaking using non-linear potential flow Simon et al. [31] add dissipation as soon as a threshold wave slope is reached, modelling only the dissipative effects of wave breaking, and preventing wave overturning.

This numerical instability is also relevant when a free-surface panel and a boundary panel on a structure coincide. This commonly happens during wetting and drying of the floater, posing a significant limitation for this modelling technique. During the wetting and drying, infinitesimally small water columns can be present on top of the floater of the semi-submersible. In a study on wave propagation along the

Norwegian coast, Wang et al. [35] confirm that this infinitesimal water column can cause numerical instabilities. As a result, they modified their modelling approach by using coastal relaxation zones in regions where wetting and drying occurs. These zones are chosen such that these coastal zones are minimally influencing the larger scale flow field. However, the specific flow field in the wetting and drying zones are of specific interest to the inconvenient draught problem. The numerical instability associated with infinitesimal water columns makes modelling motions of SSCVs at inconvenient draughts with non-linear potential flow methods challenging. This means that CFD approaches are most promising to accurately predict motions at inconvenient draught, as will be explained in the next chapter.

A.5. CFD Approaches

All approaches in this chapter are in essence computational fluid dynamics (CFD) methods. However, the methods indicated in this section regard what is usually implied with the term CFD; 3D discretised domains in which equations are solved by calculating fluxes or differences between neighbouring cells. Two studies will be highlighted that performed CFD calculations on SSCVs at inconvenient draught.

In a study of the motion response of the SSCV Thialf at deep and inconvenient draught, Ottens and Pistidda [30] compare CFD results with model tests and linear diffraction theory. The model tests were performed at a different loading condition than the CFD simulation. Additionally, the research indicates that computational resources were limited. This resulted in limited simulation time as well as limited cases that were studied. For the CFD setup, it was mentioned that wave reflections from the boundary have to be limited. To accomplish this, an Euler Overlay Method was used to force the solution to a desired far-field solution (of only the incoming waves) in the outer region of the domain. The forcing parameter was first applied using a recommended value from literature, however this was experienced too low to prevent wave reflections and was multiplied by a factor of 10. For deep draughts, the authors concluded CFD results align with model tests and linear diffraction theory. However, at inconvenient draughts, CFD results differed from linear diffraction theory but matched more closely with model test outcomes. The research concludes that the motion response of an SSCV clearly shows a non-linear character. The authors also recommend that more wave height-draught combinations should be tested to further investigate whether CFD can be used to model SSCVs at inconvenient draught.

In a study performed by De Bruijn et al. [7], model tests of a semi-submersible at deep and inconvenient draught are compared to a CFD simulation using an improved Volume of Fluid (iVOF) method. The results are also compared to those obtained from linear diffraction theory. The study considers both captive and moving conditions for the semi-submersible. For the captive test, a generating-absorbing boundary condition (GABC) was used, which allowed simulating the entire domain for a duration of 4 wave periods. De Bruijn et al. state that this was sufficient for obtaining wave forces and internal loads of the semi-submersible. For longer simulation times, reflections from boundaries would have become too dominant. For the moving case, however, no absorbing boundary conditions could be implemented, which necessitated a numerical beach. Consequently, only half of the domain could be simulated because of the additional computational resources required. The authors state that for the captive tests, CFD results were in good agreement with the model tests. Linear diffraction results differ for the inconvenient draught case, especially with higher wave amplitudes. For the moving tests, multiple limitations influence the accuracy of the tests as the authors mention. First, only half the domain was simulated, using a no-slip boundary condition instead of a symmetry boundary condition. Secondly, the motions of the semi-submersible were prescribed with linear diffraction theory instead of solved in the CFD simulation. For the free floating case, the wave loads could not be captured by the model tests. Comparing the motions would not make sense as these are prescribed by linear diffraction theory. The authors do state however that the internal loads predicted by CFD matched those based on wave loads from linear diffraction theory.

These two studies demonstrate that CFD results generally align more closely with experimental model tests than with linear potential flow theory. However, neither study provides conclusive results of the full motion behaviour due to computational limitations. This suggests that CFD holds potential for accurately predicting the motions of SSCVs at inconvenient draughts, given that computational efficiency can be improved. Both studies identify wave reflections at domain boundaries as a key challenge, each addressing this issue through different mitigation strategies. Preventing wave reflections is a

major driver of computational demand, making it a limiting factor for CFD approaches.

A.6. Requirements Method

All together, literature and the nature of the problem point toward a modelling approach in which several factors are of high importance:

- First of all, the non-linear character of the problem must be captured in the approach.
- Next to that, the approach must be able to capture a violent free surface, consisting of wetting and drying effects as well as breaking waves.
- Computational resources, despite being ever increasing, pose limits to the approach.
- To get a good indication of the non-linear behaviour of the vessel, a sufficient number of wave height-period combinations should be simulated. This again indicates significant computational resources.
- To accurately capture the vessel's non-linear behaviour, simulations must cover a significant amount wave periods. This indicates significant computational resources as well as potentially problematic wave reflections on restricted domains.

The combination of modelling non-linear effects and violent free-surface effects can only be captured by CFD approaches with accurate free-surface tracking. Two well-known options are available for the free-surface tracking; Level-Set (LS) and Volume-of-Fluid (VOF) methods. LS is not strictly mass conserving however, but VOF methods are available which are strictly mass conserving, also in complex free-surface interactions [27]. The computational resources that these CFD methods require are high, and as stated earlier, wave reflections within the computational domain pose limits to this approach. Therefore, efficient truncation of the computational domain will be necessary to accurately determine the motions of SSCVs at inconvenient draught. Literature on computational domain truncation will be given in the main body of this thesis.

B

Curvilinear Finite Volume Discretisation

In this appendix, the linearised shallow water equations with constant bathymetry h will be discretised for a curvilinear grid that does not change in time. The variable orientation is staggered; pressures are defined in cell centers, velocities on cell faces. The equations with unit density are repeated below. In Equation B.2 the right hand side introduces a bottom friction which will be set to zero for most of the applications in this work.

$$\frac{1}{G}\frac{\partial p}{\partial t} + h(\vec{\nabla} \cdot \vec{u}) = 0 \tag{B.1}$$

$$\frac{\partial \vec{u}}{\partial t} + (\vec{\nabla} p) = -C_w \vec{u} \tag{B.2}$$

A FV discretisation will be performed following the work of Sparidans [32]. This process is described in the following sections. Important assumptions up front are that the grid is stationary and does not change in time. Other than that, the grid is 2 dimensional which means cell volumes are cell areas multiplied by unit height. In curvilinear coordinates, it is common to use Einstein notation. Indices α, β, γ and δ are used for this. A superscript indicates a contravariant quantity and a subscript a covariant quantity. Also notation of staggered variable location are used, indicated by $|_{i,j}$. Offsets of $\pm\frac{1}{2}$ indicate offsets of half a cell.

B.1. Continuity Equation

For discretising Equation B.1, the physical control volume (CV) Ω, bounded by $\mathcal{S}$ is taken. $\mathcal{S}$ is composed by the combination of a north, east, south and west boundary.

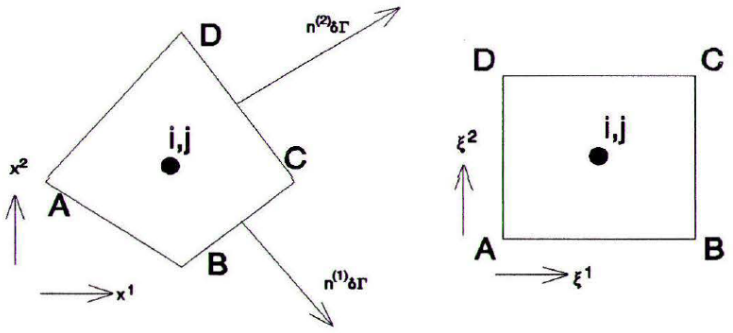

Figure B.1: Control volume in curvilinear and computational space [32]. Γ in the figure will be indicated as $\mathcal{S}$ in this work.

$$\frac{1}{G}\frac{\partial p}{\partial t} + h(\vec{\nabla}\cdot\vec{u}) = 0 \tag{B.3}$$

$$\int_\Omega \left(\frac{1}{G}\frac{\partial p}{\partial t} + h(\vec{\nabla}\cdot\vec{u})\right) d\Omega = 0 \tag{B.4}$$

$$\frac{1}{G}\int_\Omega \frac{\partial p}{\partial t} d\Omega + h\int_\Omega (\vec{\nabla}\cdot\vec{u}) d\Omega = 0 \tag{B.5}$$

Applying the divergence theorem, the following expression can be derived:

$$\frac{1}{G}\int_\Omega \frac{\partial p}{\partial t} d\Omega + h\oint_S \vec{u}\cdot\vec{n} dS = 0 \tag{B.6}$$

The normal vectors to the faces can be used, which are contravariant tensors.

$$\vec{n}^{(1)}\delta S = \begin{pmatrix} \delta x^2 \\ -\delta x^1 \end{pmatrix} \tag{B.7}$$

$$\vec{n}^{(2)}\delta S = \begin{pmatrix} -\delta x^2 \\ \delta x^1 \end{pmatrix} \tag{B.8}$$

For these expressions, it can be shown that the following holds, in which $g*$ is the determinant of the covariant metric tensor, and $\vec{a}^{(\alpha)}$ is the contravariant base vector of coordinate ξ^α.

$$\vec{n}^{(1)}\delta S = \sqrt{g*}\,\vec{a}^{(1)}\delta\xi^2 \tag{B.9}$$

$$\vec{n}^{(2)}\delta S = \sqrt{g*}\,\vec{a}^{(2)}\delta\xi^1 \tag{B.10}$$

$$\tag{B.11}$$

Approximating the surface integral using these relations gives:

$$\oint_S \vec{u}\cdot\vec{n} dS \approx (\vec{u}\cdot\sqrt{g*}(-\vec{a}^{(1)})\delta\xi^2)_{west} + (\vec{u}\cdot\sqrt{g*}\,\vec{a}^{(1)}\delta\xi^2)_{east} + (\vec{u}\cdot\sqrt{g*}(-\vec{a}^{(2)})\delta\xi^1)_{south} + (\vec{u}\cdot\sqrt{g*}\,\vec{a}^{(2)}\delta\xi^1)_{north} \tag{B.12}$$

Using the fact that $\vec{u}$ can be expressed using contravariant components:

$$\vec{u} = U^1\vec{a}_{(1)} + U^2\vec{a}_{(2)} \tag{B.13}$$

and

$$\vec{a}_{(\alpha)}\cdot\vec{a}^{(\beta)} = \delta^\beta_\alpha \tag{B.14}$$

where δ^β_α is the Kronecker delta, which is 1 if $\alpha = \beta$ and 0 otherwise. It can be shown that the following holds:

$$\oint_S \vec{u}\cdot\vec{n} dS \approx -(U^1\sqrt{g*}\,\delta\xi^2)_{west} + (U^1\sqrt{g*}\,\delta\xi^2)_{east} - (U^2\sqrt{g*}\,\delta\xi^1)_{south} + (U^2\sqrt{g*}\,\delta\xi^1)_{north} \tag{B.15}$$

In terms of i and j locations, and defining $V^\alpha = U^\alpha\sqrt{g*}$:

$$\oint_S \vec{u}\cdot\vec{n} dS \approx -(V^1\,\delta\xi^2)|_{i-\frac{1}{2},j} + (V^1\,\delta\xi^2)|_{i+\frac{1}{2},j} - (V^2\,\delta\xi^1)|_{i,j-\frac{1}{2}} + (V^2\,\delta\xi^1)|_{i,j+\frac{1}{2}} \tag{B.16}$$

$$\int_\Omega \frac{\partial p}{\partial t} d\Omega \approx \frac{\partial p}{\partial t}|_{i,j} \sqrt{g*}|_{i,j}\, d\xi^1 d\xi^2 \tag{B.17}$$

Substituting both in Equation B.6, this results in the semi discrete equation:

$$\frac{1}{G}\frac{\partial p}{\partial t}|_{i,j} \sqrt{g*}|_{i,j}\, d\xi^1 d\xi^2 - h(V^1\,\delta\xi^2)|_{i-\frac{1}{2},j} + h(V^1\,\delta\xi^2)|_{i+\frac{1}{2},j} - h(V^2\,\delta\xi^1)|_{i,j-\frac{1}{2}} + h(V^2\,\delta\xi^1)|_{i,j+\frac{1}{2}} = 0 \tag{B.18}$$

as the computational grid is chosen equidistant with $\delta\xi^1 = \delta\xi^2 = 1$:

$$(\frac{\partial p}{\partial t}\sqrt{g*})|_{i,j} - GhV^1|_{i-\frac{1}{2},j} + GhV^1|_{i+\frac{1}{2},j} - GhV^2|_{i,j-\frac{1}{2}} + GhV^2|_{i,j+\frac{1}{2}} = 0 \tag{B.19}$$

So as a result:

$$\frac{\partial p}{\partial t}|_{i,j} = \frac{Gh}{\sqrt{g*}|_{i,j}}\left(V^1|_{i-\frac{1}{2},j} - V^1|_{i+\frac{1}{2},j} + V^2|_{i,j-\frac{1}{2}} - V^2|_{i,j+\frac{1}{2}}\right) \tag{B.20}$$

B.2. Momentum Equation

$$\frac{\partial \vec{u}}{\partial t} + (\vec{\nabla} p) = -C_w \vec{u} \tag{B.21}$$

In tensor notation, following the tensor formulation of the Navier Stokes equations in Kan et al. [24]:

$$\partial_t U^\alpha + (g^{\alpha\beta} p)_{,\beta} = -C_w U^\alpha \tag{B.22}$$

The covariant derivative: $(g^{\alpha\beta} p)_{,\beta}$ is a covariant derivative of a contravariant second-order tensor: $T^{\alpha\beta}_{,\beta}$ and can be written as [24]:

$$T^{\alpha\beta}_{,\beta} = \frac{1}{\sqrt{g*}}\frac{\partial \sqrt{g*} T^{\alpha\beta}}{\partial \xi^\beta} + \Gamma^\alpha_{\gamma\beta} T^{\gamma\beta} \tag{B.23}$$

This can be discretised in finite volume in the following way. Partial integration gives:

$$\int_\Omega T^{\alpha\beta}_{,\beta} d\Omega = \int_\Omega \frac{\partial \sqrt{g*}\, T^{\alpha\beta}}{\partial \beta} d\Omega + \int_\Omega \Gamma^\alpha_{\gamma\beta} T^{\gamma\beta} d\Omega \tag{B.24}$$

$$\approx (\sqrt{g*}\, T^{\alpha 1})|^{i+\frac{1}{2},j}_{i-\frac{1}{2},j} \delta\xi^2 + (\sqrt{g*}\, T^{\alpha 2})|^{i,j+\frac{1}{2}}_{i,j-\frac{1}{2}} \delta\xi^1 + (\Gamma^\alpha_{\gamma\beta} T^{\gamma\beta}\sqrt{g*})|_{i,j}\, \delta\xi^1\delta\xi^2 \tag{B.25}$$

Applied to a U^1 cell, given that $\delta\xi^1 = \delta\xi^2 = 1$:

$$(p\sqrt{g*}\, g^{11})|^{i+1,j}_{i,j} + (p\sqrt{g*}\, g^{12})|^{i+\frac{1}{2},j+\frac{1}{2}}_{i+\frac{1}{2},j-\frac{1}{2}} + (\Gamma^1_{\gamma\beta} g^{\gamma\beta} p\sqrt{g*})|_{i+\frac{1}{2},j} \tag{B.26}$$

Applied to a U^2 cell, given that $\delta\xi^1 = \delta\xi^2 = 1$:

$$(p\sqrt{g*}\, g^{21})|^{(i+\frac{1}{2},j+\frac{1}{2})}_{(i-\frac{1}{2},j+\frac{1}{2})} + (p\sqrt{g*}\, g^{22})|^{(i,j+1)}_{(i,j)} + (\Gamma^2_{\gamma\beta} g^{\gamma\beta} p\sqrt{g*})|_{(i,j+\frac{1}{2})} \tag{B.27}$$

However, Kassels and Segal [25] suggested another discretisation, without Christoffel symbols. They omitted the Christoffel symbols by performing algebraic operations on the transformed equations based on metric identities. This is described in [25], the resulting discretisation is given below:

$$\int_\Omega (g^{\alpha\beta} p)_{,\beta}\, d\Omega \approx (p|_{i+\frac{1}{2},j} - p|_{i-\frac{1}{2},j})(g^{\alpha 1}\sqrt{g*})|_{i,j} + (p|_{i,j+\frac{1}{2}} - p|_{i,j-\frac{1}{2}})(g^{\alpha 2}\sqrt{g*})|_{i,j} \tag{B.28}$$

Applied to a U^1 cell at $i+\frac{1}{2}, j$:

$$\int_\Omega (g^{1\beta} p)_{,\beta}\, d\Omega \approx (p_{i+1,j} - p_{i,j})(g^{11}\sqrt{g*})|_{i+\frac{1}{2},j} + (p_{i+\frac{1}{2},j+\frac{1}{2}} - p|_{i+\frac{1}{2},j-\frac{1}{2}})(g^{12}\sqrt{g*})|_{i+\frac{1}{2},j} \tag{B.29}$$

Applied to a U^2 cell at $i, j+\frac{1}{2}$:

$$\int_\Omega (g^{2\beta} p)_{,\beta}\, d\Omega \approx (p_{i+\frac{1}{2},j+\frac{1}{2}} - p_{i-\frac{1}{2},j+\frac{1}{2}})(g^{21}\sqrt{g*})|_{i,j+\frac{1}{2}} + (p_{i,j+1} - p_{i,j})(g^{22}\sqrt{g*})|_{i,j+\frac{1}{2}} \tag{B.30}$$

For the time derivative, using contravariant components of vector $\vec{u}$, discretising over a finite volume, at location i, j, given that $d\xi^1 = d\xi^2 = 1$ results in:

$$\int_\Omega \frac{\partial U^\alpha}{\partial t} d\Omega \approx \left(\frac{\partial U^\alpha}{\partial t}\sqrt{g*}\, d\xi^1 d\xi^2\right)|_{i,j} = \left(\frac{\partial V^\alpha \frac{1}{\sqrt{g*}}}{\partial t}\sqrt{g*}\, d\xi^1 d\xi^2\right)|_{i,j} = \frac{\partial V^\alpha}{\partial t}|_{i,j} \tag{B.31}$$

For the right hand side, using contravariant components of vector $\vec{u}$ again, discretising over a finite volume, at location i, j, given that $d\xi^1 = d\xi^2 = 1$ results in:

$$-C_w \int_\Omega U^\alpha d\Omega \approx -C_w \left(U^\alpha \sqrt{g*}\, d\xi^1 d\xi^2\right)|_{i,j} = -C_w \left(V^\alpha\, d\xi^1 d\xi^2\right)|_{i,j} = -C_w V^\alpha|_{i,j} \tag{B.32}$$

Now these discretisations can be applied to equation 2, the total Semi-Discrete description for a U^1/V^1 cell becomes:

$$\frac{\partial V^1}{\partial t}|_{i+\frac{1}{2},j} + (p_{i+1,j} - p_{i,j})(g^{11}\sqrt{g*})|_{i+\frac{1}{2},j} + (p_{i+\frac{1}{2},j+\frac{1}{2}} - p_{i+\frac{1}{2},j-\frac{1}{2}})(g^{12}\sqrt{g*})|_{i+\frac{1}{2},j} = -C_w V^1|_{i,j} \tag{B.33}$$

$$\frac{\partial V^1}{\partial t}|_{i+\frac{1}{2},j} = (p_{i,j} - p_{i+1,j})(g^{11}\sqrt{g*})|_{i+\frac{1}{2},j} + (p_{i+\frac{1}{2},j-\frac{1}{2}} - p_{i+\frac{1}{2},j+\frac{1}{2}})(g^{12}\sqrt{g*})|_{i+\frac{1}{2},j} - C_w V^1|_{i,j} \tag{B.34}$$

And the total Semi-Discrete description for a U^2/V^2 cell:

$$\frac{\partial V^2}{\partial t}|_{i,j+\frac{1}{2}} + (p_{i+\frac{1}{2},j+\frac{1}{2}} - p_{i-\frac{1}{2},j+\frac{1}{2}})(g^{21}\sqrt{g*})|_{i,j+\frac{1}{2}} + (p_{i,j+1} - p_{i,j})(g^{22}\sqrt{g*})|_{i,j+\frac{1}{2}} = -C_w V^2|_{i,j} \tag{B.35}$$

$$\frac{\partial V^2}{\partial t}|_{i,j+\frac{1}{2}} = (p_{i-\frac{1}{2},j+\frac{1}{2}} - p_{i+\frac{1}{2},j+\frac{1}{2}})(g^{21}\sqrt{g*})|_{i,j+\frac{1}{2}} + (p_{i,j} - p_{i,j+1})(g^{22}\sqrt{g*})|_{i,j+\frac{1}{2}} - C_w V^2|_{i,j} \tag{B.36}$$

C

Stencils and Interpolation & Extrapolation of Metric Terms

In this appendix, a description is given on how all metric terms necessary for computation on curvilinear grids are determined. The metric terms occur in the semi discrete equations in Appendix B and Appendix E.

C.1. Computational Grid

To realise the curvilinear grid given in Figure C.1, a computational grid with a plus shape is defined as depicted next to it. The computational grid is equidistant with unit spacing. This property is essential and repeatedly used in derivations.

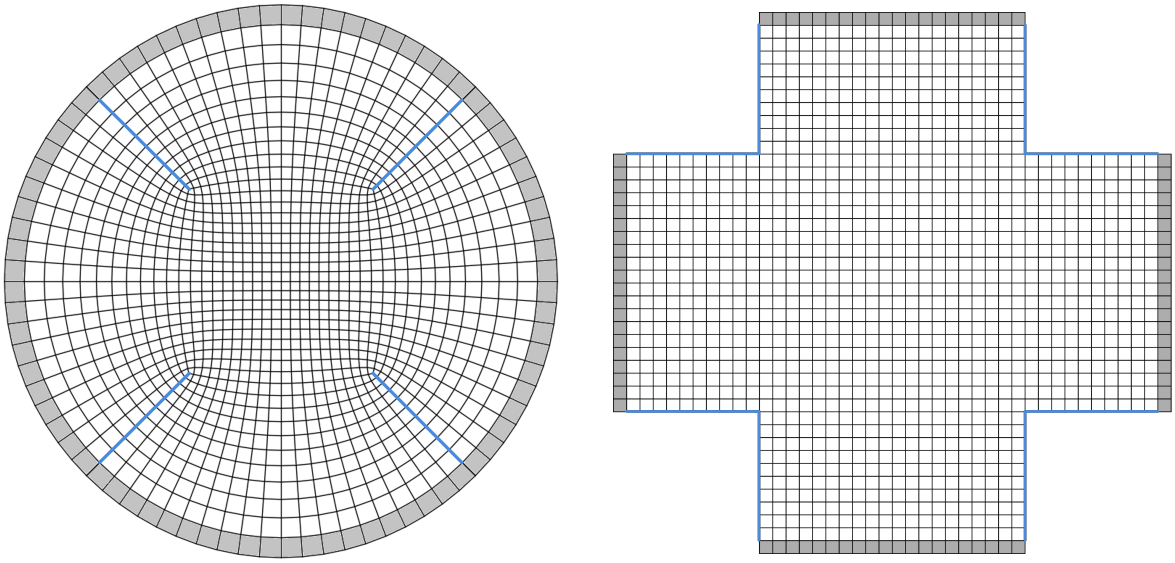

Figure C.1: Physical and corresponding equidistant computational grid, grey cells are ghost cells, blue edges are slits

C.2. Grid Derivatives

To determine all metric terms, the first step is to determine the covariant base vectors. These can be determined in the cell faces through finite differencing of the vertices. The covariant base vectors are parallel to the corresponding coordinate direction. This means that the covariant base vector in ξ^1 direction ($\vec{a}_{(1)}$) can be determined in faces where ξ^2 is constant and vice versa.

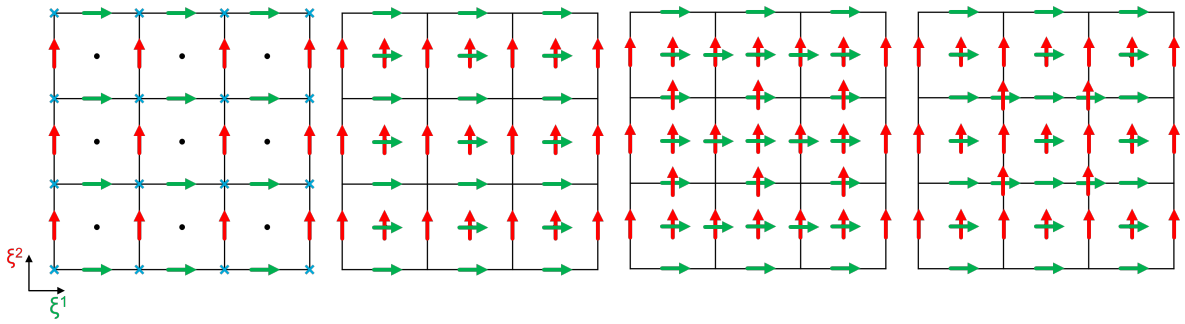

Figure C.2: Determination of basevectors, FLTR: Finite differencing, Interpolation to cell centres, interpolation to cell faces, interpolation to vertices

From the covariant base vectors in the cell faces, the complete set of base vectors can be determined through interpolation to the cell centres. The missing base vector in the cell faces (i.e. $\vec{a}_{(1)}$ in faces where ξ^2 is constant and vice versa) can be determined through interpolation from two cell centres again. This means that in every cell centre, full metric information is available. For every cell face that is not on the edge of the computational grid, full metric information is available. The base vectors are interpolated to the vertices in similar fashion to obtain full metric in the vertices. For illustration, these steps are visualised in Figure C.2.

Now all covariant base vectors are known in cell centres and cell faces, the covariant metric tensor can be determined (C.1). Using this, the contravariant metric tensor (C.2) and the cell area/volume can be determined (C.3). In tensor notation:

$$g_{\alpha\beta} = \vec{a}_{(\alpha)} \cdot \vec{a}_{(\beta)} \tag{C.1}$$

$$g^{\alpha\beta} = \vec{a}^{(\alpha)} \cdot \vec{a}^{(\beta)} = (g_{\alpha\beta})^{-1} \tag{C.2}$$

$$\sqrt{g*} = \sqrt{|g_{\alpha\beta}|} \tag{C.3}$$

C.3. Christoffel Symbols

Christoffel symbols (of the second kind) are determined through differencing of the covariant metric tensor. This means that these symbols can only be determined at locations with full metric information available at each side of the desired location. For the Christoffel symbols in cell centres, these are the cell faces surrounding the cell centre. For the Christoffel symbols in the cell faces, these are the vertices composing the face and the cell centres at each side of the face.

Because full metric information needs to be available at both sides of the desired Christoffel symbol location, this means that in in cell centres and faces adjacent to the edges of the computational domain, information is missing to determine Christoffel symbols. At locations where all metric information is available, the Christoffel symbols of the second kind are determined as follows, using tensor notation [32]:

$$\Gamma^{\alpha}_{\gamma\beta} = \vec{a}^{(\alpha)} \cdot \frac{\partial \vec{a}_{(\gamma)}}{\partial \xi^{\beta}} = \Gamma^{\alpha}_{\beta\gamma} \tag{C.4}$$

$$\Gamma^{\alpha}_{\gamma\beta} = \frac{1}{2} g^{\alpha\delta} \left(\frac{\partial g_{\delta\gamma}}{\partial \xi^{\beta}} + \frac{\partial g_{\delta\beta}}{\partial \xi^{\gamma}} - \frac{\partial g_{\gamma\beta}}{\partial \xi^{\delta}} \right) \tag{C.5}$$

Christoffel symbols of the first kind can then be found as follows:

$$\Gamma_{\alpha\beta\gamma} = g_{\alpha\delta}\Gamma^{\delta}_{\beta\gamma} = \frac{1}{2} \left(\frac{\partial g_{\alpha\gamma}}{\partial \xi^{\beta}} + \frac{\partial g_{\alpha\beta}}{\partial \xi^{\gamma}} - \frac{\partial g_{\beta\gamma}}{\partial \xi^{\alpha}} \right) \tag{C.6}$$

C.4. Slit Handling

The computational grid has edges that are located in the interior of the physical grid. These edges are located at on the sides of the 'arms' of the plus-shape. The slits are indicated as blue lines in Figure C.1. This will be referred to as a slit from now on. If the process described in Figure C.2 is performed to compute metric terms, this will result in missing metric values in the slit. This is because one of the covariant base vectors cannot be interpolated to the cell faces in the slit. The same holds for interpolating the base vectors in the vertices, which are necessary for the Christoffel symbols.

To obtain the full metric description in the slit (both covariant basevectors), metric information from across the slit can be used. In Figure C.3, the covariant base vectors around the slit are depicted. It can be seen that a switch in type of base vector is present in over the slit. This is also expected, since two curvilinear coordinate directions are coupled at the slit. This also gives the insight that the metric information can be used from across the slit to obtain full metric information at the slit faces and vertices. This is done by using the covariant base vectors from the other side of the slit in the interpolation routine described by Figure C.2. Depending on the slit location, a correction needs to be applied with a minus sign if the two coordinate directions oppose each other.

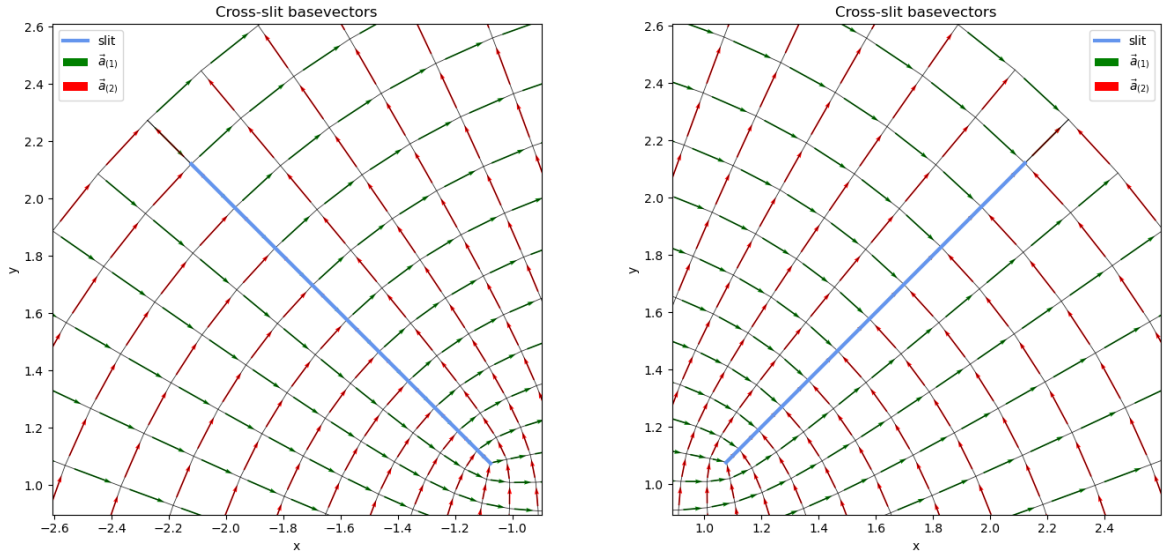

Figure C.3: Basevectors near the slit (blue). It can be seen that $\vec{a}_{(1)}$ has an equivalent definition of $\vec{a}_{(2)}$ across the slit in the left figure, and opposite in the right figure

At the cell faces in the slit, metric information can now be computed using C.1-C.3. The Christoffel symbols at faces and cell centres adjacent to the slit can be determined as described in section C.3.

C.5. Stencils

The stencils corresponding to the discretisation in Appendix B are depicted in Figure C.4. For the velocity cells, pressure values at the vertices of p cells are required. This will be obtained by linear interpolation of the four surrounding pressure values.

C.5.1. Slit Coupling

In the slit, a coupling between two coordinate directions is required. This coupling is depicted in Figure C.5. The staggered V^2 cells are coupled in the slits using their equivalent functionality as V^1 cell. The coupling has a corresponding correction of direction if the V^2 or V^1 direction would be of opposite sign. This is indicated by the + and - signs in the left of Figure C.5. This way, the computational grid can be coupled. To complete the stencils for the V^α cells in the slit, the corresponding pressure cells from across the slit were referenced as depicted in the right of Figure C.5. The required metric information for the grid deformation obtained as in section C.4.

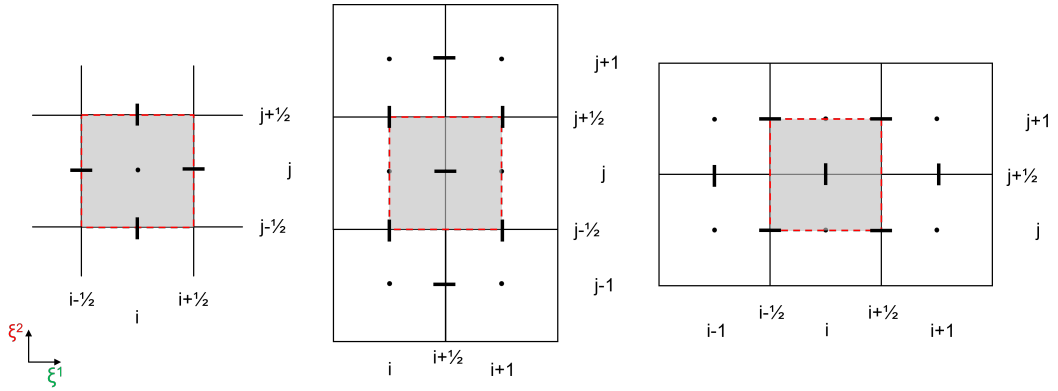

Figure C.4: Curvilinear stencils for p, V^1 and V^2

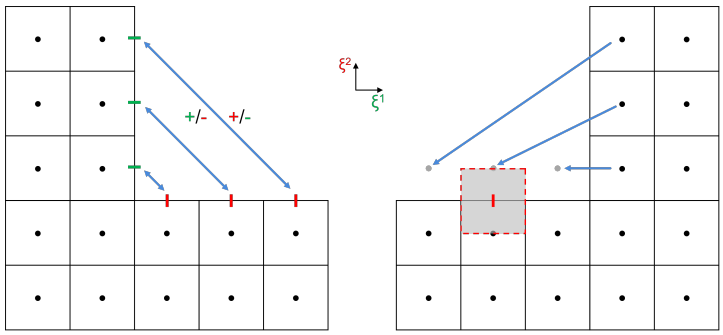

Figure C.5: Coupling with staggered cells in computational plus shaped grid

C.5.2. Corner Stencils

There are three V^α cells in each corner that have a relatively ambiguous stencil approach. Normally, four pressure cells are used to interpolate the pressure value at a vertex for the velocity stencil. However, at the interior corner of the computational grid there are only three available. Therefore at this corner vertex, for all velocity cells requiring a pressure value at this vertex, a three point linear interpolation is used. These velocity cells are depicted in the computational grid in Figure C.6 of which the left two are representations of the same cell. On the right, the interpolation is shown. If the different stencil introduces some inaccuracy, this importance is limited as such a corner only occurs four times in the entire grid. Also, as the grid refines, this stencil is of increasingly reduced importance. The accuracy of the corner stencil is evaluated in section 2.5.

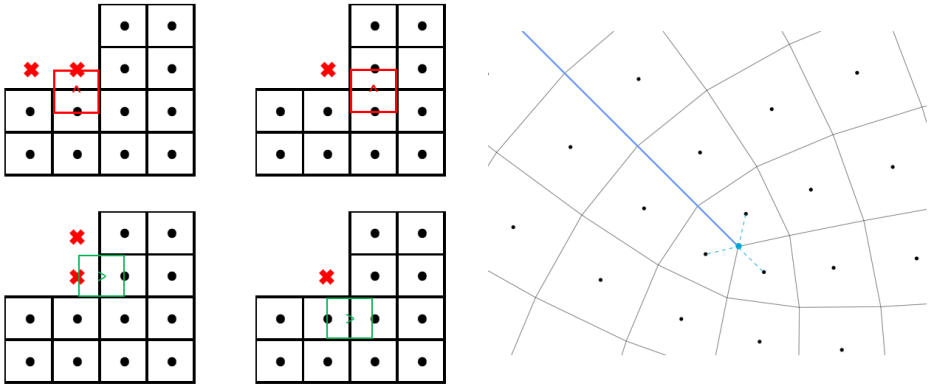

Figure C.6: Staggered cells in the interior corner point at the end of a slit. Three point linear interpolation will be used to interpolate the pressure to the corner vertex.

D

Pressure Interpolation Verification

In this appendix, the test to verify pressure interpolation at the boundary is described. This verification enables to implement a boundary condition in terms of pressures using pressure ghost values. Using pressure ghost cells to implement the boundary condition yields complete stencils for all velocities (normal and tangential to the boundary) near the boundary.

D.1. Test Setup

On the boundary, a desired pressure head can be prescribed through setting the ghost cell to a corresponding value. The value at the boundary is then determined through interpolation. To test this pressure interpolation on curved boundaries, it is desired to design a test in which certain convergence behaviour can be shown. This will be done by modelling the shallow water equations with unit density and a certain bottom friction as given below. For a constant pressure gradient, the velocity should therefore converge to a constant value regardless of boundary curvature. The discretisation of the shallow water equations with a bottom friction is also given in Appendix B.

$$\frac{1}{G}\frac{\partial p}{\partial t} + h\vec{\nabla}\cdot\vec{u} = 0 \tag{D.1}$$

$$\frac{\partial \vec{u}}{\partial t} + \vec{\nabla}p = -C_w\vec{u} \tag{D.2}$$

To set up the test, a domain with a certain pressure gradient in x direction of the domain was set up. At the west side of the domain, an over pressure can be described at boundary A. At the east side of the domain, an under pressure can be described on a curved boundary B, which follows the desired pressure gradient. At the north and south side of the domain, solid frictionless walls can be set up, by setting the normal velocity to zero. The pressure gradient normal to these boundaries was also set to zero. The domain for the test is depicted in Figure D.1.

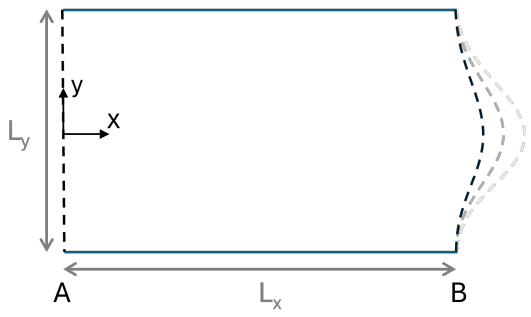

Figure D.1: Domain with increasing amounts of curvature at boundary B

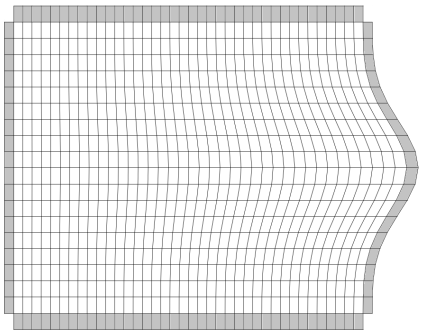

Figure D.2: Example of resulting curvilinear grid, grey cells are ghost cells

If the pressure interpolation is correct, the velocity should converge to a analytical value regardless of the curvature of boundary B. If the system has converged, this means that $\partial_t \vec{u} = 0$. This results in a zero y velocity and the constant analytical velocity in x direction of:

$$u_x = \frac{p_B - p_A}{L_x} \frac{1}{-C_w} \tag{D.3}$$

The curvature at the boundary B will be generated using a Gaussian shape. To ensure it is sufficiently orthogonal with the north and south boundary, a smooth taper function is added on top of the Gaussian. If this orthogonality at the North and South boundary is not the case, velocity sinks will occur at the corners of the domain as the velocity solution variables in the corners have a component in the direction of the solid north and south walls.

$$x(\xi^1, \xi^2) = L_x \frac{\xi^1}{N_{\xi^1}} + \beta \exp\left(-\frac{(\xi^2 - \frac{N_{\xi^2}}{2})^2}{2\,(0.2)^2} \right) W\left(\frac{\xi^2 - \frac{N_{\xi^2}}{2}}{N_{\xi^2}} \right) \left(\frac{\xi^1}{N_{\xi^1}} \right)^2 \tag{D.4}$$

$$y(\xi^1, \xi^2) = L_y \frac{\xi^2 - \frac{N_{\xi^2}}{2}}{N_{\xi^2}} \tag{D.5}$$

$$W(a) = \left(3a^2 - 2a^3\right)\left(1 - 3a^2 + 2a^3\right) \tag{D.6}$$

The curvature will be employed more towards the east side of the domain. This is done through a quadratic influence based on location, as can be seen in Equation D.4. The amount of curvature will be controlled through a linear parameter β. To generate the grid, a unit spaced rectangular computational grid with $\xi^\alpha \in \{0, ..., N_{\xi^\alpha}\}$ was set up and transformed a curvilinear grid based on Equation D.4. To ensure orthogonality at the top and bottom boundary, the mapping is applied only on the interior computational domain. Ghost cell layers are transformed afterwards by extrapolation neighbouring interior cell. An example of the resulting curvilinear grid is shown in Figure D.2.

D.1.1. Simulations

Three grids were set up with different Gaussian curvatures at the east boundary, with $\beta = 1.0$, 2.0 and 3.0 respectively. Three different grid resolutions were tested for each curvature, with a refinement ratio around $\sqrt{2}$. $N_{\xi^1}, N_{\xi^2} = 120, 100,\ 170, 140$ and $240, 200$ respectively. The other simulation parameters were kept constant and are given in Table D.1. The pressures at the two boundaries were introduced in a smooth fashion, to limit waves travelling through the domain because of the start up from zero.

Parameter	Symbol	Value	Unit
Gravitational constant	G	9.81	$m\,s^{-2}$
Water depth	h	2.0	m
Wave speed	$c = \sqrt{Gh}$	4.4294	$m\,s^{-1}$
Domain length	L_x	6.0	m
Domain width	L_y	5.0	m
Bottom friction coeff	C_w	9.0	s^{-1}
Overpressure	p_A	50.0	$kg\,m^{-1}s^{-2}$
Underpressure	p_B	20.0	$kg\,m^{-1}s^{-2}$
Simulated time	t_{tot}	50.0	s
Time step	Δt	0.0001	s

Table D.1: General simulation parameters for pressure interpolation test

D.1.2. Results

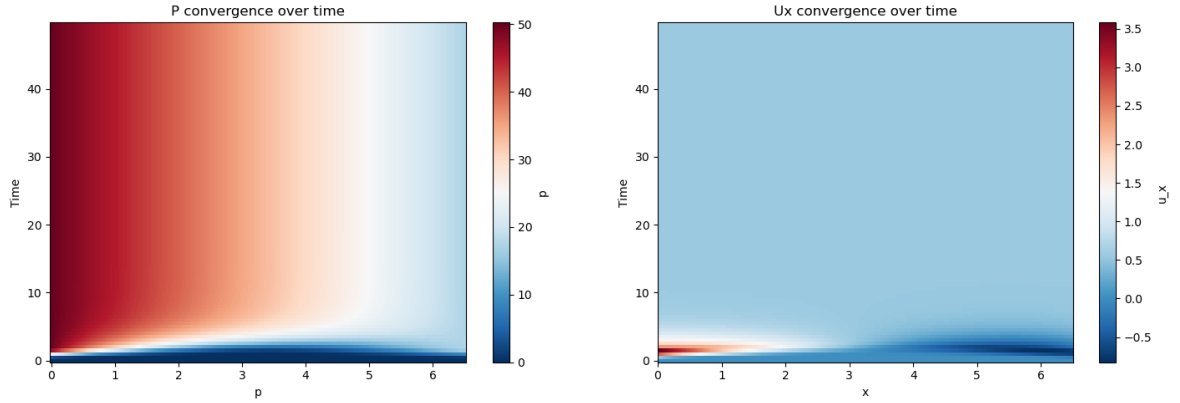

Figure D.3: Convergence over time with $N_{\xi 1}$=240 and β=2.0

Every simulation starts off in the same fashion as the interior pressure is still zero, and the boundaries are set to positive pressure values. A positive flow starts at the west boundary and a negative flow starts at the east boundary. As time continues, a constant pressure gradient is attained and the x velocity converges to the analytic velocity. The x velocity is recorded along a constant y line from the centre of the domain. This can be seen in Figure D.3. The analytical velocity that the simulation should converge to can be predicted using Equation D.3 and the simulation parameters. This value is $0.555^{m/s}$ and the simulation does converge to this analytical velocity as shown in Figure D.3. For the y velocity, the simulation should converge to 0. The results for u_x and u_y will be presented in the figures below. In Table D.2 the maximum deviation from the analytical values is presented.

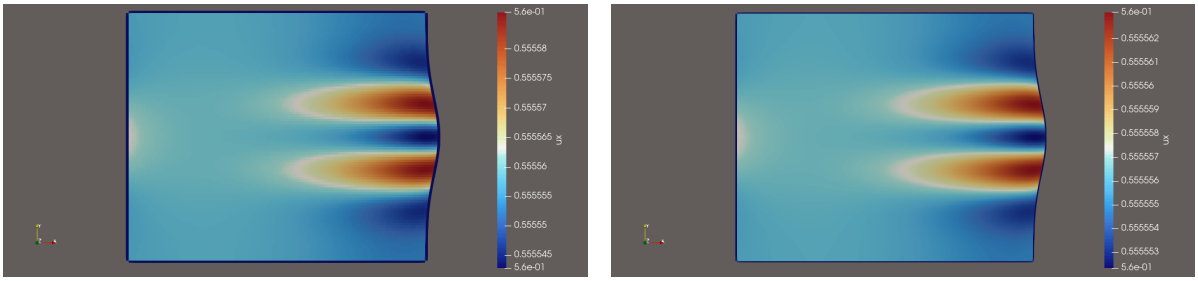

Figure D.4: Comparison of coarse and fine grid: u_x at t=50 for β=1.0

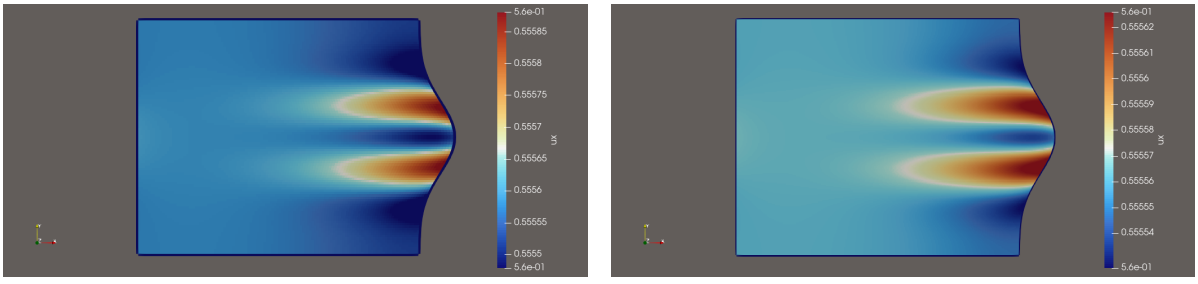

Figure D.5: Comparison of coarse and fine grid: u_x at t=50 for β=3.0

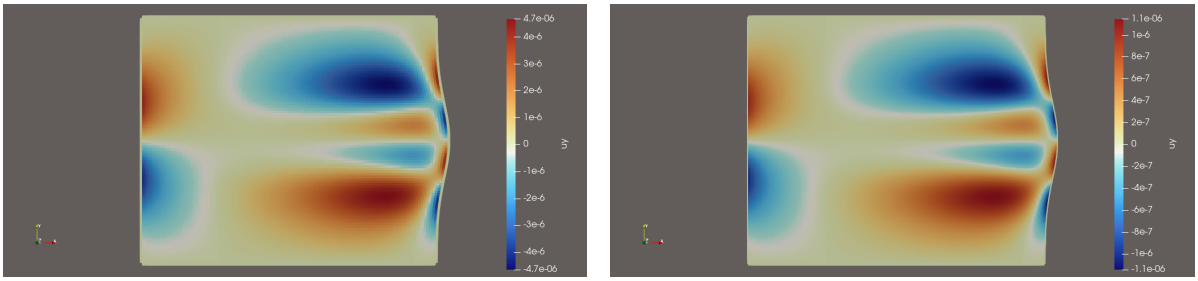

Figure D.6: Comparison of coarse and fine grid: u_y at t=50 for β=1.0

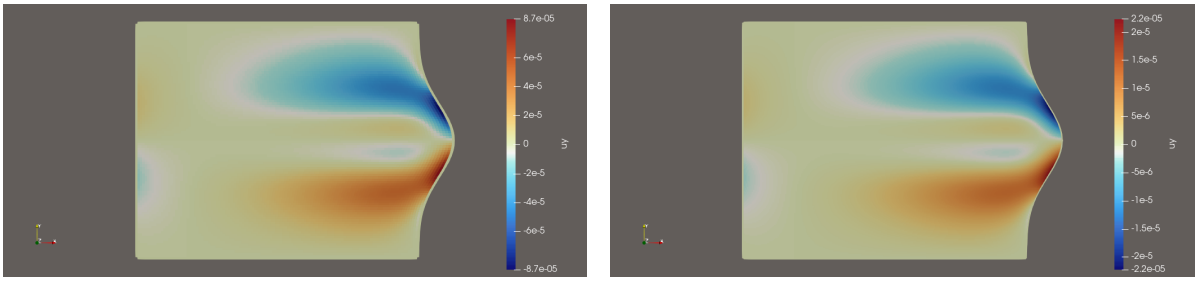

Figure D.7: Comparison of coarse and fine grid: u_y at t=50 for β=3.0

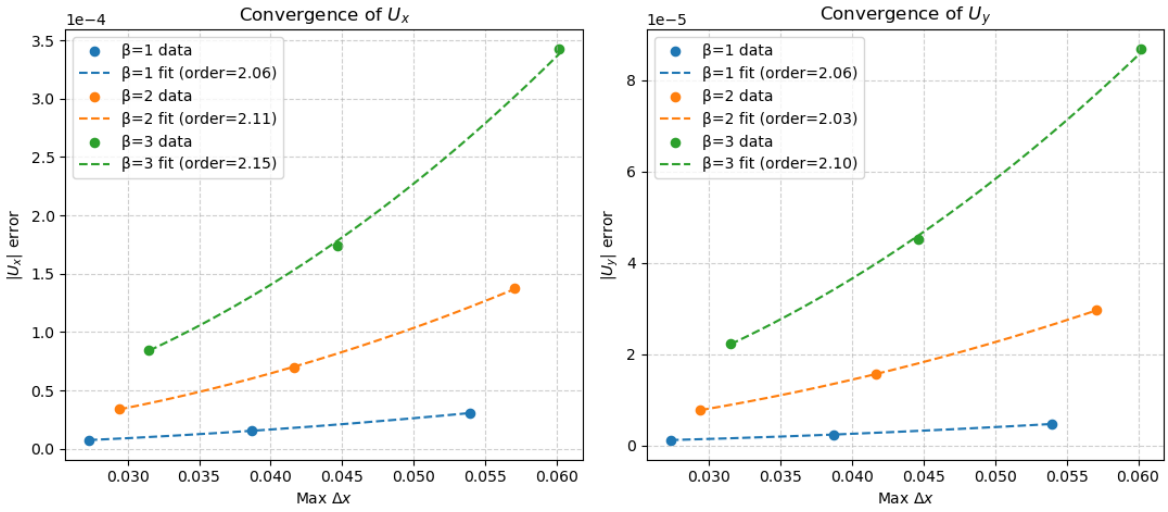

Figure D.8: Absolute error convergence trend for different grids

$N_{\xi 1}$	120		170		240	
β	u_x	u_y	u_x	u_y	u_x	u_y
1.0	3.070E-05	4.659E-06	1.558E-05	2.364E-06	7.559E-06	1.144E-06
2.0	1.377E-04	2.962E-05	6.979E-05	1.556E-05	3.394E-05	7.720E-06
3.0	3.424E-04	8.685E-05	1.741E-04	4.519E-05	8.501E-05	2.232E-05

Table D.2: Maximum absolute errors based on analytical values for different grid resolutions $N_{\xi 1}$ and boundary curvatures β

Ideally the boundary curvature should have a minimal influence on the result that is found. It can be concluded that this curvature does have an influence. The deviation increases with increasing curvature β but decreases with second-order grid convergence as shown in Figure D.8 and Table D.2, which is consistent with theoretical expectation.

E

Sommerfeld Boundary Condition

In this appendix, the Sommerfeld boundary condition will be derived in generalised curvilinear coordinates. The Sommerfeld boundary condition is an exact operator for planar waves hitting planar boundaries. For curved boundaries, it becomes an approximation. To derive a numerical implementation, a similar approach will be taken to the one of Wellens and Borsboom [37]. This means the Sommerfeld operator will be applied to potential function Φ. Intuition about the Sommerfeld operator will be given for planar boundaries, after which it will be applied to curved boundaries in generalised curvilinear coordinates.

E.1. Theoretical Framework

As a start, the wave equation normal to the boundary is formulated:

$$\left(\frac{\partial^2}{\partial t^2} - c^2\frac{\partial^2}{\partial n^2}\right)\Phi = 0 \tag{E.1}$$

Factorisation yields the following expression, in which the two factors represent propagation along characteristic lines $n \mp ct =$ constant:

$$\left(\frac{\partial}{\partial t} - c\frac{\partial}{\partial n}\right)\left[\left(\frac{\partial}{\partial t} + c\frac{\partial}{\partial n}\right)\Phi\right] = 0 \tag{E.2}$$

$\left(\frac{\partial}{\partial t} + c\frac{\partial}{\partial n}\right)\Phi$ represents the incoming characteristic. Setting the incoming characteristic to zero, yields the Sommerfeld boundary condition:

$$\left[\left(\frac{\partial}{\partial t} + c\frac{\partial}{\partial n}\right)\Phi\right] = 0 \tag{E.3}$$

The coefficient c is the wave speed of the incoming characteristic wave that should be cancelled. This can be tuned to match the incoming wave of a certain outgoing wave. Thereby, it can be seen as exactly absorbing the outgoing wave. The coefficient c can be set as the apparent phase speed of a wave, depending on the incidence direction. This apparent phase speed is defined as $c_0 = \frac{c}{\cos\theta_0}$ depending on the desired incidence angle with exact absorbance [37].

$$\left(\frac{\partial}{\partial t} + c_0\frac{\partial}{\partial n}\right)\Phi = 0 \tag{E.4}$$

$$\left(\frac{\partial}{\partial t} + \frac{c}{\cos\theta_0}\frac{\partial}{\partial n}\right)\Phi = 0 \tag{E.5}$$

For waves whose incidence angle differs from the tuned angle, partial reflection occurs. This can be explained by decomposing the wave into a linear combination of wave components. The component aligned with the tuned characteristic direction is absorbed by the boundary condition, while the remaining components are not absorbed and therefore give partial reflection.

E.2. Implementation

Now that the framework of the Sommerfeld operator has been set, the implementation at the boundary can be derived. In linear potential theory, pressures and velocities can be defined through temporal and spatial derivatives of the potential function Φ. The linearised Bernoulli equation can be used to express pressure in terms of the temporal derivative of potential Φ:

Following linearised Bernoulli:

$$\rho\frac{\partial\Phi}{\partial t} + p' + \rho G\zeta = 0 \tag{E.6}$$

In which ρ is the density, p' are pressure fluctuations and ζ is the free-surface elevation. $\rho G\zeta$ thereby gives the pressure head. At the free surface, p' = 0 due to the dynamic boundary condition (atmospheric pressure at free surface). For unit density, with p the pressure head, this gives:

$$\frac{\partial\Phi}{\partial t} = -G\zeta = -p \tag{E.7}$$

Therefore, the time derivative of Φ at the boundary can be substituted with $-p$. Spatial derivatives of the potential function give velocities. The spatial derivative in normal direction gives the velocity normal to the boundary, u_n:

$$\frac{\partial\Phi}{\partial n} = u_n \tag{E.8}$$

To evaluate this in generalised curvilinear coordinates, the gradient operator needs to be projected onto the outward normal vector. A normal derivative is therefore the dot product of the gradient operator and the unit vector in the direction of interest. At ξ^1 is constant face, the normal vector aligns with contravariant base vector $\vec{a}^{(1)}$. This can be seen in Figure E.1. The normal vector will therefore be expressed with contravariant basis and covariant components.

$$\frac{\partial\Phi}{\partial n} = \vec{n}\cdot\vec{\nabla}\Phi \tag{E.9}$$

$$\vec{n}\cdot(\vec{a}^{(\beta)}\frac{\partial\Phi}{\partial\xi^\beta}) \tag{E.10}$$

$$n_\alpha\vec{a}^{(\alpha)}\cdot(\vec{a}^{(\beta)}\frac{\partial\Phi}{\partial\xi^\beta}) \tag{E.11}$$

$$n_\alpha g^{\alpha\beta}\frac{\partial\Phi}{\partial\xi^\beta} \tag{E.12}$$

Given that the normal vector aligns with the contravariant basevector $\vec{a}^{(1)}$ and has unit length:

$$||\vec{n}|| = 1 \quad\Rightarrow\quad n_1 = \frac{1}{\sqrt{\vec{a}^{(1)}\cdot\vec{a}^{(1)}}} = \frac{1}{\sqrt{g^{11}}}\ ,\ \ n_2 = 0 \tag{E.13}$$

The gradient gives the covariant velocity components. However due to the contravariant metric tensor in front, it can be expressed in contravariant components:

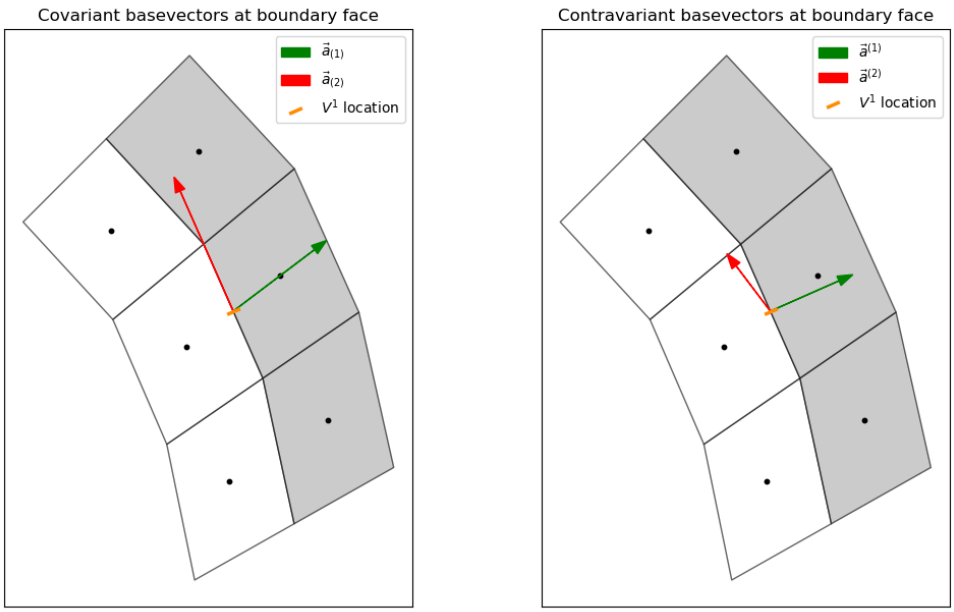

Figure E.1: Basevectors at boundary, grey cells are ghost cells

$$n_1(g^{1\beta}\frac{\partial \Phi}{\partial \xi^\beta}) \tag{E.14}$$

$$n_1(g^{1\beta}U_\beta) = n_1 U^1 \tag{E.15}$$

Now the following relation holds at the boundary. An update for the pressure is desired at the new time level t^{n+1}. Therefore a relation needs to be found to substitute unknown $U^1|_b^{n+1}$.

$$-p|_b^{n+1} + c_0\, n_1\, U^1|_b^{n+1} = 0 \tag{E.16}$$

For this the momentum equation normal to the boundary is used:

$$\vec{n}\cdot\left(\frac{\partial \vec{u}}{\partial t} + (\vec{\nabla} p)\right) = 0 \tag{E.17}$$

$$n_1\vec{a}^{(1)}\cdot\left(\frac{\partial U^\alpha}{\partial t}\vec{a}_{(\alpha)}\right) + n_1\vec{a}^{(1)}\left(\vec{\nabla} p\right) = 0 \tag{E.18}$$

$$n_1\vec{a}^{(1)}\cdot\left(\frac{\partial U^\alpha}{\partial t}\vec{a}_{(\alpha)}\right) + n_1\vec{a}^{(1)}\left(\vec{a}^{(\beta)}\frac{\partial p}{\partial \xi^\beta}\right) = 0 \tag{E.19}$$

$$n_1\frac{\partial U^1}{\partial t} + n_1\left(g^{1\beta}\frac{\partial p}{\partial \xi^\beta}\right) = 0 \tag{E.20}$$

Discretising this in time using an explicit update at the boundary ($|_b$):

$$n_1\frac{U^1|_b^{n+1} - U^1|_b^n}{\Delta t} + n_1\left(g^{11}\frac{\partial p}{\partial \xi^1}|_b^n + g^{12}\frac{\partial p}{\partial \xi^2}|_b^n\right) = 0 \tag{E.21}$$

$$n_1 U^1|_b^{n+1} = n_1 U^1|_b^n - \Delta t\, n_1\left(g^{11}\frac{\partial p}{\partial \xi^1}|_b^n + g^{12}\frac{\partial p}{\partial \xi^2}|_b^n\right) \tag{E.22}$$

Substitution of $U^1|_b^{n+1}$ in the Sommerfeld BC:

$$-p|_b^{n+1} + c_0 \left[n_1 U^1|_b^n - \Delta t \, n_1 \left(g^{11} \frac{\partial p}{\partial \xi^1}|_b^n + g^{12} \frac{\partial p}{\partial \xi^2}|_b^n \right) \right] = 0 \tag{E.23}$$

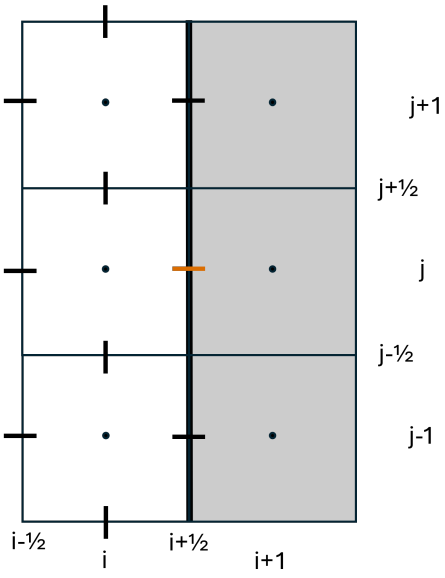

Figure E.2: Computational grid and stencil at boundary. Grey cells are ghost cells.

$p|_b^{n+1}$ can be obtained through interpolation of the ghost value and the interior value. This is validated in the pressure test in subsection 2.6.1.

$$p|_b^{n+1} = p|_{i+\frac{1}{2},j}^{n+1} = \frac{1}{2}(p|_{i,j}^{n+1} + p|_{i+1,j}^{n+1}) \tag{E.24}$$

The pressure value in the interior is known based on the explicit update for timestep t^{n+1}. This means the ghost cell value has to be set.

This gives:

$$-\frac{1}{2}(p|_{i,j}^{n+1} + p|_{i+1,j}^{n+1}) + c_0 \left[n_1 \, U^1|_b^n - \Delta t \, n_1 \left(g^{11} \frac{\partial p}{\partial \xi^1}|_b^n + g^{12} \frac{\partial p}{\partial \xi^2}|_b^n \right) \right] = 0 \tag{E.25}$$

$$\frac{1}{2}(p|_{i,j}^{n+1} + p|_{i+1,j}^{n+1}) = c_0 \left[n_1 \, U^1|_b^n - \Delta t \, n_1 \left(g^{11} \frac{\partial p}{\partial \xi^1}|_b^n + g^{12} \frac{\partial p}{\partial \xi^2}|_b^n \right) \right] \tag{E.26}$$

$$p|_{i+1,j}^{n+1} = -p|_{i,j}^{n+1} + 2c_0 \left[n_1 \, U^1|_b^n - \Delta t \, n_1 \left(g^{11} \frac{\partial p}{\partial \xi^1}|_b^n + g^{12} \frac{\partial p}{\partial \xi^2}|_b^n \right) \right] \tag{E.27}$$

The pressure derivatives are found by finite differencing on the computational equidistant grid with unit spacing:

$$\frac{\partial p}{\partial \xi^1}|_b^n = (p|_{i+1,j}^n - p|_{i,j}^n) \tag{E.28}$$

$$\frac{\partial p}{\partial \xi^2}|_b^n = (p|_{i+\frac{1}{2},j+\frac{1}{2}}^n - p|_{i+\frac{1}{2},j-\frac{1}{2}}^n) \tag{E.29}$$

$p|^n_{i+\frac{1}{2},j\pm\frac{1}{2}}$ can be found by four point interpolation of the surrounding values.

As metric scaled contravariant velocity components are used as solution variables, substitution of $U^1|^n_b = \frac{V^1}{\sqrt{g*}}|^n_b$ gives:

$$p|^{n+1}_{i+1,j} = -p|^{n+1}_{i,j} + 2c_0 \left[n_1 \frac{V^1}{\sqrt{g*}}|^n_b - \Delta t\, n_1 \left(g^{11} \frac{\partial p}{\partial \xi^1}|^n_b + g^{12} \frac{\partial p}{\partial \xi^2}|^n_b \right) \right] \tag{E.30}$$

As $n_1 = \frac{1}{\sqrt{g^{11}}}$

$$p|^{n+1}_{i+1,j} = -p|^{n+1}_{i,j} + 2c_0 \left[\frac{1}{\sqrt{g^{11}}} \frac{V^1}{\sqrt{g*}}|^n_b - \Delta t\, \frac{1}{\sqrt{g^{11}}} \left(g^{11} \frac{\partial p}{\partial \xi^1}|^n_b + g^{12} \frac{\partial p}{\partial \xi^2}|^n_b \right) \right] \tag{E.31}$$

F

Engquist-Majda Operators

The higher-order Generating Absorbing Boundary Conditions (GABCs) in this work are based on the formulations of Engquist and Majda [10]. Two second-order GABCs are implemented, of which one is based on a Planar Engquist-Majda (PEM) operator and one based on Circular Engquist-Majda (CEM) operator. Engquist and Majda derive these operators for unit wave speed, which therefore does not occur in their formulations. In this appendix, the original forms stated are adapted to apply in generalised curvilinear coordinates and the circular boundary stated in this work.

F.1. Planar Engquist-Majda (PEM)

In Cartesian coordinates, the following operator is defined to absorb waves w travelling to the left at the left boundary, in negative x direction.

$$\left(\frac{\partial^2}{\partial x \partial t} - \frac{\partial^2}{\partial t^2} + \frac{1}{2}\frac{\partial^2}{\partial y^2}\right) w|_{x=0} = 0 \tag{F.1}$$

The outward normal corresponds to negative x direction, and the tangential direction along the boundary corresponds to y. Substitution of these coordinates and applying the operator to potential Φ:

$$\left(-\frac{\partial^2}{\partial n \partial t} - \frac{\partial^2}{\partial t^2} + \frac{1}{2}\frac{\partial^2}{\partial \tau \partial \tau}\right) \Phi = 0 \tag{F.2}$$

Engquist and Majda work with unit wave speed. This is equivalent to working with a transformed time $\tilde{t} = ct$. Taking derivatives with respect to $\tilde{t}$ then gives $\frac{\partial}{\partial \tilde{t}} = \frac{1}{c}\frac{\partial}{\partial t}$. Therefore, in the operator for the wave equation with non-unit wave speed, every time derivative has to be multiplied with a $\frac{1}{c}$ term. This yields the following expression:

$$\left(-\frac{1}{c}\frac{\partial^2}{\partial n \partial t} - \frac{1}{c^2}\frac{\partial^2}{\partial t^2} + \frac{1}{2}\frac{\partial^2}{\partial \tau \partial \tau}\right) \Phi = 0 \tag{F.3}$$

Multiplied by c^2 results in the final form used in this work:

$$\left(-\frac{\partial^2}{\partial t^2} - c\frac{\partial^2}{\partial n \partial t} + \frac{c^2}{2}\frac{\partial^2}{\partial \tau \partial \tau}\right) \Phi = 0 \tag{F.4}$$

F.2. Circular Engquist-Majda (CEM)

To implement an ABC suited for circular boundaries, a start is made by taking the second-order Engquist-Majda operator for circular boundaries. Engquist and Majda derive this operator for unit wave speed, which therefore does not occur in their formulation. The operator in polar coordinates, (r, φ), is stated as follows:

$$\left(\frac{\partial^3}{\partial r \partial t^2} + \frac{\partial^3}{\partial t^3} - \frac{1}{2a^2}\frac{\partial^3}{\partial t \partial \varphi^2} + \frac{1}{2a}\frac{\partial^2}{\partial t^2} + \frac{1}{2a^3}\frac{\partial^2}{\partial \varphi^2}\right) w|_{r=a} = 0 \tag{F.5}$$

Engquist and Majda state that at $r = a$ with $r \to \infty$, an outgoing wave has the form:

$$\frac{f(r-t)}{r^{\frac{1}{2}}}\left(a(\varphi) + \mathcal{O}\left(\frac{1}{r}\right)\right) \tag{F.6}$$

They also present a first-order condition which annihilates $\frac{f(r-t)}{r^{\frac{1}{2}}}(a(\varphi))$ on $r = 0$, and state that Equation F.5 will compensate for waves with angular dependence, when the wave is not quite a spherical wave. The form is again adapted to include wave speed c:

$$\left(\frac{1}{c^2}\frac{\partial^3}{\partial r \partial t^2} + \frac{1}{c^3}\frac{\partial^3}{\partial t^3} - \frac{1}{c}\frac{1}{2a^2}\frac{\partial^3}{\partial t \partial \varphi^2} + \frac{1}{c^2}\frac{1}{2a}\frac{\partial^2}{\partial t^2} + \frac{1}{2a^3}\frac{\partial^2}{\partial \varphi^2}\right) w|_{r=a} = 0 \tag{F.7}$$

We multiply the entire equation with c^3, to arrive at the following:

$$\left(c\frac{\partial^3}{\partial r \partial t^2} + \frac{\partial^3}{\partial t^3} - c^2\frac{1}{2a^2}\frac{\partial^3}{\partial t \partial \varphi^2} + c\frac{1}{2a}\frac{\partial^2}{\partial t^2} + c^3\frac{1}{2a^3}\frac{\partial^2}{\partial \varphi^2}\right) w|_{r=a} = 0 \tag{F.8}$$

The form will now be adapted to implement in generalised curvilinear coordinates. A start is made through expressing the gradient operator in polar coordinates.

$$\vec{\nabla} = \frac{\partial}{\partial r}\vec{a}_r + \frac{1}{r}\frac{\partial}{\partial \varphi}\vec{a}_\varphi \tag{F.9}$$

As $\vec{a}_\varphi$ represents the tangential unit vector in this formulation, $\frac{1}{r}\frac{\partial}{\partial \varphi}$, can be substituted by $\frac{\partial}{\partial \tau}$. The fact that r is equal to the normal direction on the circular boundary, allows to substitute n for r.

As $r = a$ on the boundary, substitution of the coordinates and application on potential Φ yields:

$$\left(c\frac{\partial^3}{\partial n \partial t^2} + \frac{\partial^3}{\partial t^3} - c^2\frac{1}{2}\frac{\partial^3}{\partial t(\partial \tau)^2} + c\frac{1}{2a}\frac{\partial^2}{\partial t^2} + c^3\frac{1}{2a}\frac{\partial^2}{(\partial \tau)^2}\right)\Phi = 0 \tag{F.10}$$

G

Higher-Order Implementation

In this appendix, different building blocks are derived for implementation of the second-order Engquist-Majda boundary conditions stated in Appendix F. This starts with a second-order tangential derivative for scalar quantities in generalised curvilinear coordinates. After that, the analytical components needed to prescribe a desired incoming wave, thereby forming a GABC, are derived. This analytical formulation likewise requires the evaluation of a scalar second-order tangential derivative in generalised curvilinear coordinates.

The second-order tangential derivative will first be worked out for pressure, which serves as a solution variable and is used for the absorbing part of the wave. The resulting operator is then applied to a known, analytically prescribed incoming wave. All derivations are worked out in generalised curvilinear coordinates for a boundary face located at a ξ^1 = constant boundary. However, the procedure is similar for other boundaries.

G.1. Second-Order Tangential Derivative

For the application of the second-order absorbing boundary condition, a correct formula for the following relation needs to be found:

$$\frac{\partial^2 p}{\partial \tau \partial \tau} \tag{G.1}$$

A start is made by splitting the derivative and realising that the the tangential derivative is the dot product of the tangential unit vector $\vec{\tau}$ and the gradient operator $\vec{\nabla}$:

$$\frac{\partial^2 p}{\partial \tau \partial \tau} = \frac{\partial}{\partial \tau}\left(\frac{\partial p}{\partial \tau}\right) \tag{G.2}$$

$$\frac{\partial}{\partial \tau} = \vec{\tau} \cdot \vec{\nabla} \tag{G.3}$$

At the boundary face, one of the covariant base vectors is exactly tangential to the cell face. For a ξ^1 constant boundary, this be seen in Figure G.1. The tangential vector at the boundary face of interest aligns exactly with the covariant base vector $\vec{a}_{(2)}$. The tangential vector is therefore written in contravariant components with covariant basis.

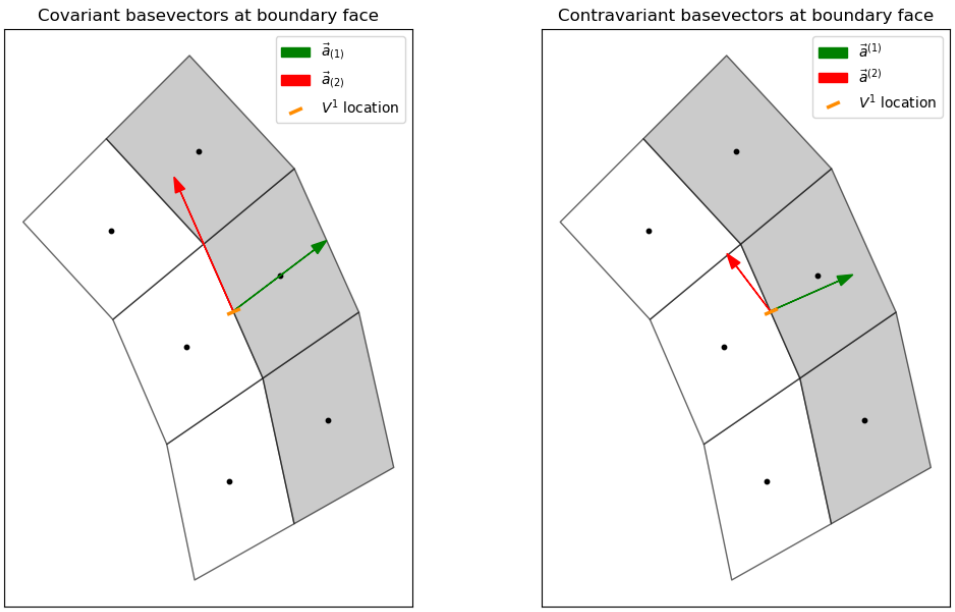

Figure G.1: Base vectors at boundary face for V^1 component

$$\frac{\partial^2 p}{\partial \tau \partial \tau} = \vec{\tau} \cdot \vec{\nabla}(\vec{\tau} \cdot \vec{\nabla} p) = \tag{G.4}$$

$$\vec{\tau} \cdot \vec{\nabla}(\tau^\alpha \vec{a}_{(\alpha)} \cdot \vec{a}^{(\beta)} \frac{\partial p}{\partial \xi^\beta}) = \tag{G.5}$$

$$\tau^\gamma \frac{\partial}{\partial \xi^\gamma}(\tau^\alpha \frac{\partial p}{\partial \xi^\alpha}) \tag{G.6}$$

The gradient operator is has covariant components and a contravariant basis. Therefore, the basis of the tangential vector and gradient operator reduce to the Kronecker delta exactly. Therefore, no Christoffel symbols appear in the previous relation. It is possible to first apply the gradient operator in Equation G.5, and then evaluate the relation further. This would result in Christoffel symbols that would cancel each other in a next step, because the contravariant and covariant bases vary in an opposite way to each other. Continuing; applying the product rule gives:

$$\tau^\gamma \left(\frac{\partial \tau^\alpha}{\partial \xi^\gamma} \frac{\partial p}{\partial \xi^\alpha} + \tau^\alpha \frac{\partial^2 p}{\partial \xi^\gamma \partial \xi^\alpha} \right) \tag{G.7}$$

Using the properties of the tangential vector at the ξ^1 = constant face;

$$||\vec{\tau}|| = 1 \quad \Rightarrow \quad \tau^2 = \frac{1}{\sqrt{\vec{a}_{(2)} \cdot \vec{a}_{(2)}}} = \frac{1}{\sqrt{g_{22}}}, \quad \tau^1 = 0 \tag{G.8}$$

Equation G.7 reduces to:

$$\frac{\partial^2 p}{\partial \tau \partial \tau} = \frac{1}{\sqrt{g_{22}}} \left(\frac{\partial (g_{22})^{-1/2}}{\partial \xi^2} \frac{\partial p}{\partial \xi^2} + \frac{1}{\sqrt{g_{22}}} \frac{\partial^2 p}{\partial \xi^2 \partial \xi^2} \right) \tag{G.9}$$

This can be further simplified using the product rule:

$$\left((g_{22})^{-1/2}\frac{\partial(g_{22})^{-1/2}}{\partial\xi^2}\frac{\partial p}{\partial\xi^2}+\frac{1}{g_{22}}\frac{\partial^2 p}{\partial\xi^2\partial\xi^2}\right)= \tag{G.10}$$

$$\left(\frac{1}{2}\frac{\partial(g_{22})^{-1}}{\partial\xi^2}\frac{\partial p}{\partial\xi^2}+\frac{1}{g_{22}}\frac{\partial^2 p}{\partial\xi^2\partial\xi^2}\right)= \tag{G.11}$$

$$\tag{G.12}$$

Applying the chain rule:

$$\left(\frac{1}{g_{22}}\frac{\partial^2 p}{\partial\xi^2\partial\xi^2}+\frac{1}{2}\frac{\partial(g_{22})^{-1}}{\partial\xi^2}\frac{\partial p}{\partial\xi^2}\right)= \tag{G.13}$$

$$\left(\frac{1}{g_{22}}\frac{\partial^2 p}{\partial\xi^2\partial\xi^2}-\frac{1}{2}(g_{22})^{-2}\frac{\partial g_{22}}{\partial\xi^2}\frac{\partial p}{\partial\xi^2}\right)= \tag{G.14}$$

$$\frac{1}{g_{22}}\left(\frac{\partial^2 p}{\partial\xi^2\partial\xi^2}-\frac{1}{2}\frac{1}{g_{22}}\frac{\partial g_{22}}{\partial\xi^2}\frac{\partial p}{\partial\xi^2}\right) \tag{G.15}$$

$\frac{\partial g_{22}}{\partial\xi^2}$ can be written as a Christoffel symbol using the product rule:

$$\frac{\partial g_{22}}{\partial\xi^2}=\frac{\partial(\vec{a}_{(2)}\cdot\vec{a}_{(2)})}{\partial\xi^2}=2\vec{a}_{(2)}\cdot\frac{\partial\vec{a}_{(2)}}{\partial\xi^2}= \tag{G.16}$$

$$2\vec{a}_{(2)}\cdot\vec{a}_{(\alpha)}\cdot\left(\vec{a}^{(\alpha)}\cdot\frac{\partial\vec{a}_{(2)}}{\partial\xi^2}\right)=2\vec{a}_{(2)}\cdot\vec{a}_{(\alpha)}\cdot\Gamma^{\alpha}_{22}= \tag{G.17}$$

$$2g_{2\alpha}\cdot\Gamma^{\alpha}_{22}=2\Gamma_{222} \tag{G.18}$$

So:

$$\frac{\partial^2 p}{\partial\tau\partial\tau}=\frac{1}{g_{22}}\left(\frac{\partial^2 p}{\partial\xi^2\partial\xi^2}-\frac{\Gamma_{222}}{g_{22}}\frac{\partial p}{\partial\xi^2}\right) \tag{G.19}$$

G.2. GABC Building Blocks

For the computation of the right hand side in the second-order GABC formulations, the same operator will be applied to a desired incoming potential. This results in the following for the PEM and CEM respectively:

$$RHS=\left(-\frac{\partial^2}{\partial t^2}-c\frac{\partial^2}{\partial t\partial n}+\frac{c^2}{2}\frac{\partial^2}{\partial\tau\partial\tau}\right)\Phi_{in} \tag{G.20}$$

$$RHS=\left(c\frac{\partial^3}{\partial n\partial t^2}+\frac{\partial^3}{\partial t^3}-\frac{c^2}{2}\frac{\partial^3}{\partial t\partial\tau\partial\tau}+\frac{c}{2a}\frac{\partial^2}{\partial t^2}+\frac{c^3}{2a}\frac{\partial^2}{\partial\tau\partial\tau}\right)\Phi_{in} \tag{G.21}$$

Φ_{in} is known in the physical space clearly, expressed in Cartesian coordinates. To implement it in curvilinear coordinates, a formulation needs to be found that takes the transformation into account clearly. For this, a few properties are derived or stated below. After this, the various terms in the equations above are covered, which are used to construct the full analytical description for each description.

First of all, for the long crested wave to be introduced over the boundary, $\vec{k}$ is constant in space. This can be used in the derivation of the gradient of Φ.

$$\vec{\nabla}\Phi=\vec{a}^{(\alpha)}\cdot\frac{\partial}{\partial\xi^{\alpha}}[Ae^{i(\vec{k}\cdot\vec{x}-\omega t+\varepsilon)}]=\vec{a}^{(\alpha)}\cdot\frac{\partial(i\vec{k}\cdot\vec{x})}{\partial\xi^{\alpha}}\Phi \tag{G.22}$$

$\vec{k}$ is independent of location, and contraction with either basis in the expression returns the corresponding components:

$$\vec{\nabla}\Phi = \vec{a}^{(\alpha)} \cdot i\vec{k} \cdot \frac{\partial \vec{x}}{\partial \xi^{\alpha}}\Phi = \vec{a}^{(\alpha)} \cdot i\vec{k} \cdot \vec{a}_{(\alpha)}\Phi = i\vec{a}^{(\alpha)} \cdot k_{\alpha}\Phi = ik^{\alpha} \cdot \vec{a}_{(\alpha)}\Phi \tag{G.23}$$

So the gradient operator returns a covariant base vector combined with the wave vector. Without the basis of the gradient this would return covariant components. This is also expected because the gradient transforms covariantly. Equation G.23 will be used in the following derivations.

G.2.1. Time Derivatives

As time is not transformed, time derivatives are trivial:

$$\frac{\partial^3 \Phi_{in}}{\partial t^3} = (-i\omega)^3 \Phi_{in} = i\omega^3 \Phi_{in} \tag{G.24}$$

$$\frac{\partial^2 \Phi_{in}}{\partial t^2} = (-i\omega)^2 \Phi_{in} = -\omega^2 \Phi_{in} \tag{G.25}$$

$$\frac{\partial \Phi_{in}}{\partial t} = -i\omega \Phi_{in} \tag{G.26}$$

G.2.2. Mixed Normal and Time Derivatives

The time derivative in the mixed derivative is similar as the spatial coordinates are independent of time, leaving:

$$\frac{\partial^2 \Phi_{in}}{\partial t \partial n} = -i\omega \frac{\partial \Phi_{in}}{\partial n} = -i\omega \vec{n} \cdot \vec{\nabla}\Phi_{in} \tag{G.27}$$

$$\frac{\partial^3 \Phi_{in}}{\partial t^2 \partial n} = -\omega^2 \frac{\partial \Phi_{in}}{\partial n} = -\omega^2 \vec{n} \cdot \vec{\nabla}\Phi_{in} \tag{G.28}$$

It is convenient to express the normal vector in covariant components and the wave vector in contravariant components (G.23):

$$\frac{\partial \Phi_{in}}{\partial n} = \vec{n} \cdot \vec{\nabla}\Phi_{in} = n_{\alpha}\vec{a}^{(\alpha)} \cdot ik^{\beta}\vec{a}_{(\beta)}\Phi_{in} = in_{\alpha}k^{\beta}\delta^{\alpha}_{\beta}\Phi_{in} = in_{\alpha}k^{\alpha}\Phi_{in} \tag{G.29}$$

Using that the normal vector aligns with the contravariant base vector, (Equation E.13):

$$\frac{\partial^2 \Phi_{in}}{\partial t \partial n} = \omega n_1 k^1 \Phi_{in} \tag{G.30}$$

$$\frac{\partial^3 \Phi_{in}}{\partial t^2 \partial n} = -i\omega^2 n_1 k^1 \Phi_{in} \tag{G.31}$$

G.2.3. Second-Order Tangential Derivative

As the potential Φ_{in} is a scalar just as the pressure p, the aforementioned derivation of the second-order tangential derivative can be used.

$$\frac{\partial^2 \Phi_{in}}{\partial \tau \partial \tau} = \frac{1}{g_{22}} \left(\frac{\partial^2 \Phi_{in}}{\partial \xi^2 \partial \xi^2} - \frac{\Gamma_{222}}{g_{22}} \frac{\partial \Phi_{in}}{\partial \xi^2} \right) \tag{G.32}$$

The spatial derivative in a certain curvilinear direction returns the covariant component of the wave vector in that direction. Using that this is a projection onto a covariant base vector and $\vec{k}$ is constant, the following is derived:

$$\frac{\partial \Phi_{in}}{\partial \xi^2} = ik_2 \Phi_{in} \tag{G.33}$$

$$\frac{\partial^2 \Phi_{in}}{\partial \xi^2 \partial \xi^2} = \frac{\partial}{\partial \xi^2}[ik_2 \Phi_{in}] = (ik_2)^2 \Phi_{in} + \frac{\partial (ik_2)}{\partial \xi^2} \Phi_{in} = -(k_2)^2 \Phi_{in} + i \frac{\partial (\vec{k} \cdot \vec{a}_{(2)})}{\partial \xi^2} \Phi_{in} \tag{G.34}$$

$$-(k_2)^2 \Phi_{in} + i\vec{k} \cdot \frac{\partial (\vec{a}_{(2)})}{\partial \xi^2} \Phi_{in} = -(k_2)^2 \Phi_{in} + ik^\alpha \vec{a}_{(\alpha)} \cdot \frac{\partial \vec{a}_{(2)}}{\partial \xi^2} \Phi_{in} = \tag{G.35}$$

$$-(k_2)^2 \Phi_{in} + ik^\alpha \Gamma_{\alpha 22} \Phi_{in} = -(k_2)^2 \Phi_{in} + ik^1 \Gamma_{122} \Phi_{in} + ik^2 \Gamma_{222} \Phi_{in} \tag{G.36}$$

The result can be expressed in both Christoffel symbols of the first and second kind, however the first kind is more convenient as these are computed for the absorbing parts of the GABCs already.

Substituting the results in the second-order tangential derivative formulation gives:

$$\frac{\partial^2 \Phi_{in}}{\partial \tau \partial \tau} = \frac{1}{g_{22}} \left(-(k_2)^2 \Phi_{in} + ik^1 \Gamma_{122} \Phi_{in} + ik^2 \Gamma_{222} \Phi_{in} - \frac{\Gamma_{222}}{g_{22}} ik_2 \Phi_{in} \right) \tag{G.37}$$

The mixed time and tangential derivative is then computed by multiplying the equation stated above by $-i\omega$.

G.2.4. Components of Wave Vector

In the derivation, both covariant and contravariant components of $\vec{k}$ are used. $\vec{k}$ and the base vectors at each boundary face are known, which allows to compute the components as follows:

$$k^\alpha = \vec{k} \cdot \vec{a}^{(\alpha)} \tag{G.38}$$

$$k_\alpha = \vec{k} \cdot \vec{a}_{(\alpha)} \tag{G.39}$$

G.2.5. Combining Building Blocks

All building blocks stated above are combined to introduce the analytical RHS evaluation corresponding to a desired wave and GABC formulation. The real part ($\Re[...]$) of the equation is taken to obtain the value of input.

H

Determining Reflection

In this appendix, additional explanations for the method of determining reflection from an ABC are described. Also, analytical derivations are given for the reflection coefficients in case of a centred source and off-centre source. First a short introduction on Bessel functions will be given, and they will be applied afterwards in the determination of reflections.

H.1. Introduction Bessel functions

Bessel functions are an analytical solution to Bessel's equation, which describes waves in circular domains [8]. Bessel functions consist of two basic types. Bessel functions of the first kind $J_m(kr)$ are continuous in the origin. Bessel functions of the second kind $Y_m(kr)$ are singular in the origin. The functions are dependent on the radius from the origin and a wavenumber. Depending on order m, the functions take on different shapes.

A linear combination can be made of the two types, which are called Hankel functions:

$$H_m^{(1)}(kr) = J_m(kr) + i\, Y_m(kr) \tag{H.1}$$

$$H_m^{(2)}(kr) = J_m(kr) - i\, Y_m(kr) \tag{H.2}$$

The Hankel function with order 0 can be used to describe outward travelling waves ($H_0^{(1)}$) and inward travelling waves ($H_0^{(2)}$) from the origin. Both are singular in the origin/source because they contain the second Bessel function as well.

H.2. Determining Centred Source Reflection

To determine the reflection of a centred source, Hankel functions can be fitted to the time signal of the combination of the outward radiating and reflected wave. This can be done using a least squares approach based on Hankel function coefficients for a given wave number.

The outgoing wave and reflected ingoing wave combination can be described as:

$$p(r,t) = A_{out}H_0^{(1)}(kr)e^{-i\omega t} + A_{in}H_0^{(2)}(kr)e^{-i\omega t} \tag{H.3}$$

In which all values are complex numbers with a real and imaginary component. Because the pressure in the simulation is real valued, the pressures correspond to the real part of this equation. When taking the real part of the signal and expanding this in terms of real and imaginary components:

$$p(r,t) = \Re(A_{out})\Big[\ \ \Re(H_0^{(1)})\cos(\omega t) + \Im(H_0^{(1)})\sin(\omega t)\Big] \tag{H.4}$$
$$+\Im(A_{out})\Big[-\Im(H_0^{(1)})\cos(\omega t) + \Re(H_0^{(1)})\sin(\omega t)\Big] \tag{H.5}$$
$$+\Re(A_{in})\Big[\ \ \Re(H_0^{(2)})\cos(\omega t) + \Im(H_0^{(2)})\sin(\omega t)\Big] \tag{H.6}$$
$$+\Im(A_{in})\Big[-\Im(H_0^{(2)})\cos(\omega t) + \Re(H_0^{(2)})\sin(\omega t)\Big] \tag{H.7}$$

In this expression, only the complex amplitudes A_{out} and A_{in} are unknown. For the numerical simulation results, all pressure values can be averaged over bins of constant radius and a certain angle range for each time step. These averages give data in the form of $p(r,t)$ for certain angle sectors. If one would not divide the domain in angular sectors, phase mismatches due to numerical dispersion can influence the results. This phase mismatch will result in cancellation when averaging over a constant radius annulus.

For angular sector, the following system of equations can be set up that holds for each radial bin and each time step. $C_i(r,t)$ is then determined according to H.4 for each bin and time step:

$$p(r,t) = \Re(A_{out})\,[C_1(r,t)] + \Im(A_{out})\,[C_2(r,t)] + \Re(A_{in})\,[C_3(r,t)] + \Im(A_{in})\,[C_4(r,t)] \tag{H.8}$$

For the radial bins, a range will be chosen that is not contaminated with introduction effects of initiating the simulation with a smooth introduction envelope for the forcing of a wave. Therefore, the time and spatial (radial) window will be chosen such that a constant signal of the pure wave can be analysed. This results in a certain annulus of the circular domain is chosen that is as large as possible spatially, but also has a sufficient amount of time steps where the introduction effects are not in the annulus.

With all radial bins in the annulus and the time steps available, an accurate least squares fit can be made to determine the components of the complex amplitudes: $\Re(A_{out})$, $\Im(A_{out})$, $\Re(A_{in})$ and $\Im(A_{in})$. After the fit, the reflection coefficient can be determined as follows for each angular sector:

$$R = \frac{||A_{in}||}{||A_{out}||} \tag{H.9}$$

The reflection coefficients will then be averaged to obtain a reflection coefficient for the entire boundary condition.

H.2.1. Analytical Reflection

As the Sommerfeld BC is an approximation of a Dirichlet to Neumann map that is exact at infinity, there is a certain analytical absorbing performance that can be attained on a curved boundary. Based on a Hankel function, this analytical value will be derived below.

$$\Phi = \Phi_{out} + \Phi_{in} \tag{H.10}$$
$$\Phi_{out} = A_{out}H_0^{(1)}(kr)e^{-i\omega t} \tag{H.11}$$
$$\Phi_{in} = A_{in}H_0^{(2)}(kr)e^{-i\omega t} \tag{H.12}$$

Sommerfeld operator applied on a circle:

$$\left(\frac{\partial}{\partial t} + c\frac{\partial}{\partial r}\right)\Phi_{out} \tag{H.13}$$

$$\left(-i\omega\Phi_{out} + cA_{out}\frac{\partial H_0^{(1)}(kr)}{\partial r}e^{-i\omega t}\right) \tag{H.14}$$

$$\left(-i\omega\Phi_{out} + cA_{out}\frac{\partial kr}{\partial r}\frac{\partial H_0^{(1)}(kr)}{\partial kr}e^{-i\omega t}\right) \tag{H.15}$$

$$\left(-i\omega\Phi_{out} + cA_{out}k(-H_1^{(1)}(kr))e^{-i\omega t}\right) \tag{H.16}$$

$$\left(-i\omega\Phi_{out} + ck\frac{-H_1^{(1)}(kr)}{H_0^{(1)}(kr)}A_{out}H_0^{(1)}(kr)e^{-i\omega t}\right) \tag{H.17}$$

$$\left(-i\omega - ck\frac{H_1^{(1)}(kr)}{H_0^{(1)}(kr)}\right)\Phi_{out} \tag{H.18}$$

$$\left(\frac{\partial}{\partial t} + c\frac{\partial}{\partial r}\right)\Phi_{in} \tag{H.19}$$

$$\left(-i\omega\Phi_{in} + cA_{in}\frac{\partial H_0^{(2)}(kr)}{\partial r}e^{-i\omega t}\right) \tag{H.20}$$

$$\left(-i\omega\Phi_{in} + cA_{in}\frac{\partial kr}{\partial r}\frac{\partial H_0^{(2)}(kr)}{\partial kr}e^{-i\omega t}\right) \tag{H.21}$$

$$\left(-i\omega\Phi_{in} + cA_{in}k(-H_1^{(2)}(kr))e^{-i\omega t}\right) \tag{H.22}$$

$$\left(-i\omega\Phi_{in} - ck\frac{H_1^{(2)}(kr)}{H_0^{(2)}(kr)}A_{in}H_0^{(2)}(kr)e^{-i\omega t}\right) \tag{H.23}$$

$$\left(-i\omega - ck\frac{H_1^{(2)}(kr)}{H_0^{(2)}(kr)}\right)\Phi_{in} \tag{H.24}$$

(H.25)

The following relations are used for taking derivatives of Hankel functions:

$$\frac{\partial}{\partial z}H_m^{(1)}(z) = -H_{m+1}^{(1)}(z) \tag{H.26}$$

$$\frac{\partial}{\partial z}H_m^{(2)}(z) = \frac{1}{2}\left[H_{m-1}^{(2)}(z) - H_{m+1}^{(2)}(z)\right] \tag{H.27}$$

$$H_{-m}^{(2)}(z) = e^{-i\pi m}H_m^{(2)}(z) \tag{H.28}$$

Combining into a total signal and solving for the complex amplitudes gives the reflection coefficient when imposing the Sommerfeld BC at a certain radius for a certain wave number.

$$\left(\frac{\partial}{\partial t} + c\frac{\partial}{\partial r}\right)\Phi = 0 \tag{H.29}$$

$$\left(-i\omega(\Phi_{out} + \Phi_{in}) + c\left(-k\frac{H_1^{(1)}(kr)}{H_0^{(1)}(kr)}\Phi_{out} - k\frac{H_1^{(2)}(kr)}{H_0^{(2)}(kr)}\Phi_{in}\right)\right) = 0 \tag{H.30}$$

$$\left(-i\omega(\Phi_{out} + \Phi_{in}) - \omega\left(\frac{H_1^{(1)}(kr)}{H_0^{(1)}(kr)}\Phi_{out} + \frac{H_1^{(2)}(kr)}{H_0^{(2)}(kr)}\Phi_{in}\right)\right) = 0 \tag{H.31}$$

Dividing out $e^{-i\omega t}$ and gathering terms corresponding to the complex amplitudes:

$$\left(-i\omega H_0^{(1)}(kr) - \omega H_1^{(1)}(kr)\right)A_{out} + \left(-i\omega H_0^{(2)}(kr) - \omega H_1^{(2)}(kr)\right)A_{in} = 0 \tag{H.32}$$

Solving for $A_{out} = 1$ gives A_{in} and the reflection coefficient from Equation H.9 for every kr.

The resulting reflection coefficient is given in Figure H.1

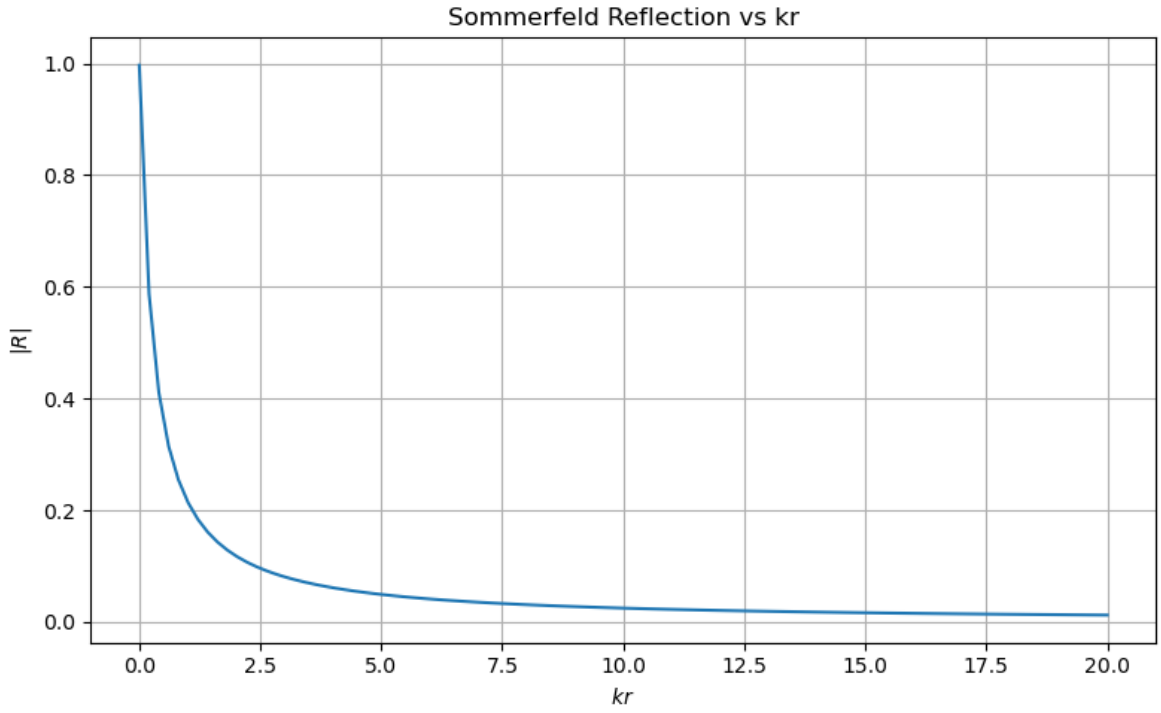

Figure H.1: Sommerfeld reflection coefficient vs kr value for waves radiating from a point source

H.3. Determining Off-Centre Source Reflection

As mentioned in the main body of this work, the amplitude of the outward radiating Hankel function is determined through a least squares fit. The least squares fit follows the same procedure as stated in section H.2, without the reflected reflected signal.

For the imposed Sommerfeld BC, an analytical result can be derived. This will be described in the following section.

H.3.1. Analytical Reflection

To determine the analytical reflection coefficient for an off-centre source, the Helmholtz equation is considered. This represents the frequency-domain equivalent of the wave equation and corresponds to the linearised shallow water equations studied in this work. The Helmholtz equation gives a steady state solution, which can be used to obtain a reflection coefficient.

For this analysis, the off-centre Hankel is represented as an infinite modal sum of centred Hankel functions. For these centred Hankel functions, the Sommerfeld boundary condition can be applied in a straightforward manner. The reflection coefficient can then be computed based on the sum of all modes together. This is performed at each boundary location on the circular boundary, represented by polar coordinates ($r = R_d$, φ). Each boundary point corresponds to a certain incidence angle of the off-centre Hankel. This way, an analytical reflection coefficient can be determined as a function of incidence angle.

The off-centre source location is indicated by $\vec{x}_s$. In polar coordinates, the modulus is described as $||\vec{x}_s||$ and the angle φ as $\angle(\vec{x}_s)$. At the boundary locations, the polar coordinates are represented by radius R_d and angle φ. The off-centre source is represented at the boundary $(r = R_d, \varphi)$ as a general solution to the 2D Helmholtz equation. [6]:

$$\Phi_{out}(R_d, \varphi) = \frac{i}{4} H_0^{(1)}(k||\vec{x}_b - \vec{x}_s||) \tag{H.33}$$

This general solution can be written as an infinite modal sum of centered Hankel functions using Graf's addition theorem:

$$\Phi_{out}(R_d, \varphi) = \frac{i}{4} \sum_{m=-\infty}^{\infty} J_m(k||\vec{x}_s||) H_m^{(1)}(kR_d) e^{im(\varphi - \angle(\vec{x}_s))} \tag{H.34}$$

The reflected signal is represented as an infinite sum of Bessel functions, with coefficients per mode a_m and b_m:

$$\Phi_{refl}(R_d, \varphi) = \sum_{m=-\infty}^{\infty} (b_m J_m(kR_d) + a_m Y_m(kR_d)) e^{im\varphi} \tag{H.35}$$

The reflected signal should be continuous in the centre of the domain, so the infinite sum should consist of only $J_m(kR)$:

$$\Phi_{refl}(R_d, \varphi) = \sum_{m=-\infty}^{\infty} b_m J_m(kR_d) e^{im\varphi} \tag{H.36}$$

As φ is periodic, the angular representation can be shifted with a constant phase. This results in the same physical solution for the system, but rotated. The argument of the source location vector will be used for the shift to match the description of the incident wave in Equation H.34.

$$\Phi_{refl}(R_d, \varphi) = \sum_{m=-\infty}^{\infty} b_m J_m(kR_d) e^{im(\varphi - \angle(\vec{x}_s))} \tag{H.37}$$

Now the frequency domain equivalent of the Sommerfeld boundary condition in polar coordinates is applied to the total signal, which results in the coefficient b_m for each reflected mode such that Equation H.38 is satisfied.

$$\left(\frac{\partial}{\partial r} - ik\right)(\Phi_{out} + \Phi_{refl}) = 0 \tag{H.38}$$

$$b_m = -\frac{i}{4} J_m(k||\vec{x}_s||) \frac{k \frac{\partial H_m^{(1)}(kr)}{\partial(kr)} - ikH_m^{(1)}(kr)}{k \frac{\partial J_m(kr)}{\partial(kr)} - ikJ_m(kr)} \tag{H.39}$$

$$b_m = -\frac{i}{4} J_m(k||\vec{x}_s||) \frac{\frac{\partial H_m^{(1)}(kr)}{\partial(kr)} - iH_m^{(1)}(kr)}{\frac{\partial J_m(kr)}{\partial(kr)} - iJ_m(kr)} \tag{H.40}$$

This way, an analytical description is obtained for the infinite sum of reflected modes at each boundary point. However, to translate this to a reflection coefficient, the infinite sum has to be evaluated numerically. The infinite sum therefore has to be truncated to a certain maximum mode m_{max}, for which the sum converges with a certain tolerance. Convergence is verified by increasing the truncation limit until

the relative change in both the incident and reflected field amplitudes falls below a prescribed tolerance of 1×10^{-10}.

When convergence is reached, the outgoing and reflected signal at each boundary point are known using Equation H.34 and H.37 respectively. The reflection coefficient can then be found through:

$$R = \left|\left| \frac{\Phi_{refl}}{\Phi_{out}} \right|\right| \tag{H.41}$$

Roadmap Towards Implementation

In this appendix, a roadmap to accurate and computationally affordable 3D CFD simulations for non-linear wave interaction is given below. The roadmap has several phases, for which a few results are critical for the potential of the method. This roadmap is to give an indication of the work that still needs to be performed before implementation, but is not definite. The ultimate goal is to simulate motions accurately for SSCVs within reasonable time.

I.1. Current Status

It was realised during this thesis that circular boundaries pose absorbing limitations. For all desired wavelength-radius ratios that are likely for 3D CFD simulations, proper absorbance needs to be accomplished. This can be accomplished using higher-order formulations based on circular boundary operators. These are available in literature, but should be implemented in the generalised curvilinear coordinates. Also, the performance should be evaluated rigorously. At this stage, a test quantifying reflection coefficients of Long-Crested Wave (LCW) absorption on circular boundaries is necessary before to gain insight in absorption limits for this wave type.

I.2. Higher-Order GABC Suited for Circular Boundaries

Before stepping to 3D, a formulation needs to be found that incorporates circular boundary effects properly together with angular dependence for the wave combination encountered in offshore wave interaction simulations. The formulation needs to absorb LCWs properly, as well as radiated and diffracted waves. This formulation will rely on methods that are available in literature. If this formulation can be combined with introducing waves effectively, the step towards 3D can be made.

I.3. Application in 3D

The GABC can now be implemented in 3D. The GABC now also will have to capture dispersion effects of the free-surface waves. This should be incorporated into the GABC either by introducing a vertical derivative term to approximate the dispersion relation by rational approximation or by extending the GABC to third order. Either version should again be stable.

After this is accomplished, a proper analysis of absorbing performance of the GABC should be performed. Also the accumulated wave reflection over longer periods for multidirectional wave spectra should be evaluated. If results are sufficiently accurate, this gives confidence in modelling non-linear wave interaction with the GABC at the boundary.

I.4. Simulating Non-linear Wave Interaction

Depending on the implementation in 3D, the rectangular interior can be used for a cut-cell method. This has proven accurate results for non-linear wave interaction. It should be checked how to apply geometric free-surface reconstruction in the quasi curvilinear interior of domain. Also the translation of

the solution to the curvilinear domain should be checked. Also the free-surface reconstruction in the non rectangular part of the domain should be checked.

For stepping to 3D implementation, a compiled coding language should be used in order to run simulations within reasonable time. This means the existing python code needs to be translated and prepared for 3D space.

The model can now be validated, using a simple diffractor of which the diffraction pattern is known. The known diffractor can also be partially submerged below the free surface, mimicking a submerged floater of an SSCV at inconvenient draught. The behaviour can possibly be validated using a model test.

I.5. Modelling SSCVs at Inconvenient Draught

Once the motions of SSCVs at inconvenient draught can be modelled using CFD, several additional studies should be performed. The motion behaviour of the SSCV should be investigated to determine which principles of linear diffraction theory remain valid. An important part of this is checking whether linear superposition of motion modes is still sufficiently accurate.

Different combinations of H_S, frequency, and directionality should be simulated to investigate the motion behaviour of the SSCV in these situations. From this, added mass and damping coefficients can be composed that match the non-linear motion behaviour for this wave combination. This way, a H_S-aware RAO can be composed and motion prediction based on this can be compared to model scale or full scale tests. If the response matches well, this gives confidence that the 'linear' superposition principle can still be used with sufficient accuracy.

It should also be evaluated whether it is computationally feasible to run an entire wave spectrum as input and record the response of the SSCV over a number of cycles. From this, the response can be derived through a Fourier transform of the motion signal. Depending on the results, it can be checked how non-linear the problem actually is, and what modelling strategy works properly to capture the non-linear behaviour of the SSCV.

Bibliography

[1] A. Bayliss and E. Turkel. “Radiation Boundary Conditions for Wave-Like Equations”. In: *Communications on Pure and Applied Mathematics* 33.6 (1980), pp. 707–725.

[2] J.P. Berenger. “A Perfectly Matched Layer for the Absorption of Electromagnetic Waves”. In: *Journal of Computational Physics* 114 (1994), pp. 185–200.

[3] X. Chang and P.R. Wellens. “A Generating Absorbing Boundary Condition for Simulating Wave Interaction with Maritime Structures in Current or at Forward Speed”. In: *Computers and Fluids* 274 (2024), p. 106216.

[4] Y. Choi et al. “Performance of different techniques of generation and absorption of free-surface waves in Computational Fluid Dynamics”. In: *Ocean Engineering* 214 (2020), p. 107575.

[5] F. Collino and P. Joly. “New Absorbing Boundary Conditions for the Finite Element Solution of 3D Maxwell’s Equations”. In: *IEEE Transactions on Magnetics* 31.3 (May 1995), pp. 1618–1621.

[6] D. Colton and R. Kress. *Inverse Acoustic and Electromagnetic Scattering Theory*. 3rd. New York: Springer, 2013.

[7] R. De Bruijn et al. “Calculation of Wave Forces and Internal Loads on a Semi-Submersible at Shallow Draft Using an IVOF Method”. In: *Proceedings of the ASME 2011 30th International Conference on Offshore Mechanics and Arctic Engineering (OMAE)*. ASME. 2011, OMAE2011–49236.

[8] J. Dutka. “On the early history of Bessel functions”. In: *Archive for History of Exact Sciences* 49.2 (June 1995), pp. 105–134.

[9] B. Düz et al. “An Absorbing Boundary Condition for Free Surface Water Waves”. In: *Computers and Fluids* 156 (2017), pp. 562–578.

[10] B. Engquist and A. Majda. “Absorbing Boundary Conditions for the Numerical Simulation of Waves”. In: *Mathematics of Computation* 31.139 (July 1977), pp. 629–651.

[11] G. Fekken. “Numerical simulation of free□surface flow with moving rigid bodies”. PhD thesis. University of Groningen, 2004.

[12] C.J. Fitzgerald. “Nonlinear Potential Flow Models”. In: *Numerical Modelling of Wave Energy Converters: State-of-the-Art Techniques for Single Devices and Arrays*. Academic Press, 2016. Chap. 5, pp. 83–104.

[13] D. Givoli. “High-order Local Non-Reflecting Boundary Conditions: A Review”. In: *Wave Motion* 39.4 (Apr. 2004), pp. 319–326.

[14] D. Givoli and B. Neta. “High-order non-reflecting boundary scheme for time-dependent waves”. In: *Journal of Computational Physics* 186.1 (2003), pp. 24–46.

[15] M.J. Grote and J.B. Keller. “On Nonreflecting Boundary Conditions”. In: *Journal of Computational Physics* 122.2 (1995), pp. 231–243.

[16] T. Hagstrom and S.I. Hariharan. “A Formulation of Asymptotic and Exact Boundary Conditions Using Local Operators”. In: *Applied Numerical Mathematics* 27.4 (1998), pp. 403–416.

[17] T. Hagstrom and S. Kim. “Complete radiation boundary conditions for the Helmholtz equation I: waveguides”. In: *Numerische Mathematik* 141.4 (2019), pp. 917–966.

[18] T. Hagstrom and S. Kim. “Complete radiation boundary conditions for the Helmholtz equation II: domains with corners”. In: *Numerische Mathematik* 153.4 (2023), pp. 775–825.

[19] T. Hagstrom and T. Warburton. “A new auxiliary variable formulation of high-order local radiation boundary conditions: corner compatibility conditions and extensions to first-order systems”. In: *Wave Motion* 39.4 (2004), pp. 327–338.

[20] T. Hagstrom and T. Warburton. “Complete radiation boundary conditions: Minimizing the long time error growth of local methods”. In: *SIAM Journal on Numerical Analysis* 47.5 (2009), pp. 3678–3704.

[21] T. Hagstrom et al. “The Double Absorbing Boundary Method”. In: *Journal of Computational Physics* 259 (2014), pp. 220–241.

[22] R.L. Higdon. “Absorbing Boundary Conditions for Difference Approximations to the Multi-Dimensional Wave Equation”. In: *Mathematics of Computation* 47.176 (Oct. 1986), pp. 437–459.

[23] N.G. Jacobsen, D.R. Fuhrman, and J. Fredsøe. “A wave generation toolbox for the open-source CFD library: OpenFOAM”. In: *International Journal for Numerical Methods in Fluids* 70.9 (2012), pp. 1073–1088.

[24] J.J.I.M. van Kan et al. *Discretization of the incompressible Navier-Stokes equations in general coordinates using contravariant velocity components*. Tech. rep. TU Delft, 1991.

[25] K. Kassels and G. Segal. *Some 2D test examples for the ISNaS incompressible code*. Tech. rep. TU Delft, 1991.

[26] S. Kim. “Hybrid absorbing boundary conditions of PML and CRBC”. In: *Journal of Computational and Applied Mathematics* 399 (2022), p. 113713.

[27] K.M.T. Kleefsman et al. “A Volume-of-Fluid Based Simulation Method for Wave Impact Problems”. In: *Journal of Computational Physics* 206.1 (2005), pp. 363–393.

[28] A. Modave, C. Geuzaine, and X. Antoine. “Corner treatments for high-order local absorbing boundary conditions in high-frequency acoustic scattering”. In: *Journal of Computational Physics* 401 (2020).

[29] K.M. Moerman. “GIBBON: The Geometry and Image-Based Bioengineering add-On”. In: *Journal of Open Source Software* 3.22 (2018), p. 506.

[30] H. Ottens and A. Pistidda. “Motion RAOs of a SSCV at Deep and Inconvenient Draft Using CFD”. In: *Proceedings of the ASME 2015 34th International Conference on Offshore Mechanics and Arctic Engineering (OMAE)*. ASME. 2015, OMAE2015–41917.

[31] B. Simon et al. “Comparing methods of modeling depth-induced breaking of irregular waves with a fully nonlinear potential flow approach”. In: *Journal of Ocean Engineering and Marine Energy* 5.4 (2019), pp. 365–383.

[32] H. Sparidans. “Een oplosmethode voor de incompressible Navier-Stokes vergelijkingen in gegeneraliseerde coördinaten volgens de Eindige Volumen Methode”. MSc thesis. Eindhoven University of Technology, 1992.

[33] B.P.J. Van der Kroft. “Motion Prediction of a Semi-Submersible Crane Vessel at Inconvenient Draft: Identifying the Cause of the Discrepancies on an Experimental Basis”. MSc thesis. Delft University of Technology, Oct. 2022.

[34] I. Van Winsen, J.S. Bokhorst, and R.H.M. Huijsmans. “Calculation of Wave Height Dependent Force RAO’s on Submerged Bodies in Close Proximity to the Free Surface”. In: *Proceedings of the ASME 2013 32nd International Conference on Offshore Mechanics and Arctic Engineering (OMAE)*. ASME. 2013, OMAE2013–10340.

[35] W. Wang et al. “A flexible fully nonlinear potential flow model for wave propagation over the complex topography of the Norwegian coast”. In: *Applied Ocean Research* 122 (2022), p. 103796.

[36] P.R. Wellens. “Wave Simulation in Truncated Domains for Offshore Applications”. PhD thesis. Delft University of Technology, 2012.

[37] P.R. Wellens and M.J.A. Borsboom. “A generating and absorbing boundary condition for dispersive waves in detailed simulations of free-surface flow interaction with marine structures”. In: *Computers and Fluids* 200 (2020), p. 104387.